ADVANCED ELECTRON MAGNETIC RESONANCE STUDIES OF NITROGEN LIGATION IN PHOTOSYNTHETIC SYSTEMS

By

Michelle Mac

A DISSERTATION

Submitted to
Michigan State University
in partial fulfillment of the requirements
for the degree of

DOCTOR OF PHILOSOPHY

Department of Chemistry

1996

ABSTRACT

ADVANCED ELECTRON MAGNETIC RESONANCE STUDIES OF NITROGEN LIGATION IN PHOTOSYNTHETIC SYSTEMS

By

Michelle Mac

Oxygenic photosynthesis in higher plants and cyanobacteria requires the interplay of two membrane bound pigment-protein reaction centers, Photosystem I and II (PSI and PSII). In each of these, the primary photochemical event proceeds via the light induced generation of a chlorophyll a cation radical species. These specialized chlorophylls initiate a series of unidirectional electron transfer events that ultimately either oxidize water (PSII) or reduce nicotinamide adenine dinucleotide (PSI). To understand better both the initial charge separation and subsequent electron transfer events, knowledge regarding the geometric and electronic structures of the primary electron donor is desirable. Recent X-ray crystallographic studies have shown that the primary donor in PSI, P_{700}, consists of a dimer of chlorophyll a molecules; the electronic structure of the cation radical, however, remains elusive. It has been suggested, on comparison to the primary donors in the bacterial systems and recent magnetic resonance studies, that the unpaired electron is delocalized either monomerically or highly asymmetrically over the two halves of the dimer. By using a combination of histidine-tolerant mutants of *Synechocystis PCC 6803*, isotopic enrichment, advanced electron magnetic resonance

spectroscopies and numerical simulations of experimental data, we were able to determine the magnetic coupling parameters for the pyrrole nitrogens in P_{700}^{+} and, moreover, identify definitively an axial histidine ligand to P_{700}^{+}. The magnitude of the of the spin density on the pyrrole nitrogens is supportive of a model for P_{700}^{+} where the excited state orbital makes a significant contribution to the spin density distribution of the cation radical. The methodology utilized to determine this structure, a combination of isotope enrichment, electron magnetic resonance spectroscopy and numerical simulations, provides a means by which complicated couplings in biological systems can be consistently and systematically evaluated.

ACKNOWLEDGMENTS

The journey through graduate school can be long and arduous, one rarely makes the trip alone. The people I've had the pleasure of working with over the past six years have made graduate achool a rewarding and memorable experience.

The histidine ligand work would not have been possible without the histidine tolerant mutant samples developed by Dr. Bruce Diner and Dr. Xiao-song Tang at Dupont. Dr. Neil Bowlby was also instrumental in the PSI work, teaching me the PSI prep and walking me through it several times. Neil was also my source of biochemical knowledge, and knew just enough spectroscopy to make him dangerous at group meetings, where his questions *always* caught me off guard! I am also indebted to Pierre Dorlet for helping me make oxygen evolving PSII samples and also for his willingness to come in at the crack of dawn just to help me with sample illumination.

I never had the privilege of a direct collaboration with either Professor Charles Yocum, or Professor Dave Britt, however the interactions I had with both of them will be remembered fondly. In particular, the many lively discussions (both at group meetings and at Dag's) I had with Charlie about "information rich" spectroscopy and "sporting methods", and the bullboys, for whom Dave will always be remembered (even though he got a graduate student to do the dirty work!).

Choosing to work jointly between Professors Jerry Babcock and John McCracken was the best decision I made in graduate school, and I have to thank Dr. Costas Varotsis for suggesting the collaboration during one of our many late night talks during my first year.

I was also lucky enough to be assigned to work with Dr. Matt Espe, a senior grad student at that time. Matt became both a mentor and friend and taught me everything he knew about EPR and BBY preps. He also showed me that signal averaging can be fun!

The many interactions with the members of the Babcock and McCracken groups made my years at MSU enjoyable. In particular, I would like to thank Dr. Kurt Warncke, Dr. Curt Hoganson, Dr. Nikos Lydakis-Simatris and Cecilia Tommos for our many discussions/arguments about magnetic resonance, not to mention our "lively" EPR meetings. Kurt was not only the best post-doc with whom I have worked, but a great person and friend as well.

There are some people in our lives with whom we connect and about whom we cannot say enough. Kerry Reidy-Cedergren is one of these people. We started grad school together and have shared every milestone in our lives, both professionally and personally. She was always willing to take time away from anything she was doing to talk to me about my research, my life, or, on several occasions, to talk me *out* of quitting! She is the most giving and caring person I have met and I cannot express how much I will miss her when I leave.

I was also lucky enough to have a circle of friends that were supportive and could always be counted on for a celebration. The closeness and camaraderie I felt with this group of friends: Matt Gardner, Sara Helvoigt, Chris Powell, Per Askeland and Tom

Halasinski, was the one constant in graduate school. They were always there to share the good times or to commiserate over a bad day in lab; I'll miss them tremendously and hope to be fortuitous enough to find such a good group of friends. I'll especially miss our Friday "Happy Hours" and our late night trips to Dag's, where T., Brenda and Randy always had a cold beer and a triangle fish waiting!

There were also other people in the department without whom the thesis writing process would have been (even more) stressful. I'd like to thank the staff in the Main Office and the Graduate Office, especially Lisa Dillingham and Beth Thomas, for their assistance in preparing the final thesis document and also for their friendship. I am also indebted to John and Jerry's secretary, Vada O'Donnell, for moral support over my graduate career. I also have to thank Erik Ruggles for keeping me focused on thesis writing, which allowed me to finish an unheard of TWELVE hours before the deadline!

The two individuals, however, who have had the greatest influence on my life and my development as a scientist over the last six years are my advisors, Jerry Babcock and John McCracken. Through their teachings, guidance and inspiration I have learned to think independently, to solve problems and, more importantly, to do control experiments! The confidence that I gained in graduate school is the direct result of the interactions I had with them and their respective research groups and I would not have done as well as I have without them. I could not have asked for two better people as advisors and I have thoroughly enjoyed my time in the lab.

Lastly, I would like to thank my parents and brothers for their love and support over the last six years, for believing in me and for teaching me that I could do anything that I chose to.

To my parents.

TABLE OF CONTENTS

LIST OF TABLES

LIST OF FIGURES

Chapter 1

Introduction to Photosynthesis in Higher Plants and Cyanobacteria

Although photosynthesis has been studied extensively since the discovery of oxygen evolution from plants in 1780 by Joseph Priestley, many of the molecular intricacies of the process remain an enigma. The mechanism of photosynthesis utilizes photochemical energy from sunlight to disrupt chemical bonds in stable substrates. The free energy inherent in this process can be trapped by the organism to synthesize vital amino acids, proteins, nucleic acids and other essential biomolecules. Two classes of organisms utilize this photosynthetic process; these classes can be distinguished from one another by the presence of molecular oxygen as a catalytic product. Because photosynthetic bacteria do not evolve oxygen, the architecture that supports catalysis and electron transfer in these systems is simpler than that of higher plants and cyanobacteria, organisms that produce oxygen. The photosynthetic process of these oxygen-producing organisms can be described with a deceptively simple reaction

$$CO_2 + H_2O \longrightarrow (CH_2O)_n + O_2$$

The mechanism behind this reaction is complex and requires the interplay of many proteins and cofactors, many of which have not been characterized completely. Whereas bacteria utilize only one pigment protein reaction center, or photosystem, for conversion of light energy into chemically useful energy, the more complex plant systems contain two interacting photosystems. The first of these, Photosystem I (PSI) mediates the

production of oxidized plastocyanin and reduced nicotinamide adenine dinucleotide phosphate (NADPH), which is used by the plant to fuel the enzymatic cycles associated with the assimilation of carbon dioxide in the Calvin cycle.[1] Photosystem II (PSII) is associated with water oxidation and is the site of oxygen evolution.[2] Both of these systems and their respective electron transfer cofactors are represented schematically in Figure 1-1. This model, known as the Z-scheme,[3] indicates the flow of electrons in higher plants and cyanobacteria; the vertical position of each electron carrier corresponds to its reduction potential at pH = 7.0.

An interesting aspect of the electron transfer process in photosynthesis is its vectorial nature. The photosynthetic machinery is located in the plant cell in an organelle known as the chloroplast. The presence of an inner and outer membrane make chloroplasts analogous to the mitochondria found in respiring eukaryotic systems. The inner membrane of the chloroplast surrounds an aqueous protein matrix which contains closed vesicles, or thylakoid membranes. The thylakoid membranes separate two chemically different environments: the stroma, located on the exterior of the membrane, and the lumen, located on the interior. The membranes appear on electron micrographs as flattened sac-like structures and are "stacked" in certain regions of the chloroplast.[4] It has been estimated that as much as 85% of the PSII reaction centers are concentrated in these stacked regions, known as grana. PSI is found to a large extent, in the unstacked stromal regions of the thylakoid membrane. This asymmetric arrangement assists in providing directionality to the electron flow; the ultimate consequence of this directionality is the establishment of both charge and proton gradients across the photosynthetic membrane that provide the free energy necessary for ATP synthesis.

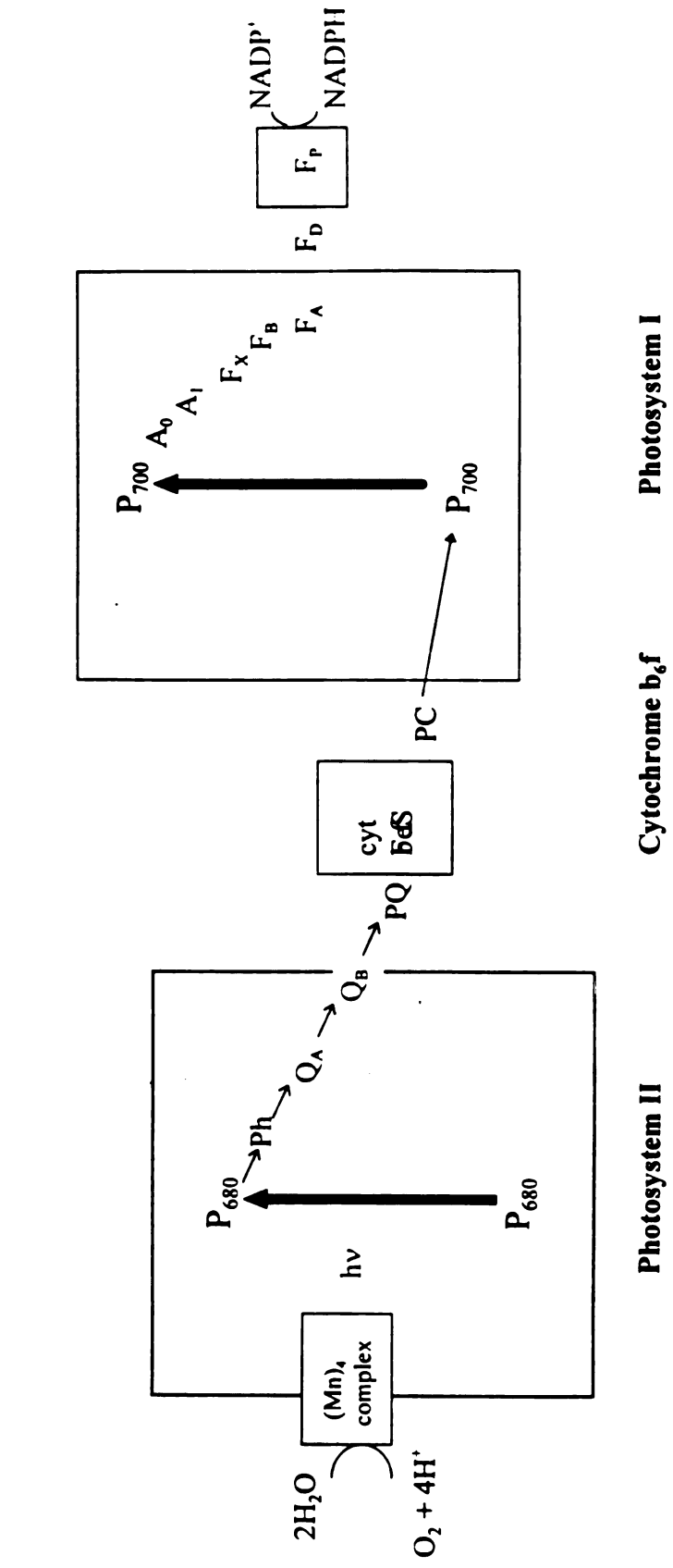

Figure 1-1: The Z scheme of photosynthesis representing non-cyclic electron flow in higher plants

Because PSI and PSII are linked by electron transfer reactions, their physical separation necessitates the presence of an additional membrane bound complex utilized as an electron transfer mediator. Cytochrome b_6f, distributed evenly between the grana (PSII) and stromal (PSI) regions of the thylakoid, is the ideal charge transfer interface between PSII and PSI.[5]

Photosystem I

The primary charge separation event in photosynthesis proceeds via the light induced generation of a chlorophyll (in higher plant and cyanobacterial systems) or bacteriochlorophyll (in bacterial systems) cation radical species. This species, $P_{\lambda max}$, where λmax indicates the wavelength at which the pigment absorbs maximally (λmax = 700 nm for PSI, 680 nm for PSII and either 960 or 870 nm in the bacterial systems), is distinguished from the light harvesting and energy transfer chlorophylls by its spectral and redox properties. Subsequent electron transfer occurs unidirectionally through a series of redox active cofactors whose stabilization of the transient charge separated states prevents back reactions and facilitates forward electron transfer. The plant is amazingly efficient at charge stabilization as the forward reactions occur with a quantum yield approaching unity.[6] The photoactive components responsible for this unidirectional electron transfer in PSI are located on three polypeptides genetically encoded by the psaA, psaB and psaC genes (the protein names are derived from their gene loci). These cofactors include the aforementioned primary electron donor P_{700}, a specialized

chlorophyll a species, a primary electron acceptor (A_0, also a chlorophyll a species), an intermediate quinone acceptor (A_1, a phylloquinone derivative) and three terminal iron-sulfur clusters (F_x, F_A and F_B). Reduction of the $NADP^+$ is accomplished by a ferredoxin protein. The reaction center heterodimer consists of two polypeptides, psaA and psaB, containing 750 and 734 amino acids residues and with molecular weights of 82 and 83 kDa, respectively. The reaction center complex in plants also includes approximately 100 antenna chlorophylls responsible for light harvesting and energy transfer, as well as a series of intrinsic, which can only be removed by detergent washing, and extrinsic, which can be removed by salt washing or treatment with chaotropic agents, polypeptides, many of whose functions are as yet undetermined.

The amino acid sequences of psaA and psaB have been determined and show sequence homologies of approximately 95% amongst subclasses of higher plants.[7] This high degree of homology remains even upon comparison to the amino acid sequences of more distantly related organisms, for example the cyanobacterium *Synechococcus* PCC 7002, especially when conservative replacements are considered. It is interesting to note that the psaB polypeptide contains a sequence of 100 amino acids that are virtually invariant amongst species. These amino acids include the cysteine residues ligating the Fe-S clusters[8] as well as the leucine zipper motif[9] thought to bind the two hydrophobic psaA and psaB proteins together.

The arrangement of the polypeptides and the presumed binding sites of the electron transfer cofactors of PSI are shown in Figure 1-2. Although the binding sites for many of the redox active cofactors are not known, it is expected that P_{700}, A_0 and A_1 are bound to either psaA or psaB of the heterodimer. The presence of a series of conserved

histidine residues in helix XIII of psaA and psaB indicates that these residues may be the putative axial ligands to the Mg^{2+} atoms of P_{700} and, or, A_0.[9] As mentioned, the cysteine ligands of F_x have been identified and show F_x as an interpolypeptide bridge between psaA and psaB. The terminal Fe-S centers (F_A and F_B) reside on a separate 8.9 kDa polypeptide known as psaC. These positions were recently confirmed by the 4.5 Å X-ray crystal structure of PSI,[10b] however, the positions of the other cofactors could not be determined unambiguously.

P_{700}

Because the highly unidirectional and efficient forward electron transfer events in PSI are controlled by the spatial and electronic arrangement of the cofactors involved, knowledge regarding the structure of these radicals is necessary to understand better the electron transfer processes in photosynthetic systems. The primary charge separation event in PSI proceeds via the light induced generation of a specialized chlorophyll a cation radical, P_{700}^{+}. The electronic and geometric structure of this radical can provide insights into the primary electron transfer events of PSI and ultimately shed light on the overall mechanism of electron transfer in PSI. Until recently, the lack of a high resolution crystal structure has precluded determination of the nuclearity of P_{700}.

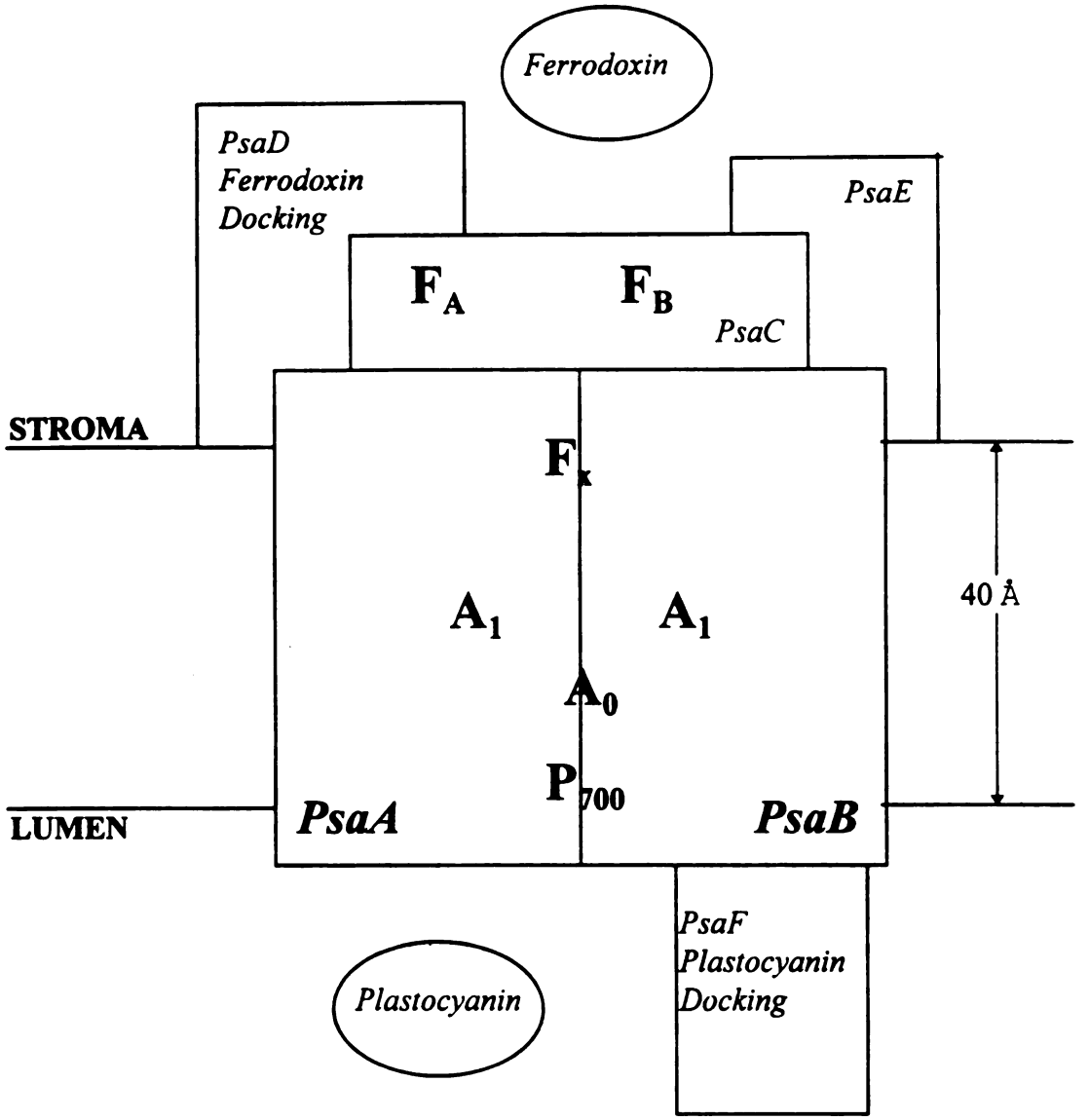

Figure 1-2: Proposed architecture for the PSI reaction center.

Although resonance Raman[11] and optical hole-burning experiments[12] have indicated a dimeric structure for P_{700} in its ground state, no evidence confirming these findings has been presented in the literature. Optical absorption data, however, provide evidence for a monomeric structure; deconvolution of the P_{700} chlorophyll envelope from these studies shows that P_{700} has a bandwidth and area consistent with a ratio of 1:2 for the oxidized species to reduced species.[13] These findings have led to the hypothesis that P_{700} in its ground state is structurally a dimeric species while P_{700}^{+} is electronically monomeric. Although this hypothesis has been investigated quite thoroughly by several research groups with multiple magnetic resonance techniques (*vide infra*),[14] no definite conclusions regarding the electronic structure of the cation radical have been made and the ambiguity surrounding its nuclearity and electronic structure remains.

Some insight into the structural arrangement of the PSI reaction center can be gained from comparison to the simpler bacterial reaction centers. Since the three dimensional structures of the bacterial reaction centers from *Rhodopseudomonas viridis* [15] and *Rhodobacter sphaeroides*[16] have been determined to high resolution with X-ray crystallography, these systems can been used as a template for the more complex oxygen evolving systems of higher plants and cyanobacteria. The bacterial reaction centers consist of a single photosystem with approximate C_2 symmetry. Electron transfer proceeds unilaterally down the L branch of the protein. The analogies to PSI extend to the structural arrangement of the primary donor, which has been shown to be a bacteriochlorophyll dimer with histidine residues as axial ligands to the Mg^{2+}.[15,16] These analogies, although a starting point for hypotheses regarding the structure of P_{700}, must be approached carefully as the presence of quinones as terminal electron acceptors in the

bacterial reaction centers indicates a similarity to PSII rather than PSI, which uses Fe-S centers in addition to quinones as terminal electron acceptors. Even with these differences the basic motif for photochemical charge separation is preserved in the bacterial reaction centers, PSII and PSI.

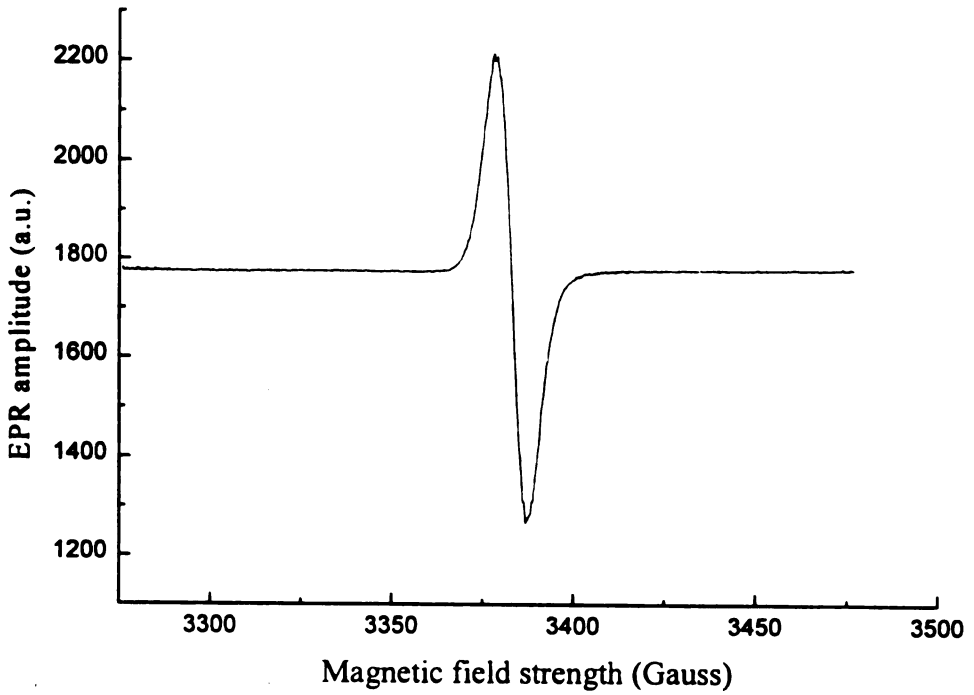

Figure 1-3: EPR spectrum from P_{700}^{+} from *Synechocystis PCC 6803*.

The presence of an easily trapped light-induced radical species makes each of these systems (eukaryotic and prokaryotic) especially amenable to the application of electron magnetic resonance techniques. Oxidation of P_{700} can be achieved either photochemically or chemically and leads to changes in the absorbance spectrum at 700,

685 and 435 nm. The EPR signal (known as Signal I, see Figure 1-3) from this cation radical was initially observed by Commoner *et al.*[17] in the 1950s and appears as a structureless Gaussian centered at g=2.0026 with a peak to peak linewidth of 7-8 Gauss.

Because the EPR linewidth of P_{700}^{+} is narrowed by a factor of $1/\sqrt{2}$ with respect to the chlorophyll cation radical monomer *in vitro*,[18] it was thought that the *in vivo* species consisted of a dimer of chlorophyll a with unpaired electron spin density distributed equally over the two chlorophyll a macrocycles. Subsequent electron nuclear double resonance (ENDOR) experiments supported this idea; proton hyperfine couplings in P_{700} decreased with respect to the chlorophyll a cation radical monomer models.[19] The dimeric model was challenged, however, by Wasielewski *et al* [20]whose second moment analysis of ^{13}C and ^{2}H enriched PSI reaction centers suggested that P_{700}^{+} consists of a single chlorophyll a macrocycle. Moreover, this analysis also predicted the dimeric nature of P_{865}^{+}, the primary electron donor in bacterial systems, a structure later confirmed by the high resolution crystal structure. The evidence for a monomer has also been corroborated by molecular orbital calculations which have shown that the linewidth of chlorophyll a cation radicals *in vitro* is extremely sensitive to environmental factors, most notably to the strength of ligands bound to the central Mg^{2+} atom.[21] Molecular orbital calculations on chlorophyll a monomers have also shown that the availability of a low lying excited state with decidedly different spin distribution can influence the electronic structure of the radical.[22] Because the proton hyperfine couplings measured by ENDOR are a reflection of the spin density distribution in the radical, they can be affected dramatically by changes in the electronic state of the cation. O'Malley and Babcock[23]

suggested that the decreased proton hyperfine couplings observed for P_{700}^{+} *in vivo* did not occur as a result of electron delocalization over two macrocycles, but instead were the direct result of differences in the composition of the ground-state electronic configuration compared to that of the chlorophyll a *in vitro*. The presence of an energetically accessible excited state led to the idea that interactions of P_{700}^{+} with its protein environment, either through axial ligation of the Mg^{2+} atom or by electrostatic interactions of the radical with nearby charged amino acid residues, could provide the perturbation necessary to mix the ground and excited state molecular orbitals. By mixing 25% of the first excited state orbital with the ground state electronic configuration, O'Malley and Babcock were able to account for the reduced proton hyperfine couplings of P_{700}^{+} observed with ENDOR.

Because the EPR signals from chlorophyll species both *in vivo* and *in vitro* consist of a single resonance line inhomogeneously broadened by the presence of multiple small overlapping hyperfine lines, internal spin redistributions resulting from environmental influences may not be detected if the perturbation occurs at sites that are either invisible to magnetic resonance or whose hyperfine coupling constant is small with respect to the overall linewidth. To overcome this obstacle, many laboratories have used a combination of isotopic enrichment and advanced magnetic resonance techniques to attempt to elucidate the electronic structure of chlorophyll radicals *in vivo* and *in vitro*. ENDOR[24] and electron spin echo envelope modulation (ESEEM)[25] spectroscopies have been used extensively to measure the nitrogen hyperfine and quadrupole interactions in both chlorophyll model compounds and in the primary donors. It was clear from early ESEEM experiments on PSI that the nitrogen hyperfine couplings could only be obtained by using ^{15}N isotope enrichment since modulations observed from PSI reaction centers

containing natural abundance ^{14}N (I=1) were dominated by nitrogen quadrupole interactions whereas the ESEEM spectrum from PSI enriched with ^{15}N (I=1/2) exhibited only nitrogen hyperfine couplings. In ESEEM experiments performed at 77K, Bowman *et al.*[26] used the experimental spectra obtained in conjunction with molecular orbital calculations to estimate the magnitude of the nitrogen hyperfine and quadrupole couplings in chlorophyll a model compounds. These studies were extended to the radical *in vivo* by Astashkin *et al*[27]. and the limits for the isotropic and anisotropic parts of the nitrogen hyperfine coupling originally determined by Norris *et al.*[28] were confirmed.

With the advent of the high resolution crystal structure from bacteria and subsequent single crystal EPR and ENDOR studies, elucidation of the electronic structure of P^+ in the bacterial systems was possible.[29] The unpaired electron was found to be delocalized asymmetrically over the two halves of the bacteriochlorophyll dimer, favoring the L branch by approximately a 2:1 ratio. This asymmetry has been attributed to structural differences in the protein environments of the two bacteriochlorophylls which manifest themselves as shifts in the energy of the highest filled molecular π orbitals of the bacteriochlorophyll monomers and may contribute to the high efficiency of forward electron transfer by moving the hole away from the primary electron acceptor.

Recent ^1H and ^{15}N ENDOR studies on frozen solutions of PSI have indicated either an analogous asymmetric, or completely monomeric, unpaired electron spin density distribution over the chlorophyll a dimer for P_{700}^+.[24,25] However, in systems with multiple anisotropic hyperfine couplings, unequivocal structural assignments from powder pattern ENDOR spectra are difficult to make, as often only the turning points of the hyperfine

coupling tensor are observed and correlation of these components to a specific ^{15}N nucleus is difficult without using specific isotope labeling. Also, the relative intensities of the ENDOR lines are not proportional to the number of coupled nuclei contributing. The modulations observed in an ESEEM experiment, though, are related directly to the relative populations of spin systems in the sample (see Chapter 2 for a complete description of these magnetic resonance techniques). Recent one and two-dimensional ESEEM experiments have been used to measure the ^{14}N hyperfine couplings and nuclear quadrupole interactions in P_{700}^{+}. These parameters were not determined conclusively, since spectral simulations of the experimental data were not successful.

Additionally, ESEEM and ENDOR spectroscopies have been used with site-directed mutagenesis in an attempt to identify the axial ligands of P_{700}^{+} in the protein system.[30] Since the Mg^{2+} atom in the chlorophyll a macrocycle is coordinatively unsaturated, amino acid residues with electron donating capabilities have been suggested as possible ligands; of these residues, histidine is the most likely candidate. The presence of histidine ligands to P^{+} in the bacterial reaction centers, as well as conserved histidine residues in the amino acid sequence of psaB, strengthens this argument. Recently, Cui *et al.*[30] have performed proton ENDOR and ESEEM experiments on mutants of *Chlamydomas reinhardtii* that indicate that the spectroscopic properties of the primary donor in this system are not affected by mutations of his523, a possible ligand to P_{700}. Three mutants were studied: H523Y, substitution of histine with tyrosine; H523Q, a glutamine substitution; and H523L, a leucine substitution. Of these, only the glutamine and leucine mutants were able to grow photoautotrophically, the tyrosine mutant required exogenous acetate to grow photoautotrophically. However, the growth rate of the H523Q

and H523L mutants was decreased with respect to the wild type. All mutants displayed decreased activity when compared to the wild type, in the case of the H523Y mutant, no activity (measured as oxygen uptake) was observed. Additionally, this mutant lacked both an EPR signal and an optical absorption spectrum attributable to P_{700}^{+}, thus confirming electron transport and Western blot assays that indicated a lack of PSI.

Spectroscopic investigations of H523Q and H523L by ENDOR and ESEEM showed no differences in the P_{700}^{+} signals when compared to wild type. Because mutations of the axial ligand to P^{+} in bacterial systems result in the loss of the Mg^{2+} and the generation of a bacteriochlorophyll-bacteriopheophytin heterodimer;[31] it was expected that the mutations of the putative his ligand to P_{700} would result in the generation of a pheophytin. The spin density distribution in a pheophytin molecule differs considerably from that of chlorophyll and this difference should be manifested in the ENDOR and/or ESEEM spectra of P_{700}^{+}.[22] Since no changes in the lineshapes or splittings in the ENDOR and ESEEM spectra were observed, it was concluded that H523 is not a ligand to P_{700}. However, since water is ubiquitous in its role as a chlorophyll ligand; the induced mutations may have allowed water access to the binding site as a bridging ligand, therefore preserving the integrity of the P_{700} structure.[32] Moreover, changes in the ENDOR and/or ESEEM spectra would not be expected unless the coupling of the axial ligand was considerable in magnitude; this idea will be explored in greater detail in Chapter 3.

More recent site-directed mutagenesis experiments and subsequent spectroscopic analysis of a PSII lacking strain of *Chlamydomonas reinhardtii* have indicated that histidine 656 of the psaB polypeptide is the axial ligand to P_{700}.[33] Although no direct

spectroscopic evidence of the ligand was presented, mutations of H656, located in the helix X region of psaB and conserved in all sequences, to Asn or Ser result in changes in the oxidation midpoint potential, electronic structure and optical properties of P_{700}^{+}. Analogous investigations by Lin *et al.*[34] on the bacterial reaction center revealed that changes resulting from mutations altering the ligand environment of the special pair have a drastic impact upon these properties. This led Webber *et al.* to conclude that H656 is close to and most likely a ligand to the central Mg of one chlorophyll of the P_{700} dimer. The conclusion must be considered as tentative and rather weak in the absence of direct spectroscopic support for it.

Although evidence supporting both monomeric and dimeric structures for P_{700}^{+} exists in the literature, the actual geometric and electronic structure of the radical species *in vivo,* until now, has yet to be determined. A complete spectroscopic study of P_{700}^{+},its axial ligands and electronic structure can be found in Chapters 3 and 4.

Electron Transfer in PSII

The initial step in the electron transfer reactions of PSII occurs when a photon of light is absorbed by a light harvesting protein antenna complex (called the LHC) composed of non-covalently bound chlorophyll a, chlorophyll b and carotenoid molecules in higher plants and green algae. These antenna pigments then transfer energy via exciton interaction and Forster transfer to the reaction centers. All of the energy absorbed by the LHC is transferred to P_{680}, the primary electron donor, promoting it to an excited singlet state, which, within 3 picoseconds[35] reduces a nearby pheophytin molecule (Pheo). To

prevent recombination, the $Pheo^-$ quickly (within 300-600 ps)[36] reduces a nearby plastoquinone, Q_A.

The electrons are shuttled out of PS II by electron transfer from Q_A^- to another plastoquinone, Q_B in about 200 μs.[37] An interesting change occurs at this point; the photosynthetic process, previously composed of single electron events, becomes a multielectron process. Q_B^- remains tightly bound in its binding site until a *second* photochemical event reduces it to Q_B^{2-} whereupon it is protonated and released from its binding site as plastoquinol. The plastoquinol is oxidized by cytochrome b_6f and the electrons are transported to PSI by a plastocyanin molecule. The Q_BH_2 is replaced in its binding site by an oxidized quinone from the membrane associated quinone pool.[38]

Recombination between P_{680}^+ and Q_A^- (which occurs with a half time of approximately 100 μs) would be an energetically "wasteful" process. To prevent this recombination, oxidation of Q_A^- or reduction of P_{680}^+ must occur on a timescale competitive with recombination. The electron transfer between Q_A^- and Q_B has been measured to be in the 100-500 μs time range.[38] The reduction of P_{680}^+, therefore must occur in the submicrosecond time range. This reduction, found to be dependent on the oxidation state of the OEC,[39] indicates the presence of a redox active donor that operates as a charge transfer interface between the OEC and P_{680}^+ in an equilibrium that depends on the net charge of the OEC.[39] Barry and Babcock[40] identified this donor as tyrosine 161 of the D1 polypeptide (Y_Z), although under non-physiological conditions other complexes may donate to P_{680}^+. The oxidizing power generated in producing P_{680}^+ must be directed

eventually at water. Tyrosine oxidation, producing the highly oxidizing (E_m^0=1.0 V) $Y_Z^{\bullet}$ radical is a means by which to achieve this.

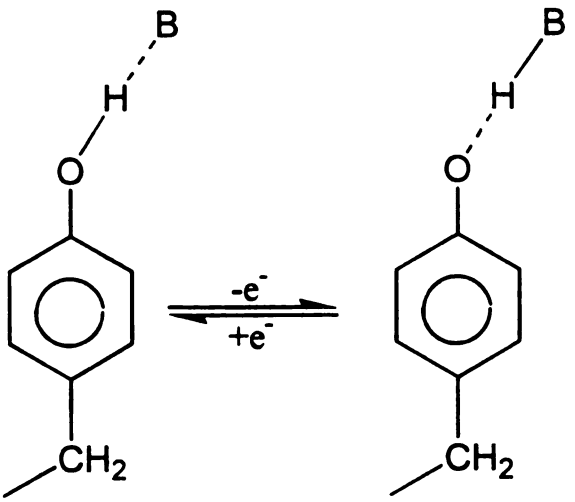

Figure 1-4: Proton "rocking" of YD.

There is a second redox active tyrosine in PS II known as Y_D.[41] It has been identified as Tyr-160 of the D2 polypeptide by site directed mutagenesis experiments, and in its oxidized form, is responsible for the dark stable EPR signal known as Signal II. The fact that Y_D^+ is not involved in the electron transfer reactions that lead to water oxidation was confirmed with site-directed mutagenesis experiments by Debus *et al.*[41] where phenylalanine was substituted for both Y_Z and Y_D. In the Y_Z case, photosynthetic growth was absent after the deletion whereas in the Y_D case photosynthetic growth continued. The two tyrosine moieties are related by an apparent C_2 symmetry. These

symmetry related branches, however, are not related *functionally*, which has interesting fundamental implications.

Insight into the function of these two apparently related moieties has recently been garnered by a series of magnetic resonance experiments on both specifically labeled model tyrosine compounds and on isotopically labeled radicals *in vivo*.[42] The suggestion that Y_D acts purely as an electron transfer cofactor is supported by ENDOR experiments indicating the presence of a well-ordered hydrogen bond.[43] A proton "rocking" motion is therefore proposed for Y_D (Figure 1-4). Y_D is most likely hydrogen bonded to H189(D2)[44] and upon oxidation, the "sense" of the hydrogen bond is reversed, allowing the proton to remain in the site. The hydrophobic environment[45],[43b] of Y_D facilitates this and nuclear motion along the reaction coordinate is minimized, keeping the reorganization energy small and, therefore, maximizing electron transfer rates.

In contrast, the close environment of Y_Z is hydrophilic,[46] facilitating proton movement. Additionally, the lack of a well ordered hydrogen bond as well as increased rotational mobility about the C_β-C_1 bond in Y_Z has provided support for a model where Y_Z acts as a hydrogen atom abstractor in a purely catalytic function.[44,47] This proton "sloughing" model where oxidation is coupled to deprotonation, is shown in Figure 1.5. Studies of proton release patterns of PSII support this hydrogen atom abstraction model, each S state transition is accompanied by a concomitant proton release and the release is coupled to Y_Z oxidation.[48] Site directed mutagenesis experiments have supported this model, as mutations of H190(D1), which facilitates the concerted hydrogen atom transfer upon oxidation of Y_Z by acting as a transient proton acceptor species, have decreased the

rate of P_{680}^{+} reduction by as much as 200 times.[49] The tyrosyl radical produced by this "sloughing" has an essential function in water oxidation (*vide infra*).

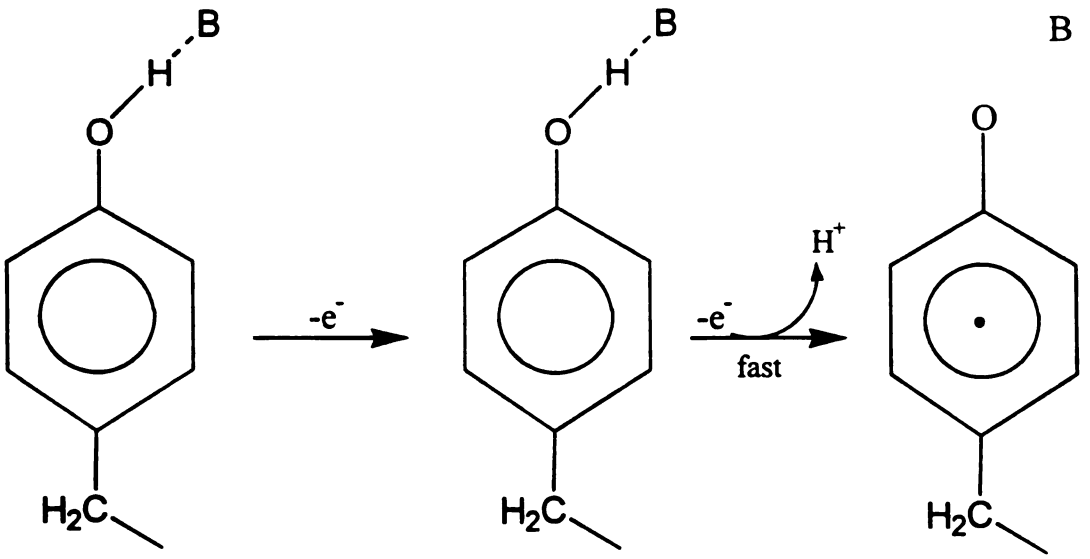

Figure 1-5: Proton "sloughing" of Y_z.

Structure

A better understanding of the functional aspects of the PS II/OEC can be obtained with an in depth discussion of the polypeptides and cofactors associated with this membrane bound complex. There are about twenty polypeptides associated with the PS II/OEC, making it a moderately complex system.[50] This complexity, however, is remarkably easy to resolve biochemically. Detergent solubilization methods have allowed isolation of a number of smaller assemblies which have led to the construction of

a reasonable working model of the PS II/OEC. The proposed architecture of PSII showing relevant polypeptides and cofactors is depicted schematically in Figure 1-6.[50]

The PS II/OEC contains both extrinsic and intrinsic polypeptides as well as a number of enzymatically active cofactors. There are three extrinsic polypeptides, which serve to stabilize the OEC and preserve oxygen evolution capabilities. The 33 kDa protein protects the manganese complex associated with water oxidation by maintaining the structural integrity of the Mn ensemble. Removal of this polypeptide results in the loss of Mn and, consequently, a loss in oxygen evolution capabilities.[51] This polypeptide also binds directly to the intrinsic polypeptides, an interaction further stabilizing the Mn complex. Recent crosslinking studies have determined the stoichiometry of this polypeptide to be 1:1 with an intrinsic polypeptide (the 47 kDa).[52] It also serves an additional function; it isolates the redox active species involved in water oxidation from the aqueous environment. This is an important function in that the water oxidizing system is susceptible to spurious reductants and this biochemical barrier provides a redox shield that allows it to perform its water splitting function successfully. Unfortunately, it is difficult to study quantitatively due to rearrangements of the intrinsic polypeptide core that occur upon removal of these soluble subunits.[53]

The remaining extrinsic polypeptides, the 17 and 23 kDa proteins, also function as binding sites for cofactors necessary for water splitting chemistry, in particular the calcium and chloride ions. These two polypeptides also protect the manganese ensemble from exogenous reductants. Upon removal of these polypeptides, oxygen evolution can only be maintained with increased concentrations of both calcium and chloride.[54]

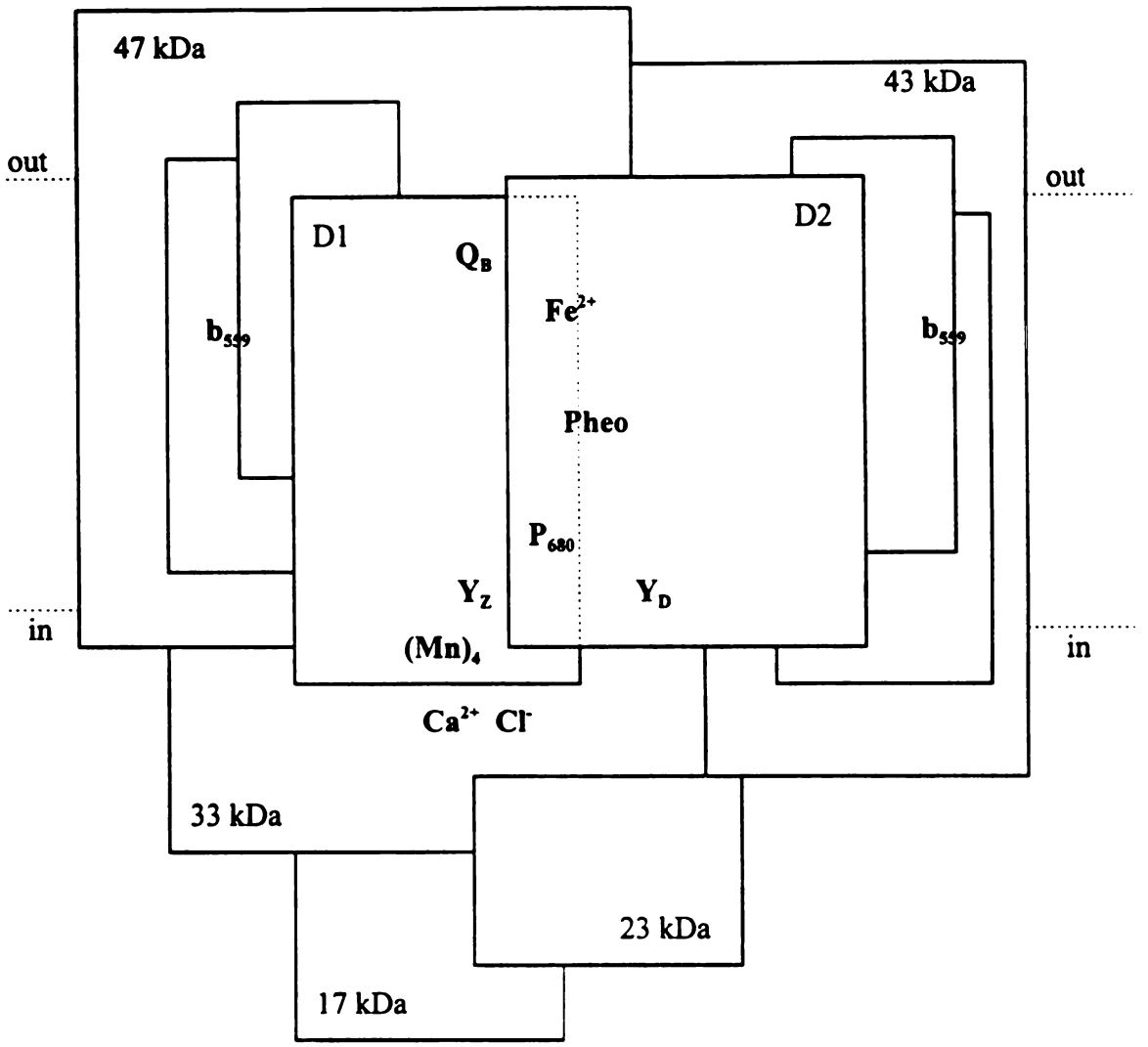

Figure 1-6: Proposed structure of PSII/OEC including polypeptides and cofactors.

The photochemical core of PS II is formed by two membrane spanning intrinsic polypeptides. These heterodimers (MW approximately 32 kDa) , commonly known as D1 and D2, bind the chlorophylls, pheophytins and quinones that mediate the light driven charge separation reactions.[55] Sequence and functional homologies between the L and M subunits of the bacterial reaction center from *Rhodopseudomonas viridis* and the D1/D2 heterodimer have led to the suggestion that D1 and D2 each contain five membrane spanning helices.[56,57] This structural arrangement leads to a pseudo-C_2 symmetry for the PS II/OEC which is broken by the incorporation of the manganese ensemble, proposed to lie off of the C_2 symmetry axis.[58]

The remaining intrinsic polypeptides have a wide variety of functions. By providing binding sites for accessory chlorophylls the 43 and 47 kDa proteins have mainly a light harvesting function. The 23 kDa polypeptide can be isolated in its pure form, and in addition to binding chlorophyll a, has been implicated in maintaining the Q_B site on D1.[59],[60] Conformational changes to D1 are modulated depending on whether this quinone-binding site is occupied. The smaller (22 and 10 kDa) polypeptides do not have binding sites for any of the cofactors. However, upon removal of these two proteins an increased accessibility of exogenous acceptors like DCBQ to Q_A^- has been observed; this leads to the conclusion that these polypeptides influence the environment around these quinones. The final two intrinsic polypeptides (4 and 9 kDa MW) each provide a single histidine ligand to the heme of cytochrome b_{559}.[61]

The Oxygen Evolving Complex

The OEC is the site of water oxidation in the photosynthetic process. The half reaction corresponding to this process,

$$2H_2O \longrightarrow O_2 + 4H^+ + 4e^-$$

has an average reduction potential of 0.93 V at pH=5.0.[62] The energy required to drive this reaction comes from the oxidized P_{680}. The midpoint potential for this reaction

$$P_{680} \longrightarrow P_{680}^{+} + e^-$$

has been estimated to be 1.17 V. The stoichiometries of these two reactions bring up an interesting mechanistic question; a single absorbed photon generates only one oxidizing equivalent, however the water splitting process is a four electron process. The oxidizing power of four photons needs to be combined in order to facilitate water oxidation.

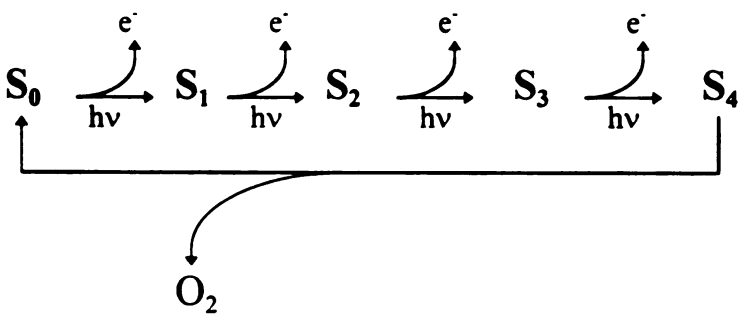

Figure 1-7: The Kok cycle.

Insight into the resolution of this paradox began with the now classic O_2 flash yield measurements of Joliot *et al.*[63] These experiments showed that the O_2 produced by

a sequence of brief (about 10 μs) saturating light flashes showed a damped oscillatory pattern with a periodicity of four following the third flash. These data were soon reproduced by Kok *et al.* and a working kinetic model was established.[64] This model showed that the PS II units function independently in accumulating the four oxidizing equivalents necessary to split water. This so-called S-state cycle is driven by successive photoactivations of PS II. A schematic representation of this cycle is shown in Figure 1-7.

The S represents the water splitting center and the subscripts indicate the number of oxidizing equivalents accumulated. Oxygen evolution occurs only after the S_4 state has been achieved. This model accurately explains the details of the flash experiments. Maximal oxygen evolution occurs after the third flash with repeated maxima after successive four flash intervals which can be explained if both S_0 and S_1 are dark stable states.[64] The oxygen evolution vs. flash pattern eventually dephases and reaches a steady state value. The slow dephasing seen is due to the non-zero probability of "misses" and "double hits" resulting in the loss of S-state coherence.

The mechanism of water oxidation has been long debated. A recent model,[42] based on experimental evidence as well as comparison to other enzyme systems,[65] is presented in Figure 1-8. In this model, the OEC comprises Y_Z , the Mn cluster, Ca^{2+} and Cl^- and involves the repetitive abstraction on each S state transition of protons and electrons from water and OH^- bound as substrates. Each of the components maintains an integral function in the water oxidation mechanism: Y_Z acts to abstract the protons and electrons from substrate water bound to the Mn tetramer; the Mn cluster provides a means

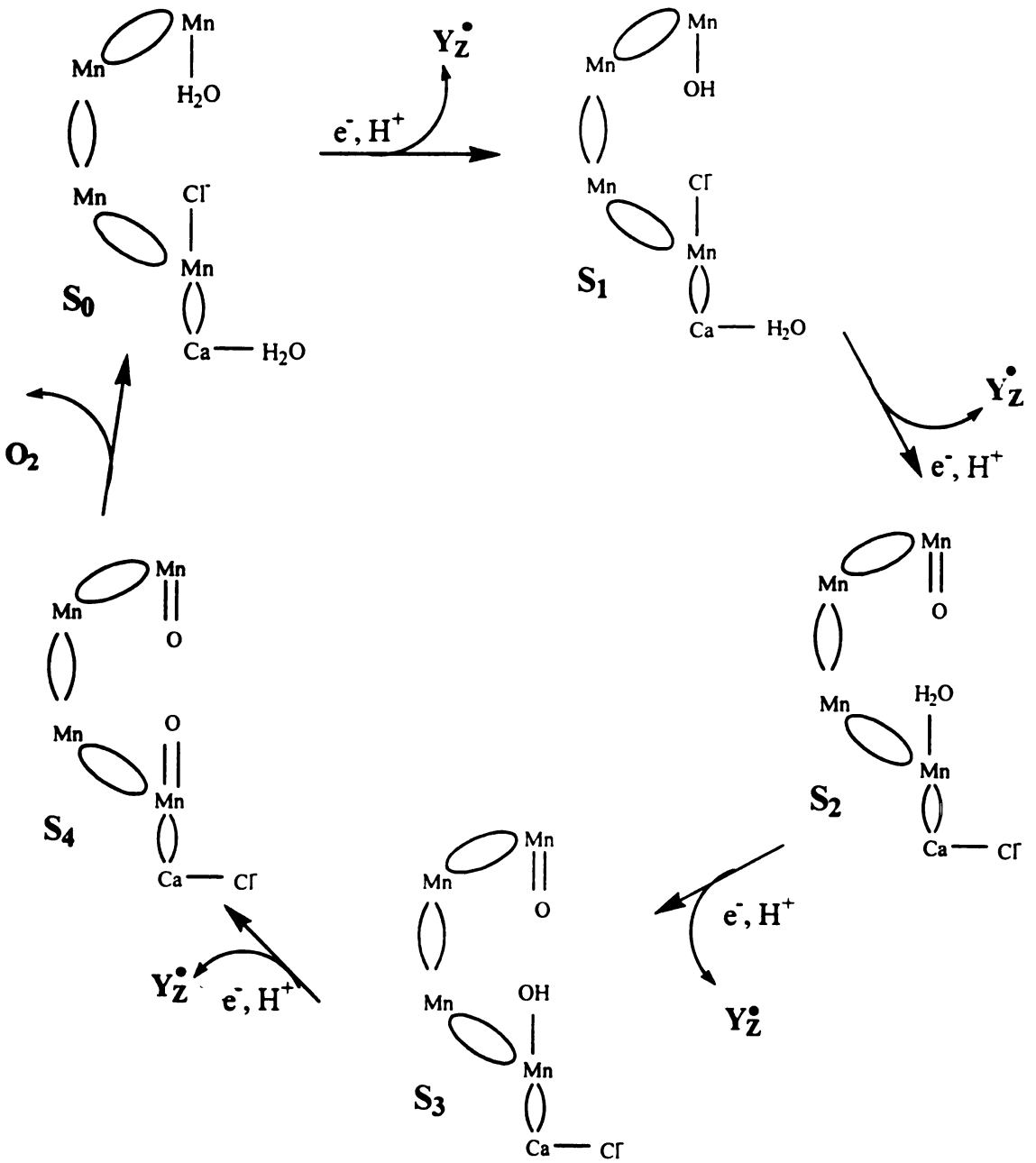

Figure 1-8: Proposed mechanism of water oxidation in PSII.

by which water binding sites are provided as well a site for the delocalization of oxidizing equivalents; and Ca^{2+}/Cl^- prevent the production of potentially toxic or reactive intermediates like peroxides. This model is also attractive because it retains electroneutrality throughout the S state transitions. Water oxidation occurs as a concerted process during the $S_3 \rightarrow S_4 \rightarrow S_0$ transition.

This model is is consistent with recent pulsed ENDOR experiments by Gilchrist *et al.* where the source of the split S_3 EPR signal in Ca^{2+} depleted PSII samples was found to be Y_Z in magnetic contact to the Mn cluster.[66] By measuring the hyperfine coupling of the β methylene protons, and assuming a purely dipolar interaction, the distance between the Mn cluster and Y_Z was estimated to be 4.5 Å This physical proximity is necessary, as studies of other metalloradical enzyme systems have shown that the oxygen activating metal center is usually less than 10 Å from the redox active amino acid.[67]

Manganese

The first row transition metal manganese has long been associated with the oxygen evolving complex of photosynthesis. Its many stable oxidation states (+2 to +7) make it an ideal metal center for the multielectron chemistry that occurs in the OEC. The earliest experiments linking Mn to oxygen evolution were performed in the 1930's and showed that algae grown on low levels of manganese exhibited a decreased ability to evolve oxygen.[68] Later experiments placed the location of manganese directly in PS II. By using heat shock techniques, Cheniae and Martin[69] demonstrated a loss of oxygen

evolution concomitant with the release of Mn. It was later shown that the major fraction of Mn^{2+} in highly oxygen evolving thylakoid membranes was in an EPR silent form.[70] This amount, calculated to be 4 per 400 chlorophyll, was resistant to release by Ca^{2-} and was released by using acidification processes and subsequently quantified with EPR measurements. A stoichiometry of four Mn per PS II was determined for optimum functioning of photosynthetic oxygen evolution. Dimers, trimers and tetramers have all been suggested as structures for this multinuclear cluster. A variety of techniques have been employed to determine the oxidation state changes of this functional Mn ensemble that correspond to S-state transitions.

EPR

Perhaps the greatest amount of information regarding the structure of the Mn ensemble has come from electron magnetic resonance techniques, particularly electron paramagnetic resonance (EPR). EPR is used as a sensitive probe into the electronic and geometric structures of paramagnetic substances; it is particularly useful in protein systems where spectral congestion, the result of multiple interacting nuclei, precludes the application of other structural determination methods. The Mn ensemble in the oxygen evolving complex, as it cycles through the S states, provides a light induced, easily trapped paramagnet (S_2 state) that makes study of the complex especially amenable to EPR. Both continuous wave (cw) and pulsed EPR techniques have been employed to characterize the structure of and ligands to the Mn ensemble.

The first EPR signal associated with the Mn ensemble was reported by Dismukes and Siderer in 1980.[71] This so-called multiline signal was initially observed in samples that had been rapidly frozen following a flash of light at room temperature. The EPR signal consists of 18-20 hyperfine lines separated by 85-90 gauss, is centered at g=1.982 $\pm$ 0.002 and has a linewidth of 1500-1800 gauss, see Figure 1-9, and can only be observed at temperatures less than 35 K. The signal resembles that of synthetic antiferromagnetically coupled Mn(III)Mn(IV) dinuclear clusters.[72] These mixed valence compounds show approximately 16 hyperfine lines which have been attributed to EPR transitions of the two chemically inequivalent ^{55}Mn nuclei. Although the multiline EPR spectrum is broader and has several more resolved transitions, its resemblance to the spectra from this and other mixed valence Mn dinuclear clusters have suggested that the OEC consists minimally of a dinuclear Mn cluster.

The multiline signal amplitude oscillates with flash number, having maximal intensity after the first and fifth flashes. This flash induced periodicity is analogous to the oscillations seen by Joliot and Kok in the S-state experiments and the multiline signal has been attributed to the S_2 state of the Kok cycle.

In addition to the multiline signal, a second EPR signal has been associated with the S_2 state.[73] This signal, in non-oriented samples, appears at g=4.1 and is approximately 1000 G wide with no discernible ^{55}Mn hyperfine structure. The signal appears subsequent to low (140 K vs. 195 K for multiline) temperature illumination and is converted to the multiline signal when PSII samples are warmed to 195 K. This signal is stabilized by increased sucrose concentration and by various O_2 evolution inhibitors, e.g. F^- and small amines.[74,75]

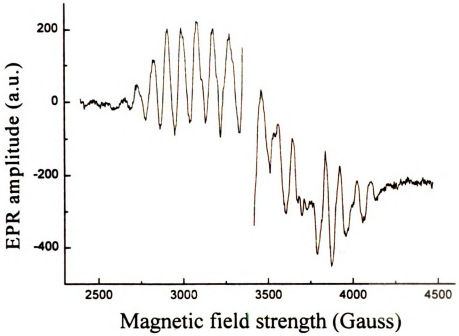

Figure 1-9: Multiline EPR spectrum from reaction center core complexes.

The advancement of the S states was also found to be markedly temperature dependent; S_1---->S_2 can occur at temperatures as low as 130 K and S_2--->S_3 occurs readily only at temperatures above 210 K. Brudvig and coworkers found that a single intense flash of light became progressively less effective in generating the multiline signal at temperatures below 240 K and, at lower temperatures (160 K), continuous illumination was needed.[76]

EXAFS

A number of possible Mn cluster structures have been proposed based on the experimental constraints provided by Extended X-ray Absorption Fine Structure (EXAFS) studies. In EXAFS, backscattering of X-ray generated photoelectrons from the electron charge density of nearby atoms causes modulations of the X-ray absorption cross section as a function of the electron de Broglie wavelength. These modulations can be utilized to determine the distance of the electron density from the parent atom. Since each element has a uniquely defined ionization energy, the results are specific for each element and provide a probe into the protein environment that focuses exclusively on the active site. The only drawback to this technique is that EXAFS cannot distinguish the individual environment of each Mn ion in the cluster, but instead reveals the summation of electron distributions surrounding all four Mn ions.

S_1 has been characterized best by the application of this technique. A strong backscatterer observed at 2.7 Å is consistent with the presence of a first row transition metal like Mn.[77] It is also consistent with Mn-Mn distances measured in di-μ-oxo bridged Mn(III)Mn(IV) model compounds.[78] The presence of a single backscatterer at 2.7 Å lends support for a dimer of dimer model for the OEC.

An additional backscatterer at 3.3 Å is present in the EXAFS data, however definitive assignment of this to a distance *in vivo* has not been made. Evidence identifying this scatterer as arising from either Mn[77] or Ca^{2+}[79] has been presented in the literature. Peaks in the 1.8-2.0 Å range arising from ligands, either nitrogen or oxygen, to

the OEC are also apparent.[77] However, it is not possible to distinguish between these two atoms with EXAFS. Moreover, since this peak contains a sum of all ligands to all Mn ions, definitive assignment of these features to a specific ligand is impossible.

These data have not resulted in a unique structure for the OEC, however they have provided useful constraints for the construction of a likely model. The "dimer of dimer" model described by Klein *et al*[80]. is perhaps the best representation of the geometrical structure of the OEC to date. In this model the dimers are linked via μ–oxo di-μ-carboxlato bridges and the planes of the two dinuclear Mn cores are tilted with respect to the membrane normal, presenting a "C" like structure.

EXAFS has also been used to examine the structural changes in the cluster as a function of the S states. Small changes were observed upon oxidation of the cluster from S1 to S2, indicative of little or no structural changes.[81] Interestingly, though, low temperature illumination resulting in the g=4.1 signal resulted in a change in backscattering from 2.7 Å to 2.8 Å.[82] This is consistent with the structural changes expected with a change in ground spin state (from S=1/2 for the multiline to an S=3/2 or 5/2 for the g=4.1).

X-ray absorption Near Edge Structure (XANES) spectroscopy has also been used to examine the oxidation state changes in the OEC. Shifts in the Mn K edge absorption as a result photoexcitation was used initially as evidence that Mn was being oxidized during the S_1 to S_2 transition.[83] This shift is a manifestation of the additional photon energy necessary to achieve photoionization of the core electrons upon oxidation state changes. Based on XANES data, the current consensus on the oxidation states in the S_1

state is Mn(III)Mn(III)Mn(IV)Mn(IV).[84] Photooxidation to the S_2 state, then, produces a paramagnetic state: Mn(III)Mn(IV)Mn(IV)Mn(IV), which yields an S=1/2 state when antiferromagnetically coupled. The lack of evidence for Mn oxidation during the S_2 to S_3 transition has been interpreted as the oxidation of a nearby amino acid residue. However, it must be pointed out that the EXAFS data indicates a large structural rearrangement upon this transition, and edge shifts are only accurate if the geometry and ligation sphere of the core remain unchanged.

Calcium effects

The role of calcium in PS II has been well documented. Initially observed in photosynthetic membranes from cyanobacteria, calcium requirements have played roles in higher plant photosynthesis as well.[85] Reconstitution of calcium depleted membranes was found to reverse the inhibition of oxygen evolution.[86] Depletion of calcium can be accomplished by salt washing either in the light or dark with 1-2 M NaCl. This treatment removes the 17 and 23 kDa polypeptides and allows access to the proposed calcium site. Salt washing in the light is facilitated by the addition of a chelating agent such as ethylene diamine tetraacetic acid (EDTA). Because illumination was found to have an effect upon the ease of calcium extraction, the role of calcium in PS II was associated with the S-states of the OEC. The ease of extraction progresses in the order $S_3 > S_2 \sim S_0 > S_1$.

The multiline spectrum has been studied to determine the effect of calcium depletion upon S-state turnover. The S-state transition inhibited by calcium depletion has been controversial. Boussac and Rutherford provide evidence for blockage of the S_3 ---> S_0 transition in NaCl washed samples.[87] Continuous illumination of the calcium depleted samples at 200 K results in a normal S_2 multiline signal whose intensity is comparable in amplitude to the signal from calcium reconstituted samples. Flash experiments showed normal multiline formation upon the first flash with a typical decrease in amplitude after the second flash. However, no increase in intensity was observed upon the fifth flash. The typical S-state oscillation pattern was present upon calcium reconstitution of these samples.

Reconstitution of the Ca^{2+} depleted samples with Sr^{2+} restores approximately 60% of the oxygen evolution capabilities of the unperturbed sample. This decrease in catalytic activity has been attributed to a decrease in the rate of the $S_3 \rightarrow (S_4) \rightarrow S_0$ transition. The magnetic properties of the cluster are affected by the Sr^{2+} substitution and the multiline spectrum is modified.[88] These modifications are manifested as losses, splits, shifts and redistributions of the ^{55}Mn hyperfine lines indicative of small perturbations in the OEC structure. Sr^{2+} substitution also stabilizes the g=4.1 signal.[89] I will return in Chapter 5 to a discussion of Ca^{2+} effects in PSII and a study of the multiline signal in samples reconstituted with Sr^{2+}.

Nitrogen ligation

Electron spin echo envelope modulation (ESEEM) techniques were used to observe nitrogen interactions between the Mn complex and a proposed histidine ligand in both cyanobacteria and spinach thylakoid preparations.[90] By studying ammonia inhibition mechanisms in PS II, Britt and coworkers[90b] were able to identify hyperfine and quadrupole frequencies associated with the ^{14}N (I=1) of ammonia. Subsequent isotopic exchange experiments with ^{15}N (I=1/2) were used to confirm the nitrogen from ammonia as the source of these frequencies. Analogous experiments were performed on oxygen evolving cyanobacteria preparations.[90a] Cultures of the cyanobacteria *Synechococcus* were grown with KNO_3 as their only source of nitrogen. Again, hyperfine and quadrupole frequencies were determined by using ESEEM spectroscopy. Isotope labeling experiments confirmed nitrogen as the origin of these frequencies.

LIST OF REFERENCES

LIST OF REFERENCES

[1] For reviews see: a) Golbeck, J. (1992) *Annu. Rev. Plant Physiol. Plant Mol. Biol. 43*, 293 b) Malkin, R. (1996) in *Advances in Photosynthesis* (Ort, D. & Yocum, C.F., eds.) Kluwer, Dordrecht, in press.

[2]For reviews see: Diner, B.A. & Babcock, G.T. (1996) in *Advances in Photosynthesis* (Ort, D. & Yocum, C.F., eds.) Kluwer, Dordrecht, in press. b) Britt, R.D. (1996) in *Advances in Photosynthesis* (Ort, D. & Yocum, C.F., eds.) Kluwer, Dordrecht, in press.

[3] Hill, R. & Bendell, F. (1960) *Nature 186*, 136.

[4] Staehelin, L.A. (1986) in Encyclopedia of Plant Physiology, New Series, Vol. 19, Photosynthesis III (Staehlin, L.A. & Arntzen, C.J., eds.) Springer Verlag, Berlin, 476.

[5] For review, see Malkin, R. (1992) *Photosynth. Res. 33*, 121.

[6] Setif, P. (1992) in *The Photosystems: Structure, Function and Molecular Biology* (Barber, J., ed.) Elsevier, B.V., 471.

[7] Andersen, B., Koch, B., Scheller, H. V., Okkels, J.S., Moller, B.L. (1990) in *Current Research in Photosynthesis* (Batscheffsky, M., ed.) Kluwer, Dordrecht, 671.

[8] Golbeck, J.H.& Cornelius, J.M. (1986) *Biochim. Biophys. Acta 849*, 16.

[9] Kossel, H., Dory, I., Istvan, G. & Maier, R. (1990) *Plant Mol. Biol. 15*, 497.

[10] a) Krauss, N., Hinrichs, W., Witt, I., Fromme, P., Pritzkow, W., Dauter, Z., Betzel, C., Wilson, K.S., Witt, H.T. & Saenger, W. (1993) *Nature 361*, 326. b) Schubert, W.D., Klukas, O., Kraub, N., Saenger, W., Fromme,P. & Witt, H.T. (1995) in *Photosynthesis: from Light to Biosphere, Vol. III* (Mathis, P., ed.) Kluwer, Dordrecht, 3.

[11] Moenne-Loccoz, P., Robert, B., Ikegami, I. & Lutz, M. (1990) *Biochemistry 29*, 4740.

[12] Ratajczak, R. Mitchell, R. & Haehnel, W. (1988) *Biochim. Biophys. Acta 933*, 306.

[13] Ikegami, I. & Itoh, S. (1989) *Biochim. Biophys. Acta 934*, 39.

[14] See, for example, a) Astashkin, A.V., Dikanov, S.A. & Tsvetkov, Yu. D. (1988) *Chem. Phys Lett. 152*, 258 b) Kab, H., Fromme, P. & Lubitz, W. (1996) *Chem. Phys. Lett. 257*, 197.

[15] Deisenhofer, J., Epp, O., Miki, K., Huber, R. & Michel, H. (1985) *Nature 318*, 618.

[16] Allen, J.P., Feher, G., Yeates, T.O., Komiya, H. & Rees, D. (1987) *Proc. Natl. Acad. Sci. USA 84*, 5730.

[17] Commoner, B., Heise, J.J. & Townsend, J. (1956) *Proc. Natl. Acad. Sci. USA 42*, 710.

[18] Norris, J.R., Uphaus, R.A., Crespi, H.L. & Katz, J.J. (1971) *Proc. Natl. Acad. Sci. USA 68*, 625.

[19] Davis, M.S., Forman, A. & Fajer, J. (1979) *Proc. Natl. Acad. Sci. USA 76*, 4170..

[20] Wasielewski, M.R., Norris, J.R., Crespi, H.L. & Harper, J. (1981) *J. Am. Chem. Soc. 103*, 7664.

[21] Fajer, J., Davis, M.S., Brune, D.C., Spaulding, L.D., Borg, D.C. & Forman, A. (1977) *Brookhaven Symp. Biol. 28*, 74.

[22] Petke, J.D., Maggiora, G.M., Shipman, L.L. & Christoffersen, R.E. (1980) *Photochemistry and Photobiolog 31*, 243.

[23] O'Malley, P.J. & Babcock, G.T. (1984) *Proc. Natl. Acad. Sci. USA 81*, 1098.

[24] Kab, H., Bittersmann-Weidlich, E., Andreasson, L.-E., Bonigk, B. & Lubitz, W. (1995) *Chem. Phys. 194*, 419.

[25] a) Davis. I.H., Heathcote, P., MacLachlan, D.J. & Evans, M.C.W. (1993) *Biochim. Biophys. Acta 1143*, 183 b) Kab, H. & Lubitz, W. (1996) *Chem. Phys. Lett. 251*, 193.

[26] Bowman, M.K., Norris, J.R., Thurnauer, M.C., Warden, J., Dikanov, S.A. & Tsvetkov, Yu. D. (1978) *Chem. Phys. Lett. 55*, 570.

[27]. Astashkin, A.V., Dikanov, S.A., Tsvetkov, Yu. D. & Goldfeld, M.G. (1987) *Chem. Phys. Lett. 134*, 438.

[28] Norris, J.R., Uphaus, R.A., Crespi, H.L. & Katz, J.J. (1971) *Proc. Natl Acad. Sci. USA 68*, 625.

[29] a) Lendzian, F., Lubitz, W., Scheer, H., Hoff, A.J., Plato, M., Trankle, E. & Mobius, K. (1988) *Chem. Phys. Lett. 148*, 377. b) Lendzian, F., Huber, M., Isaacson, R.A., Endeward, B., Plato, M., Bonigk, B., Mobius, K., Lubitz, W. & Feher, G. (1995) *Biochim. Biophys. Acta 1183*, 139.

[30] Cui, L., Bingham, S.E., Kuhn, M., Kass, H., Lubitz, W. & Webber, A.N. (1995) *Biochemistry 34*, 1549.

[31] Schenck, C.C., Gaul, D., Steffen, M., Boxer, S.G., McDowell, L., Kirmaier, C. & Holten, D. (1990) in *Reaction Centers of Photosynthetic Bacteria* (Michel-Beyerle, M.E., ed.) Springer-Verlag, Berlin, 229.

[32] Goldsmith, J.O., King, B. & Boxer, S.G. (1996) *Biochemistry 35*, 2421.

[33] Webber, A.N., Su, H., Bingham, S.E., Kass, H., Krabben, L., Khun, M., Jordan, R., Schlodder, E. & Lubitz, W. (1996) *Biochemistry*, in press.

[34] Lin, S., Murchison, H.A., Nagarajan, V., Parson, W.W., Williams, J.C. & Allen J.P. (1994) *Proc. Natl. Acad. Sci USA 91*, 10265.

[35] Schatz, G.H., Brock, H. & Holzwarth, A.R. (1988) *Biophys. J. 54*, 397.

[36] Nuijs, A.M., van Gorkom, H.J., Plijter, J.J. & Duysens, L.N.M. (1986) *Biochim. Biophys. Acta 848*, 167.

[37] Hansson, O. & Wydrzynski, T. (1990) *Photosynthesis Res. 23*, 131.

[38] Crofts, A.R. & Wraight, C.A. (1983) *Biochim. Biophys. Acta 726*, 149.

[39] Witt, H.T.,Schlodder, E., Brettel, K., and Saygin, O. (1986) *Photosynth. Res., 10,* 453.

[40]Barry, B.A. and Babcock, G.T. (1987) *Proc. Natl. Acad. Sci. U.S.A., 84,* 7099.

[41] Debus, R.J., Barry, B.A., Babcock, G.T., and McIntosh, L. (1988) *Proc. Natl. Acad. Sci. U.S.A., 85*, 427.

[42] Hoganson, C.W., Lydakis-Simantiris, N., Tang, X.-S., Tommos, C., Warncke, K., Babcock, G.T., Diner, B.A., McCracken, J. & Styring, S. (1995) *Photosynthesis Research 46*, 177.

[43] Reviewed in a) Barry, B.A. (1993) Photochem. Photobiol. 57, 179. b) Hoganson, C.W. and Babcock, G.T. (1994) Photosystem II: in *Metal Ions in Biological Systems, Vol. 30* (Sigel, H. and Sigel, A., eds.) Marcel-Dekker, New York, 77.

[44] a) Tang, X.-S., Zheng, M., Chisholm, D.A., Dismukes, G.C. & Diner, B.A. (1995) Biochemistry, submitted. b) Tommos, C., Tang, X.-S., Warncke, K., Hoganson, C.W., Styring, S., McCracken, J., Diner, B.A. & Babcock, G.T. (1995) *J. Am. Chem. Soc. 117*,10325.

[45] Svensson, B., Vass, I. & Styring, S. (1991) *Z. Naturforsch 46c*, 765.

[46] Svensson, B., Vass, I., Cedergren, E. & Styring, S. (1990) *EMBO J 9*, 2051.

[47] Warncke, K. & McCracken, J. (1995) *J. Chem. Phys. 103*, 6829.

[48] Lubbers, K., Haumann, M. & Junge, W. (1993) *Biochim. Biophys. Acta 1183*, 210.

[49] a) Diner, B.A., Nixon, P.J. & Farchaus, J.W. (1991) *Curr. Op. Struct. Biol. 1*, 546. b) Tang, X.-S., Chisholm, D.A., Dismukes, G.C., Brudvig, G.W. & Diner, B.A. (1993) *Biochemistry 32*, 13742. c) Kramer, D.M., Roffey, R.A., Govindgee & Sayre, R.T. (1994) *Biochim. Biophys. Acta 1185*, 228. d) Roffey, R.A., Van Wijk, K.J., Sayre, R.T. & Styring, S. (1994) *J. Biol. Chem. 269*, 5115.

[50] Babcock, G.T., Barry, B.A., Debus, R.J., Hoganson, C.W., Atamian, M., McIntosh,L., Sithole, I., and Yocum, C.Y. (1989) *Biochemistry, 28,* 9557

[51] Ghanotakis, D.F., Topper, J.N. and Yocum, C.F. (1984) *Biochim Biophys Acta 767,* 524.

[52] Enami, I., Kaneko, M., Kitamua, N., Koike, H., Sonoike, K., Inoue, Y., and Katoh, S. (1991) *Biochim Biophys Acta, 1060,* 224.

[53] Hoganson, C.W., Babcock, G.T., and Yocum, C.F. (1989) *Photosynth. Res., 22,* 285.

[54] Nakatani, H.Y. (1984) *Biochim. Biophy. Res. Commun., 120,* 299.

[55] Nanba, O. and Satoh, K. (1987) *Proc. Natl. Acad. Sci. U.S.A., 84*, 109.

[56] Diesenhofer, J., Epp, O., Miki, K., Huber, R., and Michel, H. (1985) *Nature 318,* 618.

[57] Sayre, R.T., Andersson, B., and Bogorad, L. (1986) *Cell, 47*, 601.

[58] Rutherford, A.W. (1989) *Trends. Biochem. Sci., 14 (6)*, 227.

[59] Ghanotakis, D.F., Demetriou, D.M., and Yocum, C.F. (1987) *Biochim. Biophys. Acta, 891,* 15.

[60] Bowlby, N.R., Ghanotakis, D.F., Yocum, C.F., Petersen, J., and Babcock, G.T.,(1988) *Light Energy Transduction in Photosyntheisi: Higher Plant and Bacterial Models* (Stevens, S.E. Jr., and Bryant, D.A., Eds.) p. 215, The American Society of Plant Physiology Publishers, Baltimore, MD.

[61] Babcock, G.T., Widger, W.R., Cramer, W.A., Oertling, W.A., and Metz, J.G. (1985) *Biochemistry, 24,* 3638.

[62] Klimov, V.V., Allakhverdiev, S.I., Demeter, S., Krasnovskii, A.A. (1980) *Dokl.Akad. Nauk. SSSR, 249,* 227.

[63] Joliot, P., Barbieri, G., and Chabaud, R. (1969) *Photochem. Photobiol., 10,* 309.

[64] Kok, B., Forbush, B., and McGloin, M. (1970) *Photochem. Photobiol., 11,*457.

[65] Sigel, H. & Sigel, A. (1994) (eds.) in *Metal Ions in Biological Systems, Vol. 30,* Marcel-Dekker, New York.

[66] Gilchrist Jr., M.L., Ball, J.A., Randall, D.W. & Britt, R.D. (1995) *Science*, submitted.

[67] Picot, D., Loll, P.J. & Garavito, R.M. (1994) *Nature 367*, 243.

[68] Pirson, A. (1937) *Z. Bot. 31,* 193.

[69] Cheniae, G.M. and Martin, I.F. (1966) *Brookhaven Symp. Biol. 19,* 406.

[70] Yocum, C.F., Yerkes, C.T., Blankenship, R.E., Sharp, R.R., and Babcock, G.T. (1981) *Proc. Natl. Acad. Sci. U.S.A., 78,* 7507.

[71] a) Dismukes, G.C. and Siderer, Y. (1980) *FEBS Lett., 121,* 78. b) Dismukes, G.C. and Siderer, Y. (1980) *Proc. Natl. Acad. Sci. U.S.A.,78,* 274.

[72] Cooper, S.R., Dismukes, G.C., Klein, M.P. & Calvin, M. (1978) *J. Am. Chem. Soc. 100*, 7248.

[73] Zimmerman, J.L. & Rutherford, A.W. (1986) *Biochemistry 25*, 4609.

[74] Casey, J. & Sauer, K. (1984) *Biochim. Biophys. Acta 767*, 21..

[75] a) Beck, W.F. & Brudvig, G.W. (1986) *Biochemistry 25*, 6747 b) Beck, W.F. & Brudvig, G.W. (1988) *Chemica Scripta 28A*, 93.

[76] Brudvig, G.W., Casey, J.L., and Sauer, K. (1983) *Biochim. Biophys. Acta, 723*.366.

[77] Penner-Hahn , J.E., Fronko, R.M., Pecoraro, V.L., Yocum, C.F., Betts, S.D. & Bowlby, N.R. (1990) *J. Am. Chem. Soc. 112*, 2549.

[78] Sauer, K., Yachandra, V.K., Britt, R.D. & Klein, M.P. (1992) in Manganese Redox Enzymes (Pecoraro, V.L., ed.) VCH Publishers, New York, 141.

[79] Latimer, M.J., DeRose, V.J., Mukerji, I., Yachandra, V.K., Sauer, K. & Klein, M.P. (1995) *Biochemistry 34*, 10898.

[80] Yachandra, V.K., DeRose, V.J., Latimer, M.J., Mukerji, I., Sauer, K. & Klein, M.P. (1993) *Science 260*, 675.

[81] A) DeRose, V.J., Mukerji, I., Latimer, M.J., Yachandra, V.K., Sauer, K. & Klein, M.P. (1994) *J. Am. Chem. Soc. 116*, 5239 b) Mukerji,I., Andrews, J.C., DeRose, V.J., Latimer, M.J., Yachandra, V.K., Sauer, K. & Klein, M.P. (1994) *Biochemistry 33*, 9712.

[82] Liang, W., Latimer, M.J., Dau, H., Roelofs, T.A., Yachandra, V.K., Sauer, K. & Klein, M.P. (1994) *Biochemistry 33*, 4293.

[83] Goodin, D.B., Yachandra, V.K., Britt, R.D., Sauer, K. & Klein, M.P. (1984) *Biochim. Biophys. Acta 767*, 209.

[84] Riggs, P.J., Mei, R., Yocum, C.F. & Penner-Hahn, J.E. (1992) *J. Am. Chem. Soc. 114*, 10650.

[85] England, R.R. and Evans, E.H. (1981) *FEBS Lett., 143*, 175.

[86] Ghanotakis, D.F., Babcock, G.T., and Yocum, C.F. (1984) *FEBS Lett., 167*, 127.

[87] Boussac, A. and Rutherford, A.W. (1990) *FEBS Lett., 277*, 69.

[88] Ghanotakis, D.F., Babcock, G.T., and Yocum, C.F. (1984) .*Biochim. Biophys. Acta,, 765*, 388.

[89] Boussac, A. & Rutherford, A.W. (1988) *Biochemistry 27*, 3476.

[90] a) DeRose, V.J., Yachandra, V.K., McDermott, A.E., Britt, R.D., Sauer, K., and Klein, M. (1990) *Biochemistry, 30*, 1335. b) Britt, R.D., Zimmerman, J.L., Sauer,K., and Klein, M. (1989)*J. Am. Chem. Soc.,111*,3522

Chapter 2

Electron Magnetic Resonance Theory

Although the intellectual environment prior to the first reported electron paramagnetic resonance (EPR) spectrum in 1945 by Zavoisky was favorable for the development of EPR methodology, significant advancements in the technique did not occur until the advent of available microwave technology following World War II. Subsequent improvements in pulse generators, stable microwave sources, amplifiers and the recent development of a commercial instrument have similarly catalyzed the growth of pulsed-EPR as an effective and applicable spectroscopic tool.

Electron magnetic resonance spectroscopy has been used successfully in chemistry and physics to understand electronic and geometric structures in a plethora of systems encompassing fields from biophysics to material science. The presence of stable, easily trapped paramagnetic species in photosynthetic systems makes them especially amenable to the application of these techniques. This chapter will provide a basic introduction to the theory behind these EPR techniques and is not meant to be a comprehensive review; a number of excellent treatises[1] and textbooks[2] have been dedicated to the complete theoretical description of magnetic resonance spectroscopy.

EPR

Electromagnetic radiation is composed of mutually perpendicular oscillating electric and magnetic fields. Interaction of these fields with molecular species initiates transitions between energy levels, which provides information regarding both geometric

and electronic structure. These transitions are observed only if the incident photon has sufficient energy to bridge the gap between energy levels and the interaction perturbs either an electric or magnetic dipole present in the sample. In EPR, the interaction of the electron magnetic moment with the magnetic field component of the electromagnetic radiation is of primary interest. The energy levels corresponding to different orientations of these magnetic moments are normally degenerate, however, the presence of an externally applied static magnetic field effectively splits the degeneracy of these spin states and, upon introduction of oscillating electromagnetic radiation, allows observation of an absorption attributable to a magnetic interaction. This interaction is the basic tenet of both EPR and nuclear magnetic resonance (NMR) spectroscopy.

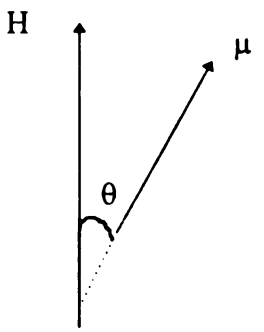

Figure 2-1: The interaction of the applied magnetic field **H**, with the magnetic moment, μ.

The macroscopic magnetic moment present in a paramagnetic material is the physical manifestation of the presence of electron spin. The classical energy of this magnetic dipole moment in a magnetic field is given by

$$E = -\vec{\mu} \bullet \vec{H}$$

where μ is a vector describing the macroscopic magnetic moment and has contributions from both spin and orbital angular momentum and **H** is the applied magnetic field strength (see Figure 2-1). Because electrons follow quantum rather than classical mechanics, μ is replaced in this expression with the appropriate spin operator to yield the Hamiltonian for an electron in a field

$$\mathcal{H} = g_e \beta \hat{S} \bullet \vec{H}$$

where β, the electron Bohr magneton, is equal to the magnetic moment for a single unit of quantum mechanical angular momentum, and g, the electronic g factor, represents, from a classical viewpoint, the correction factor for the anomalous magnetic moment of the electron (*vide infra*). Application of a static magnetic field along z with magnitude H_0 will quantize the spins along this direction and allow substitution of S_z for **S**. The scalar product, therefore, simplifies to

$$\mathcal{H} = g_e \beta S_z H_0 .$$

The eigenvalues of this Hamiltonian are the eigenvalues of the operator S_z; these eigenvalues, M_s, for an electron are + ½ (α state) and - ½ (β state). This so-called electronic Zeeman splitting results in the formation of two energy states that are degenerate at zero field, and whose separation increases linearly with increasing magnetic field.

The g value accounts for the coupling of spin and orbital angular momentum and is given by

$$g_J = \frac{3J(J+1) + S(S+1) - L(L+1)}{2J(J+1)}$$

where J represents the total angular momentum of the system, S the spin angular momentum and L the orbital angular momentum. For the free electron, $g_e = 2.00232$. In the photosynthetic systems studied in this thesis, the electronic g factor is near g_e and very nearly isotropic. This assumption of an isotropic g value is upheld throughout this discussion and the data analysis in Chapters 3-4.

Although the quantum mechanical representation of a magnetic moment interacting with a field gives a mathematically complete description of the interaction, a more "classical" approach can assist with visualization of the physical motion of the magnetic moment. Classically, Newton's third law for rotational motion states that the rate of change of angular momentum in a system is equal to the torque. For the electron with magnetic moment μ this relationship can be written

$$\frac{d\bar{\mu}}{dt} = -g_e \beta \left(\bar{H} \times \bar{\mu}\right).$$

If H is applied parallel to the z direction with magnitude H_0, then the solutions of this differential equation describe precession about the z axis with a characteristic Larmor frequency, ω_0. This precession provides a physical picture of the motion and is also consistent with the properties of quantum mechanical angular momentum in that the z component of the motion is sharply defined, while the x and y components oscillate about some average value; this behavior is reflected in the commutator relationships found for the spin angular momentum operators.

Transitions between energy levels can be effected provided that the photon energy, $h\nu$, is equal to the energy splitting between levels, ΔE,

$$\Delta E = h\nu = g_e \beta H .$$

This is the basic resonance condition for a free electron. Because of the narrow bandedness of available low noise microwave sources, the typical EPR experiment is performed by holding the microwave frequency constant and sweeping the magnetic field until the resonance condition is met.

Microwave radiation is used to provide the energy necessary to effect these transitions. The magnetic field component of this radiation interacts with the electron's magnetic moment much in the same way as the static field does. This field, H_1 ($H_1 << H_0$) rotates about z with precessional frequency ω. If this precessional frequency matches exactly the Larmor frequency of the magnetic moment, then the magnetic moment will experience a constant field in the xy plane and will precess about this with frequency

$$\omega_1 = g_e \beta H_1 .$$

Since $\omega_1 << \omega_0$, the magnetic moment will spiral down until its projection on -z has the same value that it had on +z. This oscillatory motion between +z and -z will continue as long as H_1 remains on; the frequency of these oscillations is ω_0.

Although this classical description of the behavior of a magnetic moment in an applied magnetic field does not rigorously hold for quantum mechanical particles, a requirement of which is the discrete exchange of energy and matter, it does lend insight into the physical manifestations of this behavior. For example, the application of an oscillating magnetic field applied perpendicularly to an applied field containing an oriented magnetic moment can cause changes in the value of the projection of that

magnetic moment and this reorientation occurs only if the oscillating radiation is in resonance with the natural frequency of the system.

The relative populations in each of the spin states at thermal equilibrium lends insight into the form of the EPR spectrum obtained experimentally and can be calculated by using the Boltzmann expression

$$\frac{N_{upper}}{N_{lower}} = \exp\left\{-\Delta E/kT\right\} = \exp\left\{-\left(g_e \beta H/kT\right)\right\}.$$

At room temperature and 3400 G this ratio is 7.6×10^{-4}. This population difference is essential in observing the resonance phenomenon since transitions are effected with equal probability upward and downward. If the populations of the two states were equal, as much energy would be emitted as absorbed and no net effect would be observed. Since there are more spins in the lower spin state, a net absorption is measured in EPR.

The power of the incident microwave radiation can alter the intensity of the EPR absorption. To understand this qualitatively, the differences in the relative populations of the spin levels as a function of microwave power will need to be examined. Transitions between spin states are driven more rapidly as the power of the incident radiation is increased. This, initially, will result in an increase in absorption as more transitions are effected. However, for inhomogeneously broadened lines, this increase in intensity will ultimately level off and eventually decrease as the transition rate becomes competitive with relaxation pathways. As a result of this, the relative populations in the two spin states becomes equivalent and no net absorption is observed. This phenomenon, known

as "saturation," can be avoided by performing intensity vs. power studies and choosing a non-saturating power at which to perform the experiments.

The expressions derived above describe the energies of electron spin states in an applied magnetic field. If this was the only interaction present, EPR spectroscopy could be used only to detect the presence, and perhaps the kinetics, of paramagnetic species. However, there are always magnetic fields within the paramagnetic substances that interact with the electron spin moment to perturb the resonance. The ensuing complexity of the energy levels as a result of these interactions is manifested in the experimental EPR spectrum as splittings or alterations in the frequency or linewidth of the absorption. The EPR spectrum is therefore interpreted as the allowed transitions between the eigenstates of a spin Hamiltonian that consists of terms indicative of these interactions. For the photosynthetic systems studied, this spin Hamiltonian, operating on the spin only part of the electronic wavefunction, is of the form

$$\mathcal{H} = \mathcal{H}_{ez} + \mathcal{H}_{nz} + \mathcal{H}_{hf} + \mathcal{H}_{nqi}$$

where $\mathcal{H}_{ez}$ is the Hamiltonian for the electronic Zeeman interaction, $\mathcal{H}_{nz}$ the nuclear Zeeman Hamiltonian, $\mathcal{H}_{hf}$ the Hamiltonian for the electron-nuclear hyperfine interaction and $\mathcal{H}_{nqi}$ represents the Hamiltonian for the nuclear quadrupole interaction. Although there are other interactions that can contribute to this spin Hamiltonian, only those terms directly relevant to the systems studied in this thesis have been included. The energies of the states can be evaluated by applying the spin Hamiltonian composed of the electronic Zeeman, nuclear Zeeman and hyperfine terms. These energies and the corresponding energy level diagram for an S= ½ , I= ½ system are shown in Figure 2-2. This figure is

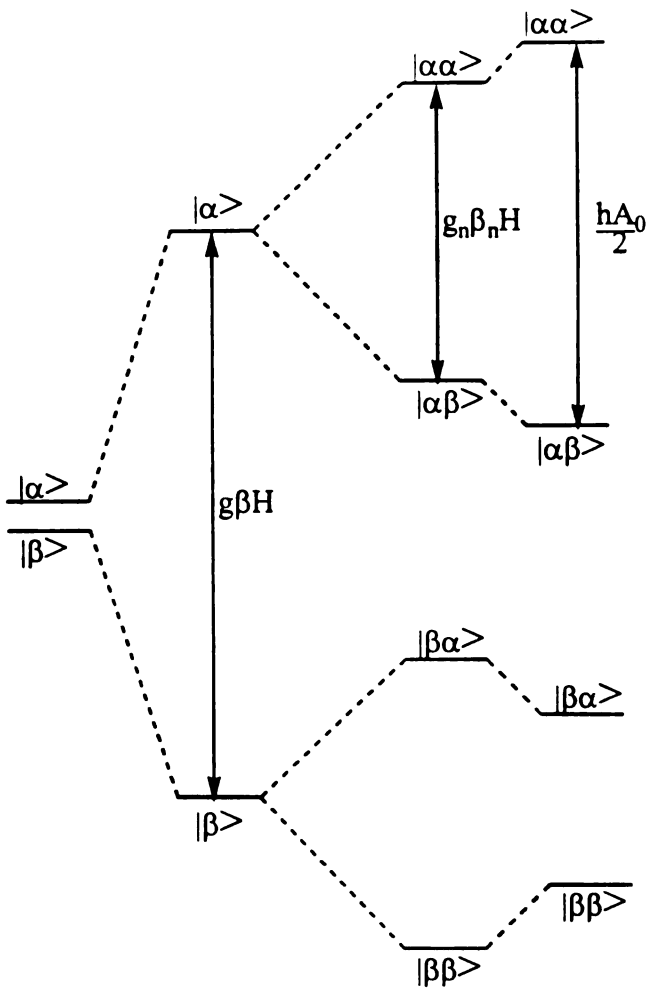

Figure 2-2: Energy level diagram for an S=1/2, I=1/2 spin system.

representative of the chlorophyll species studied in Chapters 3 and 4 of this thesis. In these systems, the unpaired electron is delocalized in a π molecular orbital, and is coupled to an ^{15}N (I= ½) nucleus on a ligated histidine residue through the electron-nuclear hyperfine interaction. The interaction is nearly isotropic and represents coupling through a covalent bond. This energy level diagram will also be utilized later in this chapter to understand the ENDOR spectrum arising from this chlorophyll species.

The electronic Zeeman term of the Hamiltonian acts on the electron spin and represents the interaction of the electron magnetic moment with the field. The resulting energy levels representing the M_s=+ ½ (or $|\alpha>$ state) and M_s =- ½ (or $|\beta>$ state) spin manifolds and transitions were previously described and are shown in Figure 2-2.

The magnetic field also has an effect on the magnetic moments from nuclei with nonzero spin ($I \neq 0$) present in a sample. The second term in the spin Hamiltonian represents the nuclear Zeeman interaction and is given explicitly by

$$\mathcal{H}_{nz} = -g_n \beta_n \vec{H} \bullet \hat{I}.$$

This Hamiltonian is analogous to the electronic Zeeman interaction described above. The nuclear spin quantum numbers M_I, are valid if the static field is applied parallel to the z direction, the corresponding energies are given by

$$E = -g_n \beta_n H M_I$$

For an I = ½ nucleus, this yields two energy levels for M_I = + ½ ($|\alpha_n>$) and M_I = - ½ ($|\beta_n>$, see Figure 2-2). This interaction is approximately three orders of magnitude *smaller* than the analogous electronic Zeeman interaction. This is due to the difference in relative masses of the proton and electron. Because of this difference, transitions between nuclear

state

prob

elec

hyp

free

mo

mag

typ

is i

orb

hov

dis

ma

wh

an

hy

are

Fig

ele

states can be effected by photons in the radiofrequency range. These transitions can be probed by using NMR techniques.

The third term in the Hamiltonian describes the interaction between the unpaired electron and magnetic ($I \neq 0$) nuclei in the system. The magnitude and form of this hyperfine interaction is a direct reflection of the electronic and geometric structure of the free radical and originates from the fact that the interaction of the electron's magnetic moment with the external magnetic field is modulated by the presence of fluctuating magnetic fields induced by nuclear magnetic moments. These interactions are of two types, a contact interaction and a dipole-dipole interaction. The Fermi contact interaction is isotropic and arises from electron spin localized at the nucleus. Only the spherical s-orbital has a nonzero probability, $\Psi^*(0)\Psi(0)$, of the electron being located at the nucleus, however, for orbitals with $\ell \neq 0$, $\Psi^*(0)\Psi(0)$ is non-zero and this contact interaction disappears. The energy for the isotropic interaction between the electron and nuclear magnetic moments can be obtained from solving the Hamiltonian for the interaction

$$\mathcal{H}_{hf(iso)} = A_0 \hat{S} \bullet \hat{I}$$

where $A_0=(8\pi/3)\, g_e g_n \beta_e \beta_e |\Psi(0)|^2$. The z components of the electronic and nuclear spin angular momentum operators can be substituted in place of $\hat{S} \bullet \hat{I}$, providing that the hyperfine interaction is less than the electronic Zeeman interaction, the ensuing energies are then given by

$$E_{iso} = A_0 M_s M_I$$

Figure 2-2 shows the energy level splittings incorporating this term in addition to the electronic and nuclear Zeeman terms.

The isotropic coupling corresponding to this energy can be related to the unpaired electron spin density distribution in the molecule and arises, in part, from the phenomenon of spin polarization that is induced by the presence of an unpaired electron in a p orbital. For example, in the $C_\alpha H$ radical fragment, Hund's Rule predicts that the state with the highest spin multiplicity will be the ground state. This is due, to some extent, to the favorable exchange energy between two electrons with parallel spins located in different orbitals. This exchange interaction, between the unpaired electron on the C_α and the electrons in the σ bond of the $C_\alpha H$ fragment, can influence the sign of the hyperfine coupling between the unpaired electron and the hydrogen nucleus (see Figure 2-3). For example, an unpaired electron with an α spin, located in the p_z orbital on C_α will constrain the electron from C participating in the σ bond to an α spin state and, since electrons participating in a covalent chemical bond must be of opposite spin, this requires that the electron spin on the proton have a β spin (see Figure 2-3). The presence of this negative spin density on the proton will yield a negative hyperfine coupling constant for the hydrogen atom.

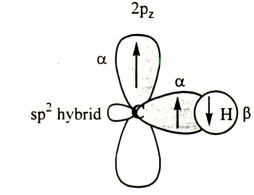

Figure 2-3: The effect of spin polarization on the spin density at the hydrogen atom.

In π radicals, like the chlorophyll cation radicals in PSI, the unpaired electron is delocalized in a π molecular orbital. In symmetric molecules like benzene, this unpaired electron is distributed equally amongst the six carbon atoms that contribute to the π molecular orbital. The proton hyperfine coupling, originating from the interaction of the unpaired spin with the ring protons, in this case, is equivalent for each atom. The magnitude of the hyperfine coupling, therefore, reflects the distribution of the unpaired electron. Moreover, this distribution is a direct probe into the symmetry of the molecule and the molecular orbitals containing the unpaired electron. The McConnell expression[3] describes this relationship

$$A_{iso} = \rho^{\pi} Q$$

where ρ^{π} is the spin density in the p^{π} orbital and Q is an experimentally determined proportionality constant specific to the nucleus of interest.

For orbitals with $\ell \neq 0$ (e.g. p or d orbitals), the hyperfine coupling is anisotropic and arises from a dipolar, through space interaction between the unpaired electron and nearby magnetic nuclei (see Figure 2-4). The classical expression for this interaction is given by

$$E_{dipolar} = \frac{\mu_e \mu_n}{r^3} - \frac{3(\mu_e \bullet \mathbf{r})(\mu_n \bullet \mathbf{r})}{r^5}$$

The corresponding quantum mechanical expression for this interaction is obtained by substituting the appropriate operators. The Hamiltonian is, therefore,

$$\mathcal{H}_{dipolar} = -g_e g_n \beta_e \beta_n \left[\frac{\hat{\mathbf{S}} \bullet \hat{\mathbf{I}}}{r^3} - \frac{3(\hat{\mathbf{S}} \bullet \mathbf{r})(\hat{\mathbf{I}} \bullet \mathbf{r})}{r^5} \right]$$

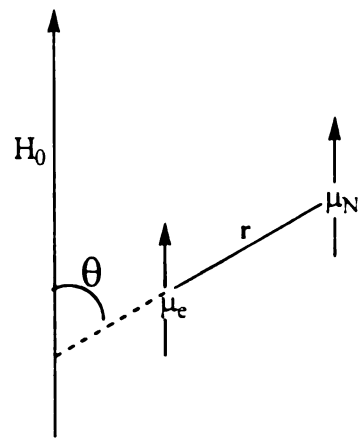

Figure 2-4: The dipolar interaction in an applied magnetic field between the magnetic moments of the electron spin and the nuclear spin for a nuclear spin = 1/2.

To remove the explicit spatial dependence of this Hamiltonian, one must integrate over the electron wavefunction to obtain a Hamiltonian containing only spin operators. This can be accomplished by expanding the Hamiltonian in the Cartesian coordinate system, then integrating. This integration gives

$$\mathcal{H}_{\text{dipolar}} = T_{xx}I_xS_x + T_{yy}I_yS_y + T_{zz}I_zS_z + T_{xy}(I_xS_y + I_yS_x) + T_{yz}(I_yS_z + I_zS_y) + T_{zx}(I_zS_x + I_xS_z)$$

with coefficients

$$T_{\alpha\alpha} = g_e g_n \beta_e \beta_n \left\langle \frac{3\alpha^2 - r^2}{r^5} \right\rangle$$

$$T_{\alpha\beta} = g_e g_n \beta_e \beta_n \left\langle \frac{3\alpha\beta}{r^5} \right\rangle$$

where the brackets indicate integration. A more convenient, and succinct, way to write this Hamiltonian

$$\mathcal{H} = \hat{I} \bullet \underline{\underline{T}} \bullet \hat{S}$$

where $\underline{\underline{T}}$ is a matrix with elements $T_{\alpha\beta}$. This dipolar coupling matrix is traceless and symmetrical and vanishes when averaged over all orientations. It, therefore, does not contribute to the peak positions and splittings observed in solution EPR. Because this matrix is symmetrical, an axis system can always be chosen in which it is diagonal. These diagonal elements are the principal values of the tensor and characterize completely the anisotropy of the hyperfine interaction. For systems with axial symmetry ($x = y \neq z$), the anisotropy can be described by two terms, $A_\perp$ and $A_\parallel$.

The EPR spectrum observed experimentally is a composite of the EPR spectrum for each orientation, with buildups of intensity at the principal values of the A tensor ($A_\perp$ and $A_\parallel$ for a system with axial symmetry). The primary electron donor of PSI studied in Chapters 3 and 4 is a chlorophyll a species, and because this molecule is planar, an axial hyperfine tensor for each of the pyrrole nitrogens is expected. Additionally, because the dipolar coupling term represents a through-space interaction, the magnitude of this coupling, dependent on r^3, can yield distances between the paramagnet and interacting nuclei.

The full hyperfine interaction requires the addition of the isotropic portion of the coupling.

$$A_{total} = A_{iso} + A_{dipolar}$$

The hyperfine Hamiltonian can therefore be represented as

$$\mathcal{H}_{hf} = h\hat{S} \bullet \underline{\underline{A}} \bullet \hat{I}$$

where $\underline{\underline{A}} = A_0 \underline{\underline{1}} + \underline{\underline{T}}$

Here A_0 represents the isotropic portion of the hyperfine coupling and **1** is the unit tensor.

The final term in the spin Hamiltonian, the nuclear quadrupole coupling term does not contribute to the EPR spectrum from P_{700}^{-}, however the effects on the ESEEM spectrum are substantial. These effects, and the functional form of the Hamiltonian, will be explained in the ESEEM section of this chapter.

The presence of multiple, small hyperfine couplings in conjunction with the complexities introduced by the powder pattern lineshapes expected for EPR spectra of frozen solutions lead to an inhomogeneously broadened EPR line. Because of this spectral congestion, the components of the dipolar tensor are obscured. To resolve these small hyperfine couplings in the photosynthetic systems, pulsed and double resonance techniques have been applied. These techniques yield the weak hyperfine couplings desired, but have the advantage of reducing the number of peaks observed in the spectrum as well as decreasing the linewidths associated with the transitions.

Electron Nuclear Double Resonance (ENDOR)

The spin Hamiltonian describing the ENDOR experiment is identical to the one used for EPR (see previous section) and consequently the energy level diagram corresponding to the observed ENDOR transitions is also the same (see Figure 2-2). The ENDOR experiment measures the change in intensity of an EPR absorption as a function simultaneously applied RF radiation. To illustrate the ENDOR effect, an $S = ½$, $I = ½$ system will be utilized. Again, this system mirrors the interaction of the unpaired

electron on P_{700}^{+} with the ^{15}N nucleus on the directly ligating histidine that is discussed in Chapter 3. The Hamiltonian for this interaction is

$$\mathcal{H} = g_e\beta_e HS_z - g_n\beta_n HI_z + A_{iso}S_zI_z$$

with g_n = -0.566378 for the ^{15}N nucleus. A_{iso} = 0.64 MHz for the interaction (see Chapter 3) and ν_n = 1.45 MHz for ^{15}N in a 3200 G static field. The selection rules for EPR are given as $\Delta M_s = \pm 1$, $\Delta M_I = 0$; the allowed transitions for EPR are shown in Figure 2-5. The analogous allowed nuclear transitions representing a nuclear spin flip, with selection rules $\Delta M_I = \pm 1$, $\Delta M_s = 0$, are also indicated. As discussed earlier, these transitions fall in the radiofrequency (RF) range.

The ENDOR experiment is performed by fixing the externally applied Zeeman field so that the resonance condition for a single EPR transition (epr1, for example) is met. The microwave power is increased to equalize the populations of levels 2 and 3. This results in partial saturation of this transition subsequently decreasing the intensity of the EPR absorption. Irradiation with swept RF radiation will effect nuclear transitions when the frequency of the radiation meets the resonance condition for the nuclei (nmr1 or nmr2). Focusing on nmr1, transitions between nuclear levels 1 and 2 will reinstate the population difference between 2 and 3 and therefore desaturate the EPR transition, the absorption due to this transition will therefore increase. This change in the EPR absorption is detected and plotted as a function of the RF frequency.

While the peaks observed in an EPR spectrum reflect the interaction of the unpaired electron with all nearby magnetic nuclei in a multiplicative fashion

$$\text{peaks observed} = \prod_{i=1}^{x} 2n_i I + 1$$

where n is the number of chemically equivalent nuclei and I represents their respective nuclear spins, the ENDOR effect provides the same hyperfine information in an additive

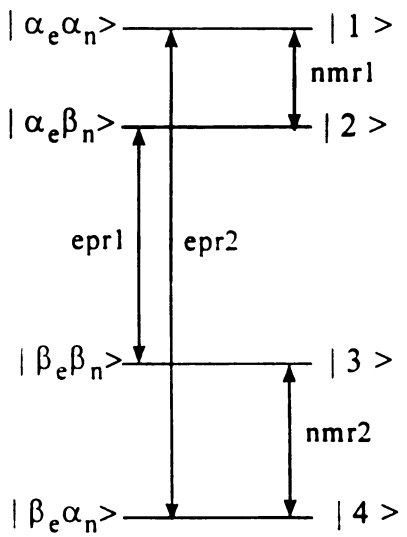

Figure 2-5: Energy level diagram for S = 1/2, I = 1/2 system showing the allowed EPR and NMR transitions.

manner. One pair of peaks appears for each chemically equivalent set of interacting nuclei. This decreases the spectral congestion and moreover, simplifies assignment of the salient features. These peaks, for an isotropic hyperfine coupling, A_{iso}, appear at frequencies

$$\left| \nu_n \pm {}^{A_{iso}}\!/_{2} \right|$$

where ν_n is the free precessional frequency of the nucleus of interest. For the ^{15}N studies reported here, the ENDOR experiments were performed at a static field strength of 3375 G, where the Larmor frequency of ^{15}N is 1.45 MHz.

The presence of hyperfine anisotropy, discussed above in the EPR section. also contributes significantly to the lineshapes observed in frozen solution ENDOR. The lineshape characteristic of an axial hyperfine coupling tensor is shown in Figure 2-6a. ENDOR data are collected in the first derivative mode, the corresponding absorptive powder patterns are shown in Figure 2-6b. The turning points in this ENDOR spectrum represent the most probable orientations and correspond to $A_\perp$ and $A_{||}$. The peaks are split about the Larmor frequency according to

$$A_{dipolar} = g_e g_n \beta_e \beta_n \left(3\cos^2\theta - 1/r^3 \right)$$

where θ=90° for $A_\perp$ and 0° for $A_{||}$. This equation predicts that $A_{||}$ is twice as large as $A_\perp$. The absorptive peaks in Figure 2-6a are then split by an amount equal to $A_{||}$ and the derivative shaped peaks are split by $A_\perp$. In the limit of small dipolar coupling, only a single pair of derivative shaped peaks is observed. By recognizing the lineshapes associated with different tensor symmetries, the geometric and electronic structure of the paramagnetic system can be deduced. The absorptive peaks associated with $A_{||}$ are often difficult to resolve experimentally since the number of orientations with parallel symmetry contributing to the overall lineshape is small. This precludes the use of ENDOR in systems with large dipolar couplings, however the applicability of the technique to systems containing large, isotropic hyperfine couplings has been shown in numerous studies of biological systems.[4] For systems containing small, anisotropic

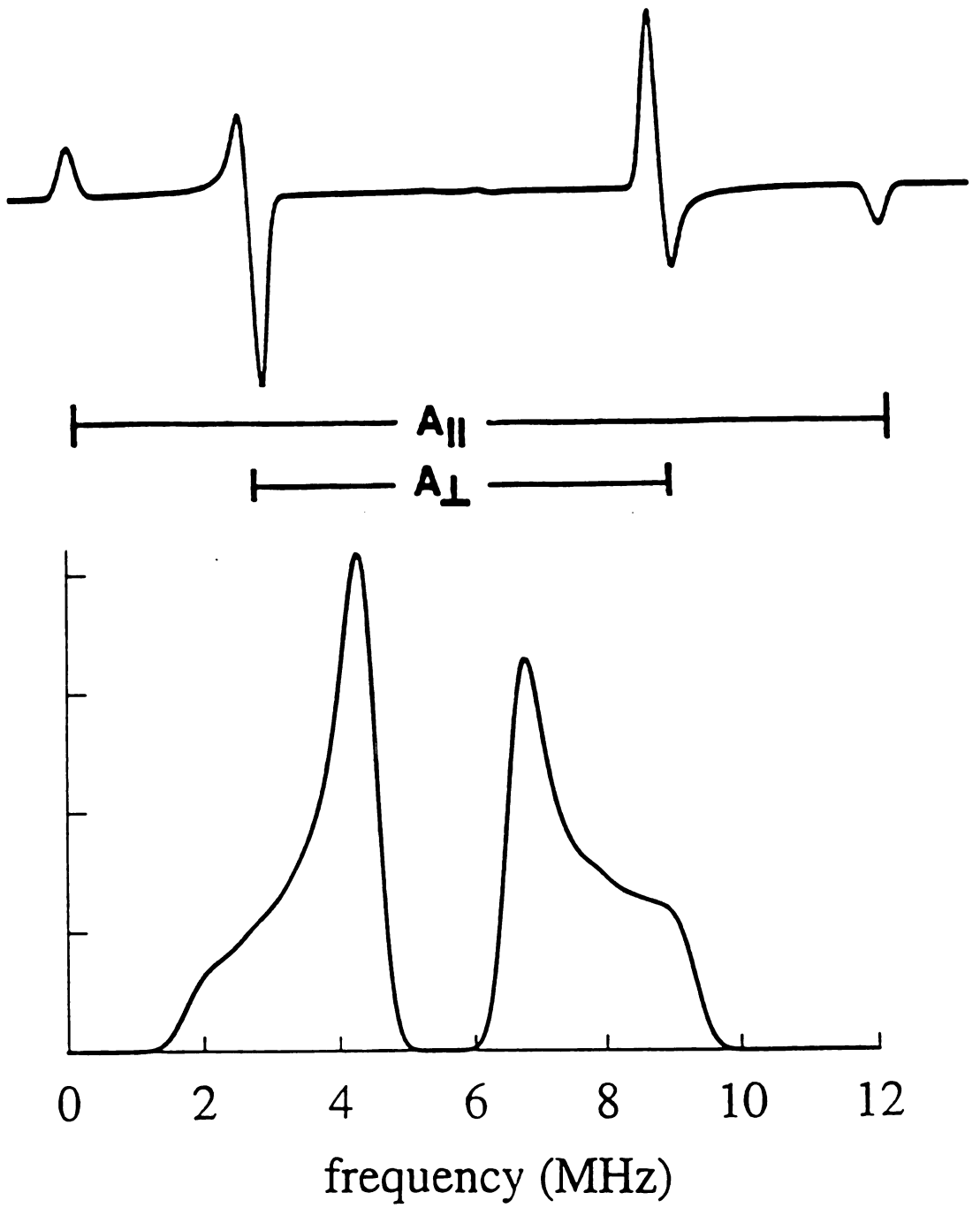

Figure 2-6: ENDOR spectrum showing the first derivative lineshapes expected for an axial dipolar coupling (top) and the corresponding powder pattern absorption (bottom)

hyperfine couplings, the technique of electron spin echo envelope modulation spectroscopy can be applied to extract hyperfine and nuclear quadrupole coupling constants and therefore information regarding the structure and function of the paramagnetic species. The complementarity of these two spectroscopies is exhibited in the study of axial ligation to P_{700}^{+} presented in Chapter 3.

Electron Spin Echo Envelope Modulation (ESEEM)

Electron spin echo envelope modulation (ESEEM) is a sensitive technique for measuring the small superhyperfine couplings in systems with large inhomogeneously broadened EPR lines. Inhomogeneity in an EPR line can result from the presence of anisotropy in the hyperfine term of the Hamiltonian. The electron is subjected to slightly different local fields such that only a small fraction of the spins are in resonance at a given time. The EPR spectrum is then composed of a superposition of these "spin packets" (see Figure 2-7). Inhomogeneous broadening can also be the result of numerous hyperfine couplings, which can be resolved effectively with the use of ENDOR spectroscopy, or fluctuations in the homogeneity of the applied magnetic field, although the latter is only observed at large field values. ESEEM spectroscopy circumvents the inhomogeneity problem by causing rotations of net electron spin magnetization that allow observation of the individual spin packets.

The Two-Pulse ESEEM Experiment

To explain the theory behind a two-pulse ESEEM experiment, a semi-classical model will be utilized. The choice of coordinate systems for this model is crucial, and for the ease of explanation, a rotating coordinate system will be used. Figure 2-8 depicts this

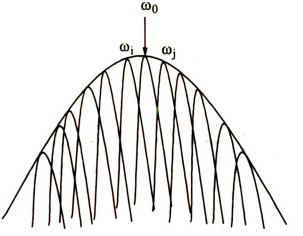

Figure 2-7: An inhomogeneously broadened EPR absorbance.

coordinate system, with rotational frequency ω_0 and with axes X',Y',Z'. As in previous discussions, a static magnetic field with magnitude H_0 is applied along the Z' direction. Detection of the build up and decay of magnetization occurs along Y'.

The description of the two pulse experiment will focus on two spin packets (see Figure 2-7) with characteristic Larmor frequencies that precess slower (ω_i) or faster (ω_j) than the rotating frame. At thermal equilibrium, a net macroscopic magnetization will lie

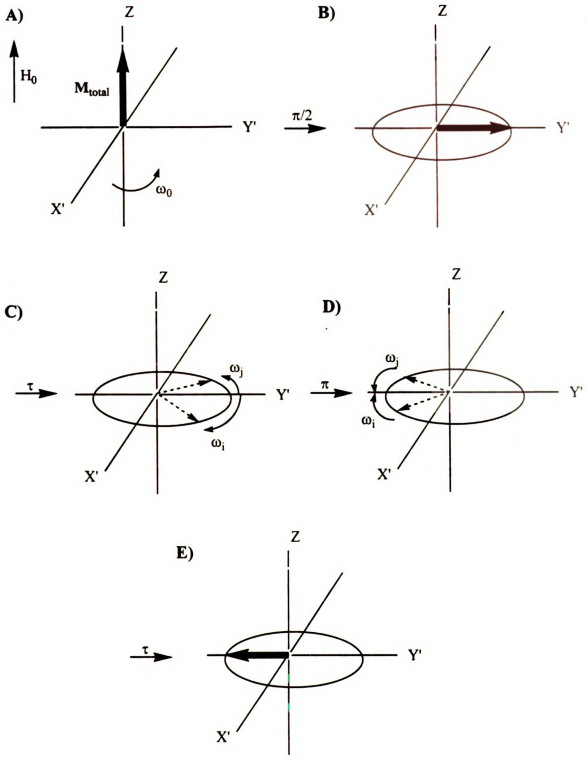

Figure 2-8: Classical description of the formation of a spin echo.

along the z axis. This magnetization, which arises from the population difference of the α and β spin states, is due to the vector sum of the individual magnetic moments.

Application of a short, high field microwave pulse will rotate this magnetization. It can be described quantitatively by the fundamental Bloch equation

$$\frac{d\mathbf{M}}{dt} = \gamma(\mathbf{H} \times \mathbf{M})$$

where **H** is the effective field in the rotating frame. The effective field that is interacting with the magnetization is composed of a z component (H_0) and an x component (H_1). The physical manifestation of this is, as discussed earlier, a precession about H with magnitude

$$H_{effective} = \left[H_1^2 + \left(H_0 \frac{\omega_0 - \omega}{\omega} \right)^2 \right]^{\frac{1}{2}}$$

To determine the magnetization before and after the H_1 field is turned on, the Bloch equations describing the time dependent behavior of the magnetization will need to be solved. For t=0, when the H_1 field is turned on, the solutions are

$$M_z = M_0 \cos\omega_1 t$$
$$\nu = M_0 \sin\omega_1 t$$

where M_0 is the magnitude of the magnetization at thermal equilibrium and ν is the out-of-phase component of the magnetization in the rotating coordinate system; these solutions describe a circle in the Y'Z' plane of the rotating frame, comparable to the oscillatory motion of the magnetic moment as continuous microwave radiation is applied (see EPR section).

Subsequent to the application of a microwave pulse of duration τ_p, the components of magnetization are

$$M_z(\tau_p) = M_0 \cos\omega_1\tau_p$$
$$v(\tau_p) = M_0 \sin\omega_1\tau_p$$

If the microwave pulse is applied with $\omega_1\tau_p = \pi/2$ then

$$M_z(\tau_p) = 0$$
$$v(\tau_p) = -M_0$$

indicating that the magnetization, with its equilibrium value, now lies along the Y` axis.

It is interesting to examine the magnitude of H_1 needed to effect such a rotation. For NMR, $\pi/2$ pulses are regularly applied to the spin system to bring about rotations in an analogous manner. However, because nuclear relaxation occurs on a much slower timescale than the analogous electron relaxation, pulses can be applied for a longer time period to create the H_1 necessary for a $\pi/2$ rotation of the magnetization. With pulses in the microsecond range, H_1 magnitudes on the order of 2-3 G are needed to produce a $\pi/2$ rotation. In pulsed-EPR, pulses of 10-20 ns are necessary to ensure a reasonable frequency spread and allow neglect of the effects of electronic relaxation. This requires the generation of a microwave field with an H_1 in the 25-30 G range, a substantial increase as compared to NMR. Design and implementation of hardware capable of generating nanosecond pulses of this power was one of the primary impediments to the development of pulsed EPR as an effective spectroscopic tool.

Following the first $\pi/2$ pulse, the magnetization lies along the positive Y' axis (see Figure 2-8b). If the frequency of the rotating frame equals the precessional

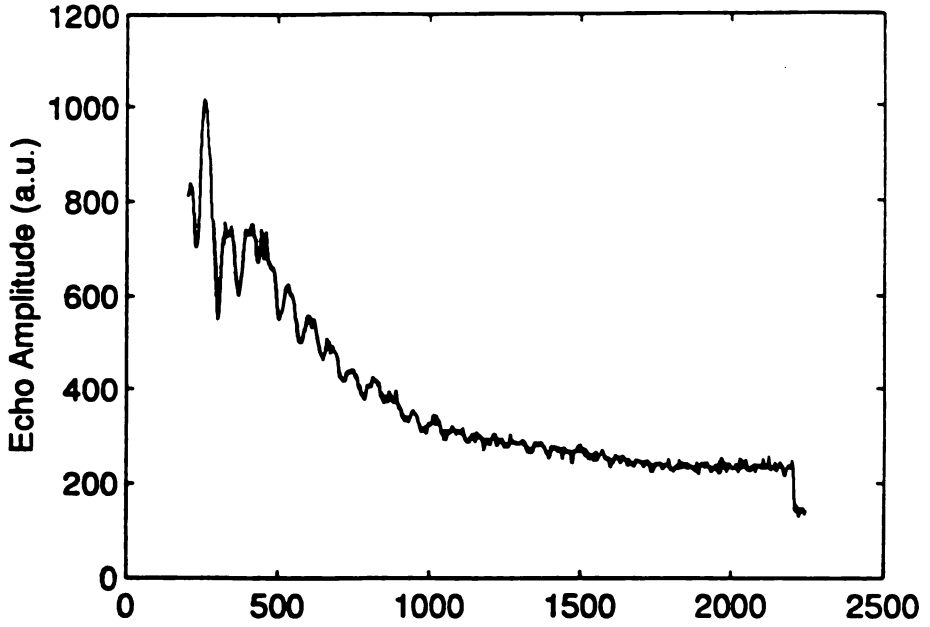

Figure 2-9: Representative time domain trace from two-pulse ESEEM experiment.

frequency of the spin packet, it will remain along the Y' axis during the interpulse time, τ. However, if the spin packets have different offset frequencies (for example, ω_i and ω_j in Figure 2-7), then they will start to dephase immediately (see Figure 2-8c). A second microwave pulse of sufficient duration to rotate the spin packets 180° about the X' axis is then applied. The precessional frequency and direction of these spin packets remains unaltered after the rotation. After time τ, the spin packets refocus along -Y', which creates the build up of magnetization that is known as a spin echo. The amplitude of this spin echo is measured as a function of the interpulse time, τ.

The decay in the echo amplitude as a function of τ is not monotonic (see Figure 2-9), but instead modulated by interactions with nearby magnetic nuclei. The frequency of these modulations can be related directly to the NMR frequencies in Figure 2-5. The modulations of the spin echo decay are the direct result of the fact that microwaves can

induce transitions that initially involve one pair of energy levels, but then branch to a second pair upon application of additional pulse(s). The resulting interference effects then rely on the ability of the microwave pulses to excite coherently all four EPR transitions shown in Figure 2-10. The branching of transitions is allowed quantum mechanically because the anisotropy of the hyperfine interaction effectively mixes the nuclear states contributing to the energy level diagram, consequently the transition probability for each EPR transitions becomes non-zero.

To illustrate this nuclear modulation effect, a semi-classical description will be used (see Figure 2-10). The rotating coordinate system of Figure 2-8 will again be utilized. The energy level system for an S = ½ , I = ½ system is shown in the top of Figure 2-10. The four transitions represent both the allowed and semi-forbidden transitions. Because the states are mixed by the dipolar part of the hyperfine coupling, the $|\alpha>$ and $|\beta>$ labels used in Figure 2-2 are no longer valid, the states, therefore, have been labeled numerically. This discussion will focus on the transition labeled "A" in this energy level diagram. Transition "A" corresponds to a spin packet that is precessing slower than the rotating frame, therefore after the $\pi/2$ pulse, the spin packet has dephased and its precessional frequency is given by $(\omega_0-\omega_1)\tau$ (Figure 2-10a). Application of a π pulse will excite transition "A" , and because of branching, the semi-forbidden transition "C" will be excited as well; these transitions will not, however, be excited with equal probabilities. Spin packet "C" has a characteristic precessional frequency that is faster that the rotating frame, therefore after time τ, spin packet "A" will have refocused along -Y' but spin packet "C" will not be aligned along the rotating frame.

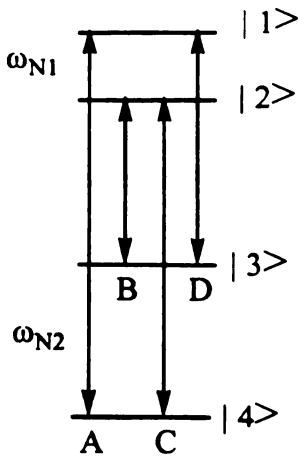

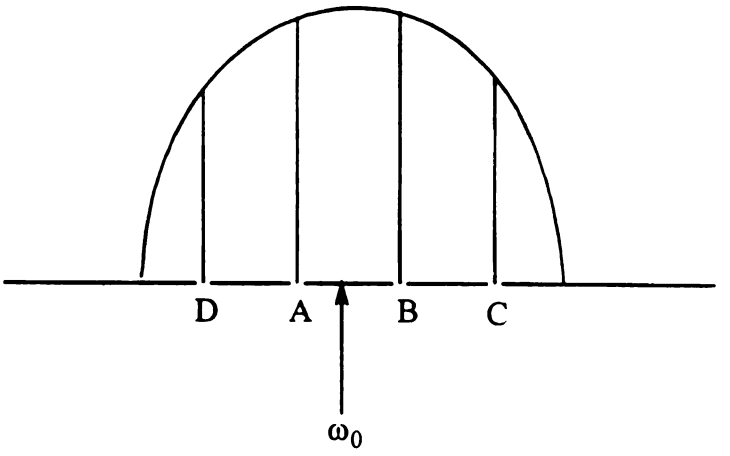

A & B: allowed transitions
C & D: forbidden transitions

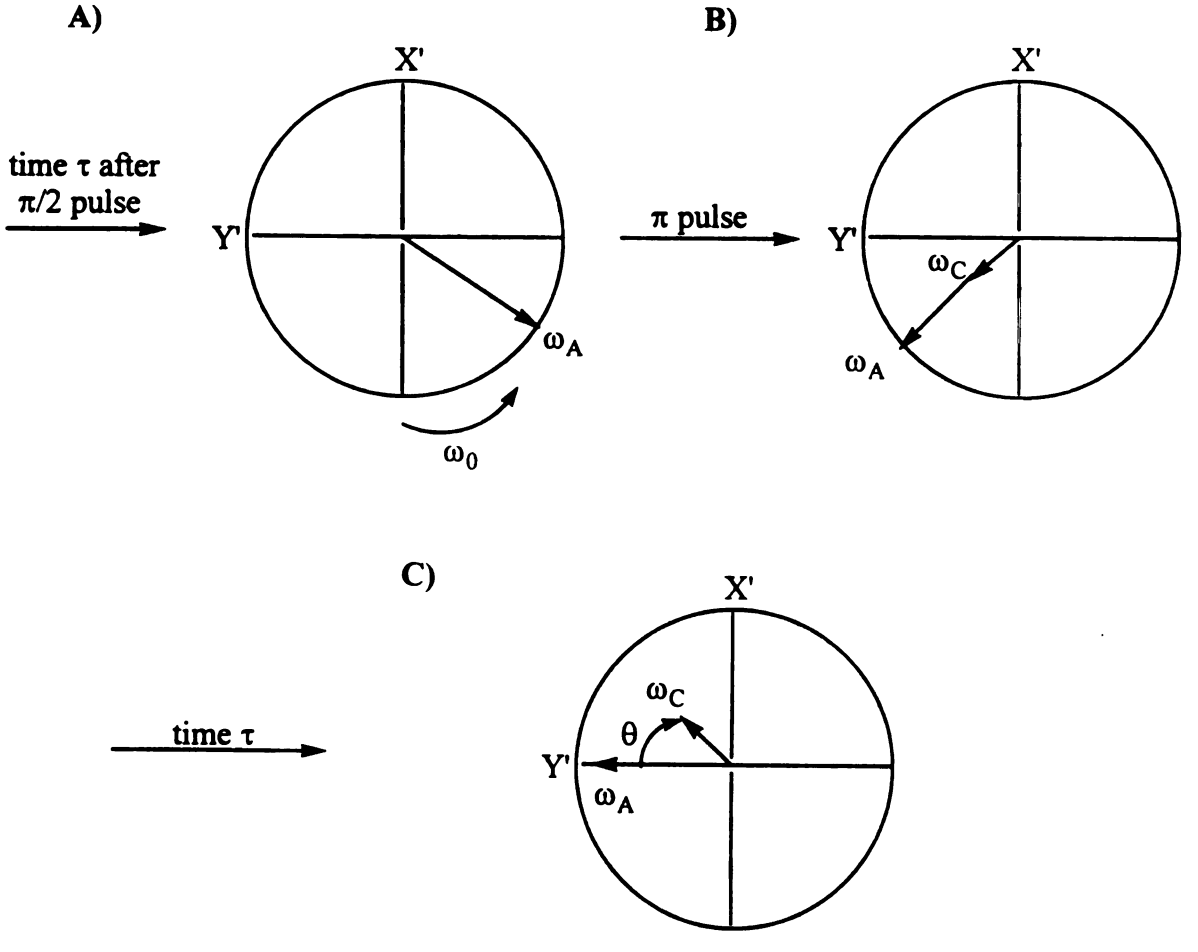

Figure 2-10: Nuclear modulation effect.

The echo amplitude at time τ is given by the projection of these spin packet "vectors" onto -Y'. Spin packet "A" is along the -Y' direction and therefore contributes fully to the echo amplitude, however "C" does not contribute fully and may add to or subtract from the echo amplitude. This depends on the projection of "C", which is given by $\cos(\omega_A - \omega_C)\tau$ or $\cos\omega_{NI}\tau$, where ω_{NI} is the NMR frequency. The echo amplitude observed experimentally is the sum of all of the spin packets in the excited region of the inhomogeneously broadened line and this sum is the source of the modulation pattern observed in the spin echo experiment. The frequencies of the modulations yield the hyperfine frequencies that are the ultimate goal of the spectroscopist. To observe better these frequencies, a cosine Fourier transform of the time domain data is performed and the spectrum obtained subsequent to this yields an ENDOR-like spectrum; hyperfine peaks can be expected to appear centered about the Larmor frequency of the nucleus from which they arise and are split by A_{iso}.

Density Matrix Treatment of ESEEM

Because the generation of spin echoes and the nuclear modulation effect are both quantum mechanical phenomena, they can be understood quantitatively by solving the total spin Hamiltonian describing the interaction of the spin system with the static and applied magnetic fields. This is most easily accomplished by utilizing the density matrix formalism.

The density operator, ρ, describes the projection of one basis set onto another and the elements of the density matrix characterize the quantum state of the spin system. It is possible, therefore, to calculate all of the physical observables of $|\Psi(t)>$ from the density matrix. The pertinent operator is given by

$$\rho(t) = |\Psi(t)\rangle\langle\Psi(t)|$$

with matrix elements

$$\rho_{pn}(t) = \langle u_p | \rho(t) | u_n \rangle$$

where Ψ is a state vector at time t that can be described in terms of an orthonormal basis set $|u_n>$ with coefficients $c_n(t)$ such that

$$|\Psi(t)\rangle = \sum_n c_n(t) | u_n \rangle .$$

The expectation value $<A>(t)$ of an observable A can then be obtained by using

$$\langle A \rangle(t) = \mathrm{Tr}\{\rho(t) A\} .$$

The equation of motion for the density operator can be derived by using the Schroedinger equation

$$\frac{d}{dt}\rho(t) = \frac{1}{i\hbar}[\mathcal{H}(t), \rho(t)]$$

where $\mathcal{H}(t)$ is the time dependent system Hamiltonian.

Integration of this equation will yield the density matrix ρ_E at the time of the appearance of the echo in terms of the initial density ρ_0. The system Hamiltonian in this equation of motion consists of a sum of two components

$$\mathcal{H} = \mathcal{H}_0 + \mathcal{H}_1$$

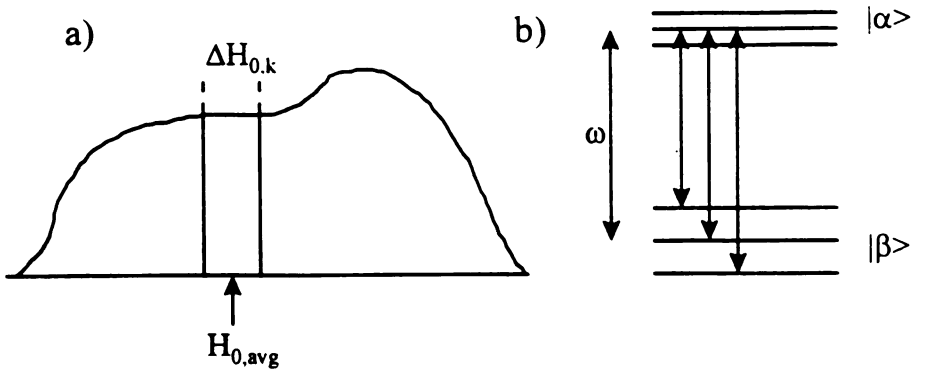

Figure 2-11: a) Inhomogeneously broadened line indicating the distribution of values of H_0. b) Energy levels of a quantized spin system. Microwave radiation of frequency ω is able to induce transitions from any α state to more than one β state.

where $\mathcal{H}_0$ is the Hamiltonian for precessional periods and $\mathcal{H}_1$ the Hamiltonian for nutation. The echo signal is proportional, then, to $Tr(\rho \mathcal{H}_1)$. To obtain this trace, two summations must be performed: the first over the $|\alpha_i>$ and $|\beta_j>$ states of each quantized, this will yield the envelope modulation function; and the second over the systems that make up the inhomogeneously broadened line, this will produce the functional form of the spin echo signal. The first of these summations can be factored out provided that the pulse width is sufficient to excite all spin packets within $\pm\Delta\mathcal{H}_{0,k}$ of an average value, $\mathcal{H}_{avg}$ (see Figure 2-11), the second, provided that $\Delta\mathcal{H}_{0,k}$ is large with respect to the energy spacing in each spin manifold.

The general expression for the echo can be given as

$$E = \eta Tr(\rho_E \mathcal{H}_1)$$

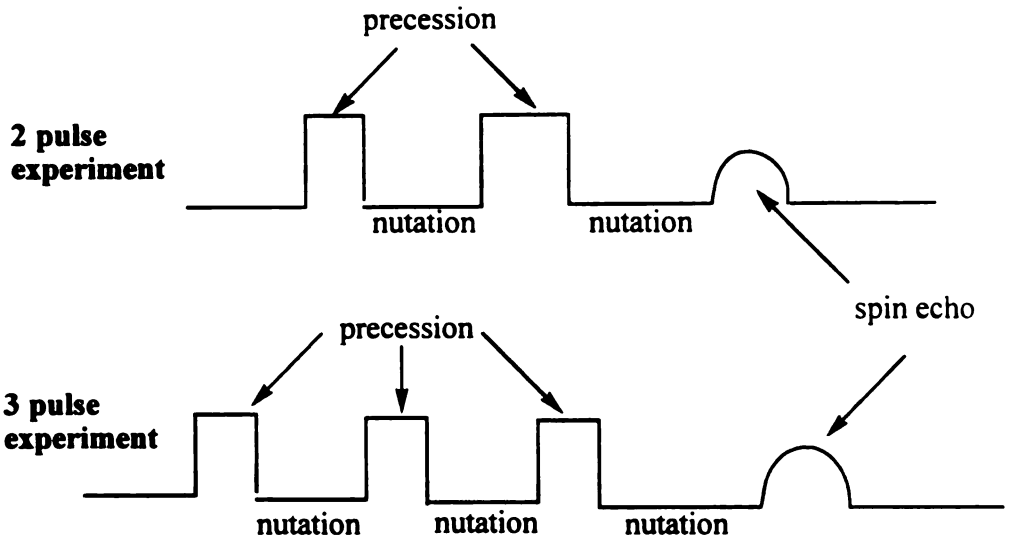

Figure 2-12: Pulse sequences for the Hahn (top) and stimulated (bottom) echo experiments indicating periods of nutation and precession.

where ρ_E is the density matrix of the system when the maximum echo appears and $\mathcal{H}_1$ is the Hamiltonian describing the interaction of the spin system with the microwave pulse and is given by

$$\mathcal{H}_1 = \omega S_x$$

Calculation of the initial and final density matrices is essential in the derivation of the functional form of the echo expression for the two or three pulse experiment. These expressions, as given by Mims (1972)[5] are

$$E(\tau) = \left[2(2I+1)\right]^{-1} \mathrm{Tr}\left[Q_\tau^+ M^+ P_\tau^+ M Q_\tau M^+ P_\tau M + \text{Hermitian conjugate}\right]$$

$$E(\tau+T) = \left[4(2I+1)\right]^{-1} \mathrm{Tr}\begin{bmatrix} Q_\tau^+ M^+ P_T^+ P_\tau^+ M Q_\tau M^+ P_T P_\tau M \\ + Q_T^+ Q_\tau^+ M^+ P_\tau^+ M Q_T Q_\tau M^+ P_\tau M + \text{H.C} \end{bmatrix}$$

The derivation of the echo expressions for the two and three pulse experiments is long and, for the sake of brevity, only the summary of this derivation will be included here. The details of the derivation can be found in the classic 1972 paper by W.B. Mims.[5]

Initially, the Hamiltonians corresponding to precession and nutation (see Figure 2-12) need to be transformed into the rotating frame. Then, the solutions for the equation of motion for the transformed density matrix ρ_E containing a time dependent Hamiltonian need to be obtained. This can be accomplished by using general rotation operators of the form

$$\rho(t) = \exp[-i\mathcal{H}t/\hbar]\,\rho(0)\,\exp[i\mathcal{H}t/\hbar]$$

The density matrix following the pulse sequence can be written as

$$\rho_E(t) = R^{-1}\rho(0)\;R \quad \text{where} \quad R = \prod_{n,p} R^{(n,p)}(t_p,\tau,T) \quad \text{and}$$

$$R^{(n,p)}(t_p,\tau,T) = \exp\left[(2\pi i/h)\mathcal{H}_{n,p}(t_p,\tau,T)\right]$$

Here $\mathcal{H}_{n,p}$ represents the various parts of the Hamiltonian in nutation and free precessional periods and t_p is the pulse duration. An appropriate basis set must be chosen such that $\mathcal{H}_p$ is block diagonal with $\mathcal{H}_1$ connecting elements amongst blocks but not within them. The resulting basis set is built up by using the two electron spin manifolds (α and β) and completed by including the nuclear spin eigenfunctions of $\mathcal{H}_p$. This formalism allows the $\mathcal{H}_1$, ρ_E and $R^{n,p}(t_p,\tau,T)$ matrices to be partitioned in submatrix form

	α states	βstates
α states	$A^{\alpha\alpha}$	$A^{\alpha\beta}$
β states	$A^{\beta\alpha}$	$A^{\beta\beta}$

Once this matrix has been set up and normalized, one finds that only $A^{\alpha\alpha}$ and $A^{\beta\beta}$ of $R_p(\tau,T)$ and the off diagonal block of $\mathcal{H}_1^{\alpha,\beta}$ contribute to the echo signals; these matrices are designated P,Q and M, respectively. The submatrices corresponding to P and Q are diagonal with elements

$$P_{ii} = \exp\left(i\omega_i^{\alpha} t\right) \quad \text{and} \quad Q_{nn} = \exp\left(i\omega_n^{\beta} t\right)$$

where t represents either τ or T depending on the experiment and ω_i is the energy of the ith state belonging to the α or β manifold. The M submatrix is not diagonal and maps the nuclear eigenvectors from one spin manifold to the other, it is given by

$$\mathcal{H}_1 = \frac{h\omega_1}{4\pi} \begin{vmatrix} 0 & M \\ M^{+} & 0 \end{vmatrix}$$

where $M = M_{\alpha}^{+} M_{\beta}$. These unitary matrices describe the state mixing in the α and β manifolds with elements given by

$$M_{i,n} = \alpha\langle i|n\rangle\beta .$$

To obtain the terms involving the superhyperfine frequencies, the expressions for the two and three pulse echoes need to be expanded by using the above definitions and terms in the trace can then be rearranged to yield a frequency independent term and

$$\omega_{ij}^{\alpha} = \omega_i^{\alpha} - \omega_j^{\alpha}$$
$$\omega_{kn}^{\beta} = \omega_k^{\beta} - \omega_n^{\beta}$$

The ultimate expressions for the envelope modulation functions can be written in the following forms

$$E_{mod}(\tau) = |v|^4 + |u|^4 + |v|^2|u|^2\left[2\cos\omega_{ab}\tau + 2\cos\omega_{cd}\tau - \cos\left(\omega_{ab} - \omega_{cd}\right)\tau - \cos\left(\omega_{ab} + \omega_{cd}\right)\tau\right]$$

$$E_{mod}(\tau,T) = |v|^4 + |u|^4 + |v|^2|u|^2 \left[\begin{array}{l} \cos\omega_{ab}\tau + \cos\omega_{cd}\tau + 2\sin^2\frac{1}{2}\omega_{cd}\tau \ \cos\omega_{ab}(\tau+T) \\ + 2\sin^2\frac{1}{2}\omega_{ab}\tau \ \cos\omega_{cd}(\tau+T) \end{array} \right]$$

where the frequencies given by ω_{ab} and ω_{cd} indicate the intervals between states |a>, |b>, |c> and |d> (see Figure 2-13). The u and v terms are the transition probabilities for the branching transitions and are the elements of the M matrices discussed above. It is easy to see how the lack of branching (either u or v equal to 0) will result in no observed modulations. These expressions also show the sum and difference frequencies that are observed in the two-pulse experiment.

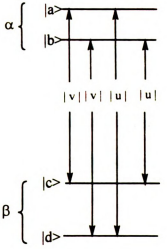

Figure 2-13: Energy level diagram for S=1/2, I=1/2 system. The vectors indicate the transition matrix elements connecting the eigenstates.

The transition probabilities for the branching transitions can be determined by using transformations that can be described as rotations of the electron and nuclear coordinate systems. The following Hamiltonians are obtained.

$$\mathcal{H}_\alpha = \omega_I I_z + \frac{1}{2} A I_z + \frac{1}{2} B I_x$$

$$\mathcal{H}_\beta = \omega_I I_z - \frac{1}{2} A I_z - \frac{1}{2} B I_x$$

Diagonalization of these Hamiltonians will yield eigenfrequencies given by

$$\omega_\alpha = \omega_{ab} = \left[\left(\frac{1}{2} A + \omega_I \right)^2 + \left(\frac{1}{2} B^2 \right)^2 \right]^{\frac{1}{2}}$$

$$\omega_\beta = \omega_{cd} = \left[\left(\frac{1}{2} A - \omega_I \right)^2 + \left(\frac{1}{2} B^2 \right)^2 \right]^{\frac{1}{2}}$$

these are the hyperfine frequencies where A and B represent the first and second order terms of the hyperfine tensor (*vide infra*) and ω_I is the nuclear Larmor frequency.

Because the rotation operators utilized to diagonalize the above Hamiltonians correspond to the M_α and M_β, the terms of the M matrix (the u and v components) can easily be determined. The product $|v|^2|u|^2$ is then

$$4|v|^2|u|^2 = \left(\omega_I B / \omega_\alpha \omega_\beta \right)^2$$

and this can be used to give the final form of the envelope modulation functions

$$E_{mod}(\tau) = 1 - \frac{2\omega_I^2 B^2}{\omega_{ab}^2 \omega_{cd}^2} \sin^2 \frac{1}{2}\omega_{ab}\tau \sin^2 \frac{1}{2}\omega_{cd}\tau$$

$$E_{mod}(\tau + T) = 1 - \frac{2\omega_I^2 B^2}{\omega_{ab}^2 \omega_{cd}^2} \left\{ \begin{array}{l} \sin^2 \frac{1}{2}\omega_{ab}\tau\left[1 - \cos\omega_{cd}(\tau + T)\right] \\ + \sin^2 \frac{1}{2}\omega_{cd}\tau\left[1 - \cos\omega_{ab}(\tau + T)\right] \end{array} \right\}$$

In these expressions the term $(\omega_I B/\omega_{ab}\omega_{cd})^2$ is called the modulation depth parameter and it is clear from examination that if the nuclear Zeeman interaction, ω_I, is equal to the hyperfine frequency then the maximum modulation depth occurs. Furthermore, if the assumption that the hyperfine coupling arises from a contact interaction, A_{iso}, and a classical magnetic dipole-dipole interaction, then the A and B parameters can be given as

$$A = A_{iso} + \frac{g g_n \beta \beta_n}{\hbar r^3}\left(3\cos^2\theta - 1\right)$$

$$B = \frac{g g_n \beta \beta_n}{\hbar r^3}(3\cos\theta \sin\theta)$$

These assumptions have been made throughout the analysis of the ESEEM data presented in Chapters 3-5.

Nuclear Quadrupole Effects

For nuclei with $I \geq 1$ interacting with the paramagnetic species, the ESEEM experiment is substantially affected by the magnitude of the nuclear quadrupole interaction.[6] This interaction is present when the electric quadrupole moment of the nucleus is surrounded by a non-spherical electron distribution. The quadrupolar nucleus will interact with the electric field gradient from the non-symmetrical electron cloud

depending on the orientation of the charge distribution within the nucleus (see Figure 2-14). Because the quadrupole moment is intimately tied to the nuclear spin through the nuclear structure, the quadrupole interaction connects the spin directly to the molecular network. The nuclear spin is, through its magnetic moment, also connected to the magnetic fields produced by the spectrometer and unpaired electrons. Thus, the quadrupolar interaction that is detected and measured by using ESEEM spectroscopy can yield, when combined with the information extracted from the hyperfine coupling, structural information regarding the paramagnetic species. The utility of measuring both

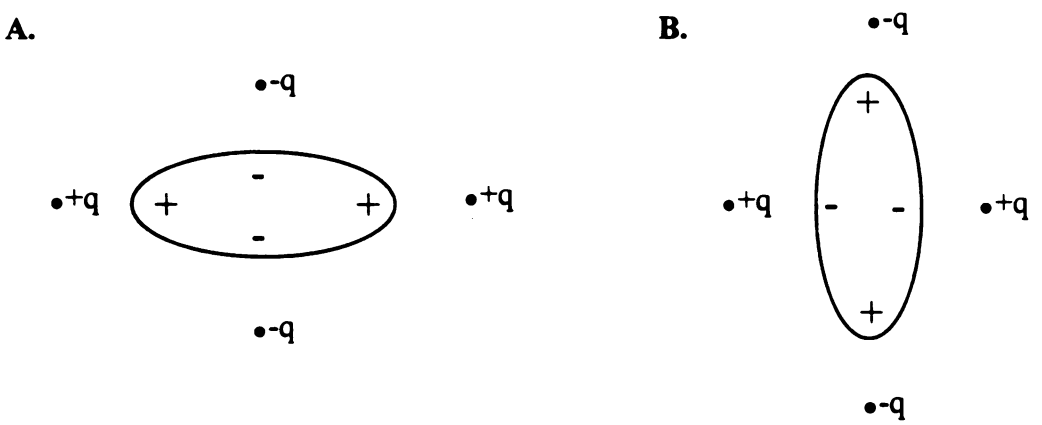

Figure 2-14: The interaction of a quadrupolar nucleus with four point charges showing the lowest energy state for the nucleus (nucleus B).

of these parameters is exhibited by the chlorophyll cation radical, P_{700}^{+} , studied in Chapter 4. By using multifrequency ESEEM and numerical simulations of experimental data, the quadrupole coupling constants and asymmetry parameters were determined for

the pyrrole nitrogens in P_{700}^{+}. These results, and their implications for structure/function relationships in PSI will be discussed in Chapter 4.

Quantitation of this quadrupolar interaction is through the quadrupole coupling tensor, which is the product of the nuclear quadrupole moment and the gradient of the electric field due to the surrounding electrons. This tensor is traceless and disappears in the limit of a symmetrical distribution, e.g. cubic or octahedral, where the electric field gradient is zero. However, a concentration of charge, for example from the electrons participating in a covalent bond between a transition metal atom and a ligand, will result in a non-zero gradient and the subsequent quadrupolar coupling is a measure of the electron concentration in the bond. To understand the effects of this quadrupole coupling on the energy levels, the Hamiltonian describing this interaction will be examined. Because the quadrupole moment's axis of quantization is collinear with the nuclear spin angular momentum, the Hamiltonian for the quadrupole interaction is expressed in terms of the operators for the nuclear spin. This operator is

$$\mathcal{H}_{nqi} = \kappa\left[3I_z^2 - I^2 + \eta\left(I_x^2 - I_y^2\right)\right]$$

where κ is the quadrupole coupling constant and reflects the extent to which the nucleus is coupled to the electric field gradient and is given by

$$\kappa = \frac{e^2qQ}{4h}$$

while η is the asymmetry parameter and measures the deviation from axial symmetry. It is given by

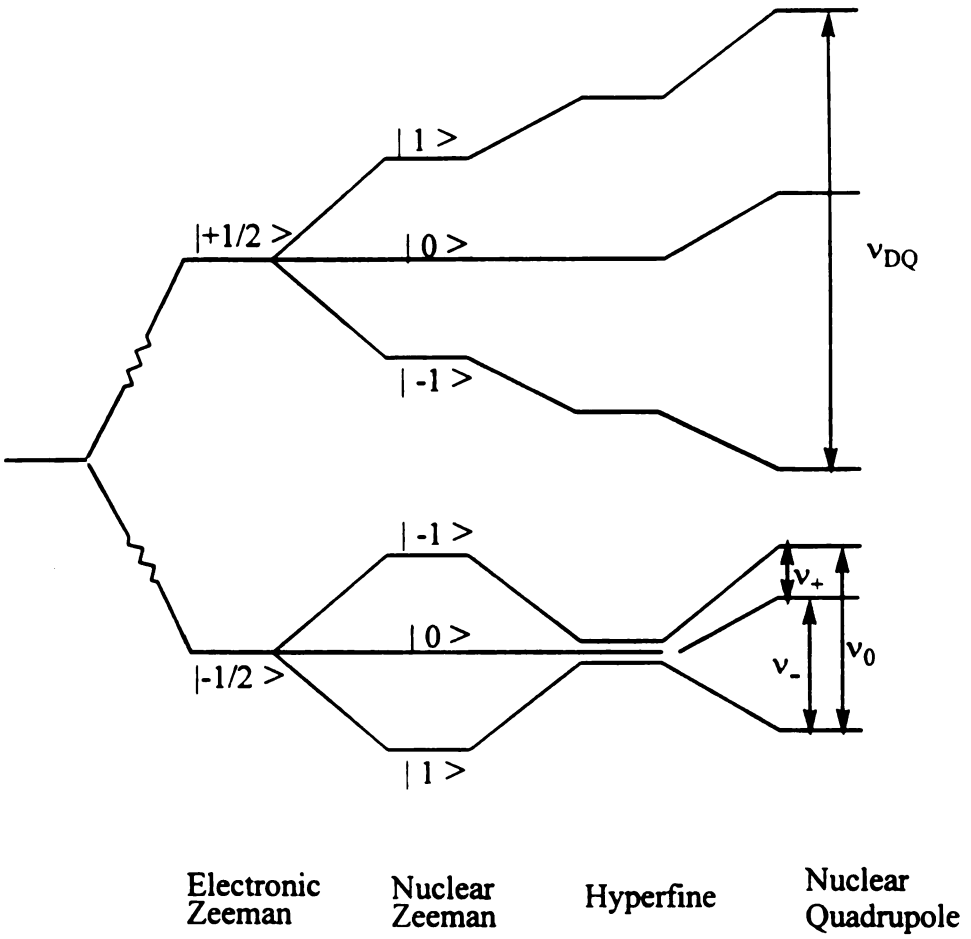

Figure 2-15: Energy level diagram for an S=1/2, I=1 system at exact cancellation.

$$\eta = \left| \frac{q_{xx} - q_{yy}}{q_{zz}} \right|$$

where q_{xx}, q_{yy} and q_{zz} are the principle values of the field gradient.

The effect of this Hamiltonian on the spin system will be investigated for the special case where the electron nuclear hyperfine interaction is exactly twice the nuclear Larmor frequency and nearly isotropic. This "exact cancellation" condition results in a collapse of the energy levels in one spin manifold (see Figure 2-15).[7] Complete cancellation is only possible if the magnitude of the dipolar portion of the hyperfine coupling is small compared to the isotropic contribution.[8] The transitions in the "cancellation" manifold arise from pure quadrupolar interactions and are easily resolved with stimulated echo ESEEM spectroscopy. The peaks that arise from these "zero-field" transitions appear at frequencies that correspond to pure quadrupolar interactions. The energies of these transitions can be obtained by diagonalizing the 3 x 3 Hamiltonian matrix. These frequencies are given by

$$\nu_+ = (3+\eta)\kappa$$
$$\nu_- = (3-\eta)\kappa$$
$$\nu_0 = 2\eta\kappa$$

where the transitions ν_+,ν_- and ν_0 are shown in Figure 2-15.

In the other, non-cancellation, spin manifold, the effect of the hyperfine and nuclear Zeeman fields must be taken into account. The external magnetic field due to these interactions, with angles θ and φ with respect to the quadrupolar axis system must be incorporated into the Hamiltonian. An isotropic hyperfine coupling with

$$\nu_{eff} = \left|\nu_i \pm A/2\right|$$

is assumed. The Hamiltonian matrix[9] corresponding to the non-cancellation manifold. then, has the form

$$\mathcal{H} = \begin{vmatrix} \kappa(1+\eta) & \nu_{eff}\sin\theta\cos\varphi & \nu_{eff}\cos\theta \\ \nu_{eff}\sin\theta\cos\varphi & -2\kappa & -i\nu_{eff}\sin\theta\sin\varphi \\ \nu_{eff}\cos\theta & -i\nu_{eff}\sin\theta\sin\varphi & \kappa(1-\eta) \end{vmatrix}$$

Trigonometric as well as graphical solutions to this Hamiltonian are available.[10]

Experimentally, the exact cancellation condition (for ^{14}N) is manifested by the appearance of three sharp, low frequency peaks plus a broader "double quantum" peak at higher frequency, which arises from transitions ($\Delta M_I = -1$ to $\Delta M_I = +1$) originating from the non-cancellation manifold.[11] The appearance of this peak is indicative of the contribution of the dipolar coupling to the total hyperfine coupling in the system. The anisotropic hyperfine interaction acts to mix the eigenstates this alters the transition probabilities between the eigenstates in the non-cancellation manifold. The probability of the double quantum transition occurring is, therefore, decreased with a concomitant loss of amplitude in the ESEEM spectrum. The anisotropic contribution can be estimated based on the appearance of this peak and this information can be utilized to simulate numerically the experimentally observed data. This methodology has been used to determine the magnetic properties of the chlorophyll cation radical involved in the primary electron transfer events in PSI (see Chapter 3-4).

LIST OF REFERENCES

LIST OF REFERENCES

[1] A) Mims, W.B. & Peisach, J (1981). in *Biological Magnetic Resonance* (Berliner, L.J. & Reuben, J., eds.) pp. 213-263, Plenum Press, New York. B) Kevan, L. (1990) in *Modern Pulsed and Continuous Wave Electron Spin Resonance* (Kevan, L. & Bowman, M.R., eds.) Wiley-Interscience. C) McCracken, J. In *Handbook of Electron Spin Resonance*, Vol. II, (Poole, C.P., ed.) in press.

[2] A) Atherton, N.M. (1993) *Principles of Electron Spin Resonance*, Ellis-Horwood/PTR Prentice Hall, New York. B) Wertz, J.E. & Bolton, J.R. (1986) *Electron Spin Resonance: Elementary Theory and Practical Applications*, Chapman & Hall, New York. C) Gordy, W. (1980) *Theory and Applications of Electron Spin Resonance in Techniques of Chemistry*, Vol. XV (West, W., ed.) John Wiley & Sons, New York. D) Kevan, L. & Kispert, L.D. (1976) *Electron Spin Double Resonance Spectroscopy*, John Wiley & Sons, New York. E) Keijzers, C.D.; Reijerse, E.J. & Schmidt, J. (1989) *Pulsed EPR. A New Field of Applications*, North Holland Publ.

[3] McConnell, H.M.; Heller, C.; Cole, T. & Fessenden, R.W. (1959) *J. Chem. Phys. 82*, 766.

[4] Mac, M.; Tang, X.-S.; Diner, B.A.; McCracken, J. & Babcock, G.T. (1996) *Biochemistry 35*, 13288.

[5] A) Mims, W.B. (1972) *Phys. Rev. B. 5(7)*, 2409.

[6] Lucken, E.A.C. (1969) *Nuclear Quadrupole Coupling Constants*, Academic Press, NY

[7] Mims, W.B. & Peisach, J. (1978) *J. Chem. Phys. 69*, 4921.

[8] Flanagan, H.L. & Singel, D.J. (1987) *J. Chem. Phys. 87*, 5606.

[9] A) Casabella, P.A. & Bray, P.J. (1958) *J. Chem. Phys, 28*, 1182. B) Muha, G.M. (1980) *J. Chem. Phys, 73*, 4139.

[10] Astashkin, A.V.; Dikanov, S.A. & Tsvetkov, Yu. D. (1984) *J. Struct. Chem. 25*, 45.

[11] Gerfen, G.J. & Singel, D.J. (1994) *J. Chem. Phys. 100*, 4127.

Chapter 3

Identification of Histidine as an Axial Ligand to P_{700}^{+}

Background

Long range electron transfer and the chemiosmotic hypothesis developed in the 1960's by Peter Mitchell[1] and others [2,3] proposed that the key electron transfer reactions of respiration and photosynthesis were directed across the 35 Å span of the membrane dielectric. Although these ideas have gained support and general acceptance over the past 25 years, many of the factors governing long range electron transfer reactions have remained unclear. The simple, non-adiabatic description of electron transfer given so eloquently by Fermi's golden rule indicates that the nuclear positions and environments of reacting molecules play a central role in determining the electron transfer rate:

$$k_{et} = \frac{2\pi}{h} V^2_R \, FC$$

where V^2_R is the electronic coupling of the reactant and product wavefunctions and FC is the Franck-Condon factor representing the integrated overlap of the reactant and product nuclear wavefunctions. The classical view of nuclear motion described by Marcus[4] and the analogous quantum mechanical explanations of Levich and Dogonadze[5] and of Jortner[6] treat the nuclear reactant and product wavefunctions as harmonic oscillator potential surfaces with the subsequent overlap of these wavefunctions representing the Franck-Condon factors. This overlap will be maximal when the Gibbs free energy ($-\Delta G^{\circ}$) is equal to the reorganization energy (λ), the energy required to change the equilibrium

geometry of the reactant state to the product state without concomitant electron transfer. The overall gaussian dependence of the electron transfer rate on this free energy predicted by Marcus has been confirmed experimentally; the rate rises with increasing $-\Delta G^{\circ}$ until $-\Delta G^{\circ}$ is equal to λ then falls as $-\Delta G^{\circ}$ exceeds the reorganization energy. From a classical viewpoint, the width of this gaussian, is proportional to the Boltzmann thermal energy. However, if the effective frequency of the oscillator is large with respect to the thermal energy, then a quantum mechanical approach is necessary. With the quantum mechanically corrected view of the harmonic oscillator, nuclear tunneling becomes an added concern and the breadth of the gaussian approximating the rate/Gibbs free energy relationship becomes markedly temperature independent and proportional to $\sqrt{\lambda}h\omega$.[7]

The application of these theories to the photosynthetic systems of bacteria has provided a wealth of kinetic, thermodynamic and structural information on intermolecular electron transfer.[8] These results indicate that the electron transfer rates in these systems are modulated by the interdependence of $-\Delta G^{\circ}$ and λ, which are, in turn, dependent upon the geometric and electronic structures of the cofactors involved in the electron transfer reactions. The availability of a high resolution X-ray crystal structure of the reaction centers from purple non-sulfur bacteria has been a tremendous catalyst to the study of these electron transfer rates, providing an *in vivo* geometric structure of the cofactors.[9,10] Similar studies of oxygenic photosynthetic systems have been hindered by the lack of an analogous high resolution structure. Because the bacterial systems lack the oxidative power necessary for oxygen evolution, a comparative study of the two systems, which

contain many structural and mechanistic similarities, is desirable from an evolutionary perspective.

In PSI, the primary charge separation event proceeds via the light-induced generation of a chlorophyll a cation radical species (P_{700}^{+}).[11] This photochemically active chlorophyll is distinguished from the light harvesting and energy transfer chlorophylls by its spectral and redox properties. Initial charge separation occurs with a quantum yield near unity, even though recombination back to the ground state is favored thermodynamically. In spite of the fact that hypotheses rationalizing this unidirectional electron transfer have been advanced,[12] no definitive explanation has been found. Elucidation of the geometric and electronic structures of the primary electron transfer cofactors, specifically P_{700}, is necessary to understand the directional specificity and efficiency of forward electron transfer in PSI. Although significant progress has been made in solving the crystal structure of PSI,[13] the resolution is not yet sufficient to provide a clear view of the geometric structure of P_{700}; neither the nuclearity nor the ligation spheres of the chromophore has been determined definitively. Because the ligation and hydrogen bonding environments of chlorophyll species *in vivo* can affect profoundly the chemical and optical properties of the cofactor, and therefore, the forward electron transfer rate, work exploring the ligation sphere of P_{700}^{+} was undertaken and is presented in this chapter. An analogous investigation of the electronic structure of the cation radical utilizing isotope enrichment, ENDOR, multifrequency ESEEM and numerical simulations of experimental data will be presented in Chapter 4.

Chlorophyll

The ability of a chlorophyll species *in vivo* to perform a variety of functions, from light harvesting and energy transfer to primary electron donor and acceptor roles, reflects the flexibility of the species and the sensitivity of its molecular orbitals (MO's) to modulation by the local protein environment. Characteristic optical, electronic and magnetic properties of chlorophyll species *in vivo*, which are photosystem specific, emanate from the relative energies and electron configurations of the valence MO's of the neutral or ionic species.[14],[15] These general features can be understood best by examining the electronic structure of a porphyrin containing perturbed valence MO's.

Porphyrins contain four fully unsaturated cyclic tetrapyrroles and have D_{4h} symmetry (see Fig. 3-1A). Saturation of ring IV results in the formation of a chlorin (Fig. 3-1B), additional saturation of ring II creates a bacteriochlorin (Fig. 3-1C). The progressive saturation of the C_β-C_β bonds changes the energies, symmetries and electron distributions of the porphyrin MO's, which destabilizes the valence orbitals and alters the shape and symmetry of the cyclic π system.[14] The effect of these distortions on the chemical properties of the chlorin or bacteriochlorin can be observed by examining the orbitals comprising the highest occupied and lowest unoccupied π molecular orbitals (HOMO, HOMO-1, LUMO and LUMO+1) for the porphyrin derivatives relative to the unperturbed porphyrin, see Figure 3-2; symmetry labels for the Zn porphyrin, chlorin and bacteriochlorin in this figure are from the D_{4h} point group and have been utilized for

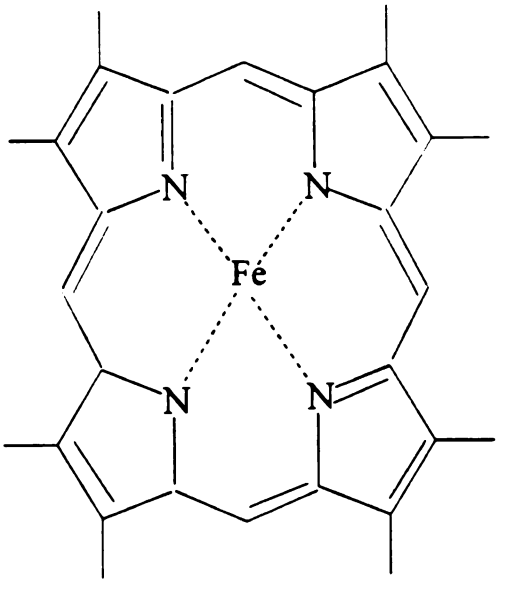

A. Porphyrin

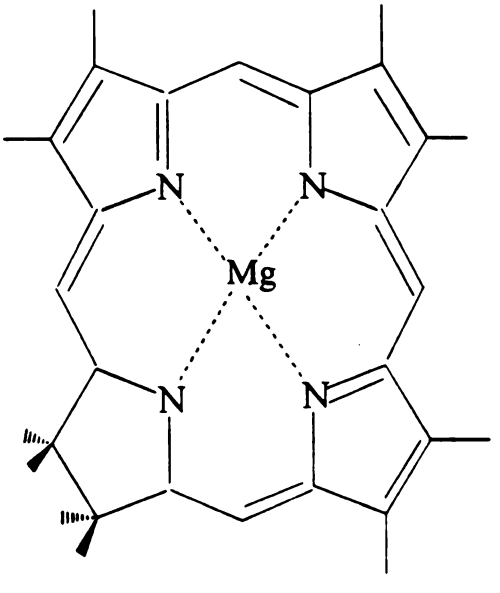

B. Chlorin

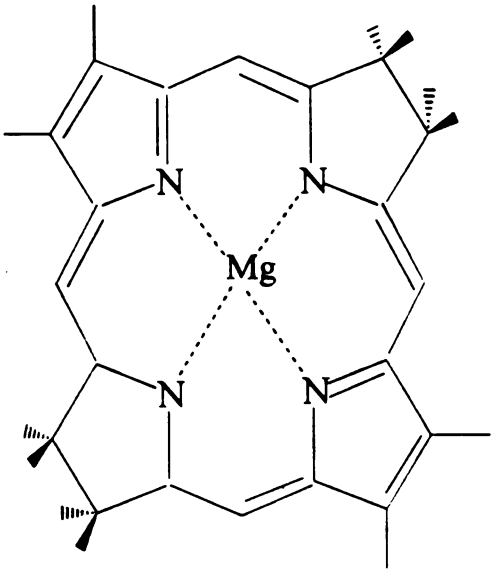

C. Bacteriochlorin

Figure 3-1 - Comparison of A) porphyrin, B) chlorin and C) bacteriochlorin compounds

clarity, in spite of the fact that the symmetry of chlorin and bacteriochlorin compounds deviates from "pure" D_{4h} symmetry.[16]

For the chlorin, *ab initio* molecular fragment and iterative extended Huckel (IEH) calculations predict that the a_{1u} MO lies in close proximity to another orbital of different symmetry, the a_{2u}.[17] The relative energies of these two π orbitals can be affected by ring substituents, the identity of the central metal and, or, the presence of axial ligands.[18] In the porphyrin, the π^* LUMO and LUMO + 1, e_{gx} and e_{gy}, represent a "true" degenerate pair, since the x and y axes are equivalent in a molecule with D_{4h} symmetry. Saturation of the C_β-C_β bonds in the chlorin, however, removes this degeneracy and destabilizes the e_{gy} as well as the HOMO (either a_{1u} or a_{2u}). The destabilization of the HOMO with respect to the LUMO is reflected experimentally in the increasing ease of oxidation observed for bacteriochlorophyll a ($E^{ox}_{1/2}(CH_2Cl_2)$ = 0.64 V vs. NHE)[19] compared to that of chlorophyll a ($E^{ox}_{1/2}$ (CH_2Cl_2) = 0.74 V vs. NHE).[20] The ring saturation does not affect the LUMO, the reduction potentials of the two moieties are similar.[20,21]

The energy differences between the ground and excited states of the different porphyrin derivatives directly affects their optical properties and is manifested in the spectrum as an increasing red shift with concomitant changes in oscillator strength and intensity as the symmetry of the molecule is decreased. Additional modulation of these properties *in vivo* as compared to *in vitro* has been observed and is attributed to interactions of the chromophore with its protein environment through hydrogen bonding or axial ligation of the central metal atom.[18,22] Semi-empirical and *ab initio* calculations on bacteriochlorophyll analogues have correctly predicted the blue and red shifts

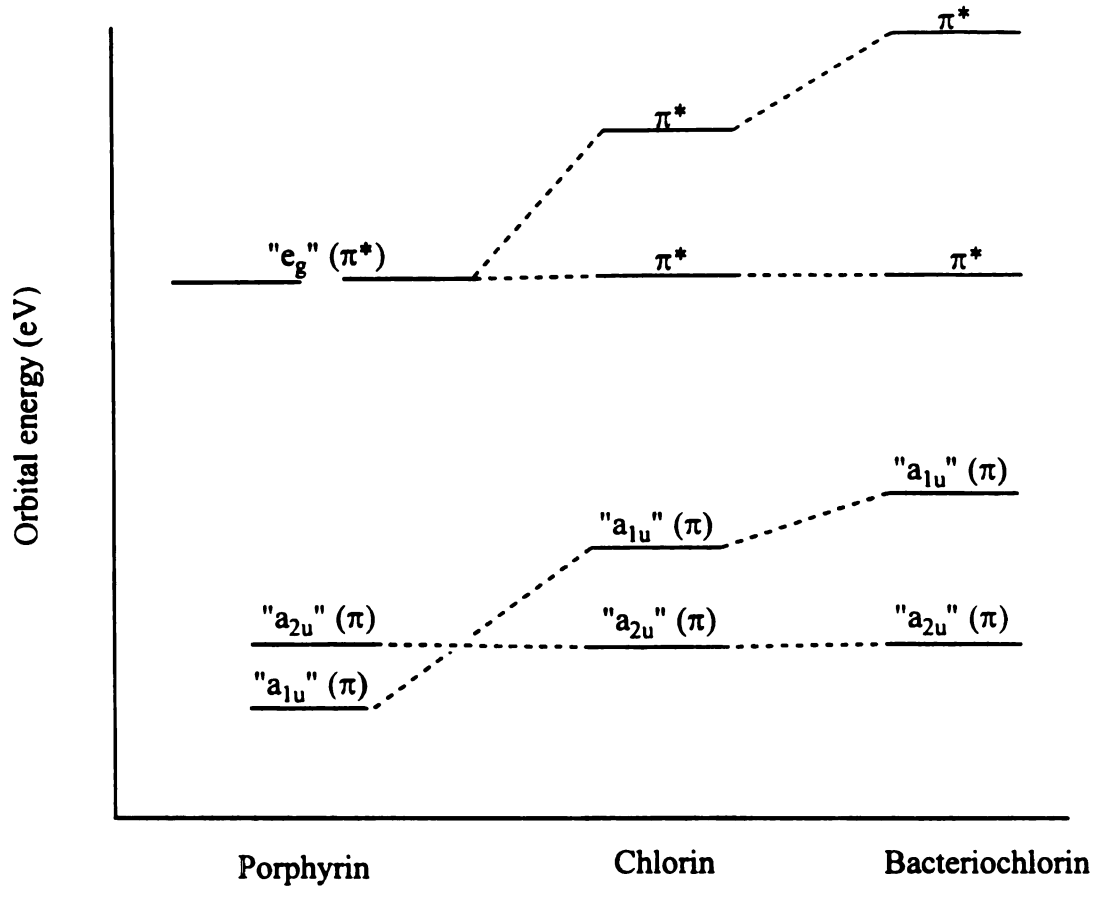

Figure 3-2: Energies of the highest occupied and lowest unoccupied molecular orbitals for Zn porphyrin, chlorin and bacteriochlorin compounds.[16]

observed in bacteriochlorophyll compounds containing hydrogen bonded residues at the 13'-keto or 3-acetyl positions, respectively.[23] Similar shifts are predicted with the addition of water or imidazole ligands to the axial metal atom.[23] The experimental data, though, show only minor perturbations, in ligating and hydrogen bonding solvents the optical spectra of bacteriochlorophyll a and bacteriopheophytin a remain essentially unaffected.[24] However, because the chlorin and bacteriochlorin molecules are so large, these calculations are performed with minimal basis sets and reflect only *trends* in behavior and, therefore, are not quantitative. Nevertheless, the basic trends that have emerged from these calculations combined with experimental results have provided a foundation for understanding the general features of the chlorophyll optical spectra, the redox properties and the unpaired spin density distributions in the anionic and cationic chlorophyll and bacteriochlorophyll species.

The magnetic properties of the cation radicals are also affected by the decrease in symmetry. The unpaired spin density distributions for the a_{1u} and a_{2u} MOs differ markedly.[25] The a_{1u} orbital is characterized by large unpaired spin densities on the carbons adjacent to the nitrogens while the unpaired spin in the a_{2u} orbital resides mainly on the meso carbons and the nitrogens. There is also unpaired spin density on the central metal atom for the a_{2u} MO. Calculations on Mg^{II} and Co^{III} metalloporphyrin cation radicals where the unpaired electron is in either the a_{1u} or a_{2u} MO reflect this disparity in unpaired spin density distributions, see Table 3-1.[26]

Table 3-1 Calculated π Spin Densities for Metalloporphyrin Cation Radicals

	$^2A_{1u}$		$^2A_{2u}$	
	Mg^{II}	Co^{III}	Mg^{II}	Co^{III}
C_α	0.098	0.102	0.0005	0.0005
C_β	0.027	0.023	0.019	0.014
C_{meso}	0.000	0.000	0.151	0.135
nitrogen	0.000	0.000	0.043	0.069
metal	0.000	0.000	0.009	not measured

Magnetic resonance spectroscopy is an invaluable tool for studying these differences because elucidation of the electron-nuclear hyperfine coupling constants for a radical provides a direct measurement of its singly occupied molecular orbital (SOMO). For example, in chlorophyll a cation radical monomeric model compounds, a marked temperature dependence of the proton hyperfine couplings at positions 17 and 18 has been observed.[27] The magnitude of these couplings decreases as a function of increasing temperature[27] and is evidence for thermal mixing of the ground and first excited states, as the proximity of the a_{2u} MO allows thermal accessibility upon an increase in temperature. A similar decrease in hyperfine couplings is observed when the chlorophyll a compound is studied in ligating solvents.[19] Axial ligation of the central Mg atom may induce mixing between the ground a_{1u} and first excited a_{2u} states by lowering the energy of the a_{2u} orbital. This hypothesis is supported by IEH calculations.[28] In the bacteriochlorophyll, however, the singly occupied a_{1u} lies well above the a_{2u}[16] and therefore the small perturbations in electronic structure that result from axial ligation or interactions with the protein environment do not perturb the energetics of the system enough to bridge the energy gap between the orbitals and the probability of state mixing is smaller. This is evidenced

experimentally[29] as axial ligation and hydrogen bonding have been found to have little effect on the unpaired spin density distributions. These differences in unpaired spin density distributions of the cation radicals of the primary donors in these systems and their effect on function will be explored in greater detail in Chapter 4.

Axial Ligation of P_{700}^{+} in PSI

X-ray crystallographic studies of the bacterial reaction centers have shown that the primary donor in these systems consists of a dimer of BChl with each BChl having a single histidine ligand.[9,10] Recent chemically induced dynamic nuclear polarization experiments have confirmed the presence of this nitrogen based.[30] Specific mutation of either of these ligands to leucine or phenylalanine[31] results in the loss of Mg^{2+} from the associated BChl and the generation of a BPheo.[32] Interestingly, the replacement of histidine with glycine does *not* result in the generation of a BPheo; a coordinating water molecule is thought to stabilize the P^{+} structure.[33]

The identity of the axial ligand(s) to P_{700}^{+} remains uncertain as previous attempts at identification by using a combination of biochemical manipulation and subsequent spectroscopic evaluation have been inconclusive.[34] The presence of histidine ligands to P^{+} in the bacterial reaction centers, as well as conserved histidine residues in the amino acid sequence of psaB, the PSI protein known to bind P_{700}, suggests this residue as the most likely candidate[35,11] Recent proton ENDOR and ESEEM experiments on mutants of *Chlamydomas reinhardtii* indicate that the observed spectroscopic properties of the primary donor in this system are not affected by mutations of his523, a highly conserved

residue that is a good candidate for the putative histidine ligand to P_{700}^{+}.[34] These mutations were expected to generate a pheophytin, analogous to the bacterial system, however the ENDOR and ESEEM spectra collected on these mutants (H523Q and H523L) failed to detect any changes in the unpaired electron spin distribution for the radical. Because the spin density distribution for a pheophytin molecule differs considerably from that of chlorophyll[36] , it was concluded that H523 is not a ligand to P_{700}^{+}. The possibility that the induced mutations could have allowed water access to the binding site as a bridging ligand,[33] preserving the integrity of the P_{700}^{+} structure, could not be ruled out. Moreover, since the X-band ESEEM spectrum is dominated by contributions from the pyrrole nitrogen atoms of the Chl a macrocycle, perturbations in the hyperfine coupling resulting from changes to the axial ligand would be difficult to detect.

However, because the EPR signal from P_{700}^{+} consists of a single resonance line [37] that is inhomogeneously broadened by the presence of multiple overlapping hyperfine interactions, information regarding the magnitude of these hyperfine coupling constants is obscured. These couplings can be resolved by the application of advanced EPR techniques. ^{1}H and ^{15}N ENDOR and electron spin echo envelope modulation (ESEEM) studies on frozen solutions of PSI have indicated[38] that P_{700}^{+} is a dimeric Chl a species characterized by an asymmetrical spin density distribution similar to that found in the bacterial reaction centers.[39]

The recent development of histidine-tolerant mutants[40] of the cyanobacterium *Synechocystis* PCC 6803 has allowed for specific isotopic labeling of the histidine nitrogens. By using a combination of ENDOR and ESEEM spectroscopies and these

specifically labeled samples, we are able to present the first definitive spectroscopic evidence for a histidine ligand in P_{700}^{+}.

Materials and Methods

Strains and Cell Growth. A histidine-tolerant strain was isolated from the cyanobacterium *Synechocystis* PCC 6803 as described previously.[40] Cells of this strain were grown photoautotrophically at 30° C for 5 days in 10-L carboys by using cool-white fluorescent lamps (7 W/m2). BG-11 medium[41] was supplemented with 240 μM of either DL-histidine containing only natural-abundance ^{14}N, or DL-histidine containing two ^{15}N atoms in its imidazole group. For ^{15}N global labeling, 99.9% ^{15}N- nitrate was used as the sole nitrogen source during cell growth. For ^{14}N-histidine-reverse labeling, this ^{15}N nitrate containing BG-11 medium was supplemented with 240 μM ^{14}N histidine. The growth medium was bubbled with 5% CO_2 in air. With these experimental conditions, approximately 85% of the histidine molecules incorporated into thylakoid proteins were from the histidine supplemented in the growth medium as shown previously by mass analysis of histidine.[40]

Preparation of PSI core complexes: PSI core complexes were purified according to the procedure described earlier.[42] The complexes were eluted from DEAE-Toyopearl 650s column by using 50 mM $MgSO_4$ in 50 mM MES-NaOH buffer (pH=6.0) containing 0.03% dodecylmaltoside, 25% (w/v) glycerol, 5 mM $MgCl_2$ and 20 mM $CaCl_2$. The samples were desalted by passage through a gel filtration column (Econo-pak 10DG, Bio-

Rad) equilibrated with 50 mM HEPES-NaOH (pH=7.5) buffer containing 10 mM NaCl and 0.03% dodecylmaltoside, and then concentrated down to about 15 mg chl/mL by using centricon 100 (Amicon). To generate P_{700}^{+}, 1 mM potassium ferricyanide was added to the samples. Finally, the samples were loaded into 4 mm O.D. EPR tubes and frozen in liquid nitrogen.

ENDOR spectroscopy and data analysis: The ENDOR data were obtained at X-band on a Bruker ESP300e spectrometer with a Bruker ESP360 DS ENDOR accessory and home-built demountable coils.[43] All ENDOR data were collected at a field position corresponding to the center of the EPR absorption line. Constant temperature in the cavity was maintained with an Oxford ESR900 continuous flow cryostat. Microwave frequency was determined by using an EIP Microwave Model 25B frequency counter and the static magnetic field strength was measured with a Bruker ER035M NMR gaussmeter

The peaks attributed to ^{15}N (I=1/2) electron nuclear hyperfine coupling are expected to be split symmetrically about the nuclear Larmor frequency for ^{15}N (ν_{15N} = 1.45 MHz at 3500 G). In solution ENDOR, the position of these peaks is indicative of the strength of the isotropic hyperfine coupling according to the relationship[44]

$$\nu_{\pm} = \nu_N \pm A_{iso}/2$$

where $\nu_N \geq A_{iso}/2$. However, in frozen solution, the anisotropy of the hyperfine coupling gives rise to powder lineshapes described to first order by

$$\nu_{\pm} = \nu_N \pm A/2$$

$$\text{where } A = A_{\parallel} \cos^2\theta + A_{\perp} \sin^2\theta$$

$A_{||}$ and $A_{\perp}$ in the above expression are the principal values of the axially symmetric hyperfine tensor and θ describes the orientation of the principal axis system of the hyperfine tensor with respect to the laboratory magnetic field.[45]

ESEEM data collection and analysis: ESEEM data were collected on a home built spectrometer[46] by using a reflection cavity where either folded stripline[47] or slotted-tube structures[48] served as the resonant element. A three pulse or stimulated echo (90°-τ-90°-T-90°) pulse sequence was used. Dead time reconstruction was performed prior to Fourier transformation as described.[49] Computer simulations of the ESEEM data were performed on a Sun Sparcstation 2 computer utilizing FORTRAN software based on the density matrix formalism of Mims.[50] The analysis software for the treatment of experimental and simulated ESEEM data was written with Matlab (Mathworks, Nantick, MA). The experimental dead time was included in the simulations. An isotropic g-tensor was assumed in all of the calculations. The success of the spectral simulations was based on the modulation depth and duration observed in the time domain traces as well as the lineshapes, peak positions and relative peak intensities in the frequency spectra.

Results

The use of ENDOR spectroscopy in conjunction with ESEEM in these studies exhibits the complementarity of the two techniques. Couplings containing a large dipolar component are usually difficult to detect with ENDOR, since the broadened powder patttern lineshape precludes resolution of the turning points. In contrast, the dipolar

portion of the hyperfine coupling mixes the nuclear states within each electron spin manifold and enables the "forbidden" EPR transitions that give rise to ESEEM. Similarly, purely isotropic hyperfine couplings will result in discrete EPR transitions from each hyperfine level and eliminate the interference effects that give rise to the modulations.[50] ENDOR spectroscopy can, therefore, be used to resolve primarily isotropic nitrogen couplings, while ESEEM is suited best for hyperfine couplings that contain a considerable dipolar contribution. The degree of this contribution can be quantitated by applying both techniques.

The ENDOR first derivative spectrum collected at 6 K for P_{700}^{+} globally labeled with ^{15}N is shown in Figure 3-3 (top). The analogous spectrum from P_{700}^{+} specifically labeled with ^{15}N histidine and "reverse" labeled so that all nitrogens are ^{15}N except those of histidine, which contains natural abundance ^{14}N, are shown in Figure 3-3, middle and bottom, respectively. Features observed in the spectra of Figure 3-3 are expected to arise from all ^{15}N nuclei coupled to the electron spin; these include nitrogens in the chlorophyll macrocycle as well as in the putative histidine ligand. By using specific isotope labeling, identification of the peaks arising from this ligand is facilitated. The peaks at 1.13 and 1.78 MHz appear in the spectrum from the globally labeled sample (Fig. 3-3, top) as well as in the spectrum from P_{700}^{+} containing ^{15}N labeled histidine (Fig. 3-3, middle). Upon reverse labeling, these peaks disappear (Fig. 3-3, bottom), thus confirming histidine as their origin. These features are split symmetrically about the Larmor frequency for ^{15}N and correspond to an isotropic hyperfine coupling of 0.64 MHz. Moreover, features in the 2-3 MHz region can be assigned definitively to contributions from the nitrogens in the chlorophyll *a* macrocycle. A comprehensive analysis of these chlorophyll pyrrole

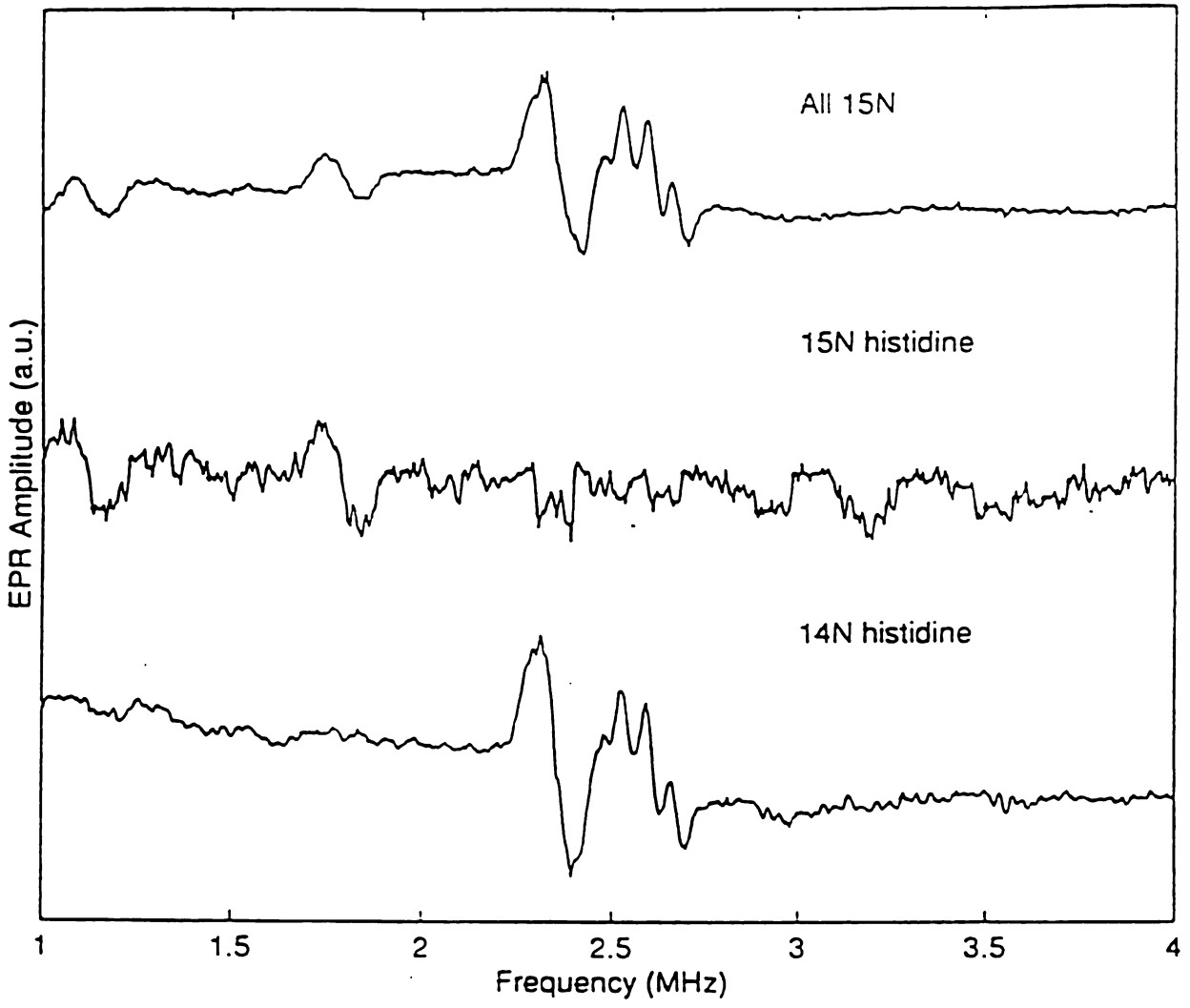

Figure 3-3: ENDOR spectra collected at 6K for P_{700}^{+} globally labeled with ^{15}N (top), specifically labeled with ^{15}N histidine (middle) and "reverse" labeled, ^{14}N histidine in the presence of ^{15}N nitrate (bottom). Spectrometer conditions for all spectra, unless otherwise indicated: microwave power, 1.99 mW; magnetic field strength, 3375 G (top), 3356 G (middle), 3367 G (bottom); RF power, 200 W; RF frequency modulation, 100 kHz.

nitrogen couplings by using multifrequency ESEEM and ^{15}N ENDOR is presented in Chapter 4.

The presence of this nitrogen derived histidine coupling does not affect the ESEEM spectrum as demonstrated in Figures 3-4 and 3-5. The cosine Fourier transformation of three-pulse time domain data from P_{700}^+ containing natural abundance ^{14}N is identical (Figure 3-4, top) to the spectrum from P_{700}^+ specifically labeled with ^{15}N histidine (Figure 3-4, bottom). These spectra are dominated by ^{14}N modulations from the Chl a pyrrole nitrogens and are typical for situations where the hyperfine interaction is approximately equal to twice the nuclear Zeeman energy. Under these conditions the energy level splittings in the spin manifold where the nuclear Zeeman and electron-nuclear hyperfine interactions cancel is determined primarily by the ^{14}N nuclear quadrupole interaction. This exact cancellation condition is characterized by modulations that are deep and long-lived. Because these modulations will dominate the ESEEM spectrum, contributions from the nitrogen of the histidine ligand, which is away from exact cancellation, are not expected to be observed. To eliminate this deep ^{14}N ESEEM from our measurements, analogous three-pulse ESEEM experiments were performed on the ^{15}N enriched and "reverse" labeled samples (Figure 3-5, top and bottom, respectively). No differences were resolved in the spectra, indicating a minimal contribution to the ESEEM spectra from nitrogen hyperfine coupling originating from the histidine.[2]

Discussion

The presence of a histidine ligand bound to the central Mg^{2+} atom of P_{700}^+ has often been postulated as it has been shown to ligate the primary donor in the bacterial

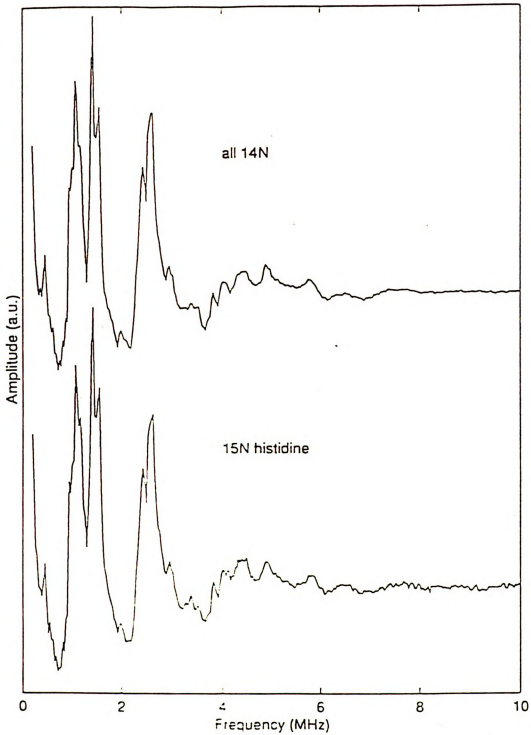

Figure 3-4: Fourier transformations of three-pulse ESEEM data from P_{700}^{+} containing natural abundance ^{14}N (top) and specifically labeled with ^{15}N histidine (bottom). Spectrometer conditions: magnetic field strength, 3210 (top), 3195 (bottom); microwave pulse power, 45 dBm; microwave pulse length (FWHM), 15 ns; pulse repetition rate, 20 Hz; tau value, 175 ns and sample temperature, 4K.

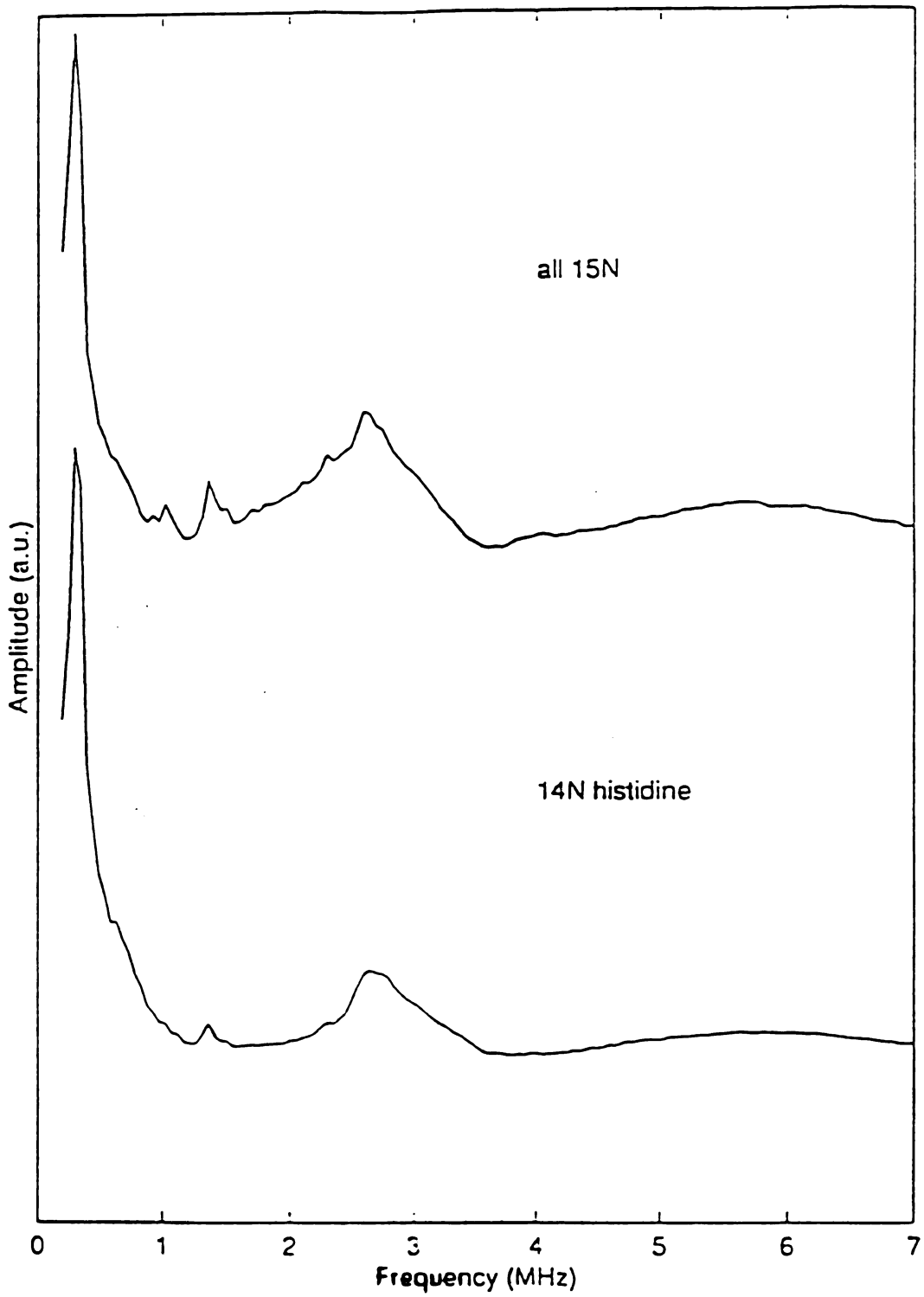

Figure 3-5: Three-pulse ESEEM frequency spectra from P_{700}^{+} globally enriched with ^{15}N (top) and "reverse" labeled (bottom). Spectrometer conditions: magnetic field strength, 3195 G; microwave pulse power, 45 dBm; microwave pulse length (FWHM), 15 ns; pulse repetition rate, 90 Hz; tau value, 250 ns; sample temperature 4K.

reaction center [9,10] [51] but until now, not demonstrated unambiguously. Spectroscopic characterization of this ligand is necessary to understand the optical and magnetic properties of the cation radical. Modulation of these properties is thought to occur by interactions of the chromophore with its protein environment through, for example, hydrogen bond interactions with nearby amino acid residues or through axial ligation to the Mg^{2+}. In heme proteins, cavity mutants generated by site directed mutagenesis allow the introduction of exogeneous organic ligands that greatly affect the functional properties of the protein[52]. A similar strategy to examine the effect of axial ligands on magnetic and optical properties of the primary donor of bacterial reaction centers has been applied by Goldsmith *et al.*[33] However the lack of an adequate spectroscopic probe has precluded characterization of the ligand. Identification of a histidine ligand to P_{700}^{+} provides the spectroscopic methodology necessary for characterization of these mutants.

It is possible, however, that the histidine derived nitrogen hyperfine coupling shown in Figure 3-3 arises from a histidine residue hydrogen bonded to the 9-keto group of the conjugated π system of the chlorophyll *a*. Amino acid residues interacting non-covalently with the primary electron donors in photosynthetic reaction centers from a variety of organisms have been suggested as the source of the disparity in their redox potentials and optical properties.[53] The role of H-bonded residues as redox potential "tuning modules" is not unusual in biological systems; it has been suggested as an explanation for the wide range of redox potentials observed for [nFe-mS] clusters[54] and has recently been shown to alter the internal charge transfer state in BChl-BPheo heterodimer mutants in bacterial reaction centers.[55] The precedence of histidine residues

in H-bonded interactions with P^+ has been demonstrated in the bacterial reaction centers.[56] Although the H-bonded histidine was not detected directly by spectroscopic methods, changes in the redox potential and unpaired electron spin density distribution subsequent to mutations of his L168 led to conclusions that this residue participates in a hydrogen bond with the 2-acetyl group of the BChl. However, because the spin density distribution of P^+ in bacterial reaction centers differs from that of P_{700}^+ in PSI[38] the lack of spectroscopic evidence for this H-bonded histidine does not preclude detection in PSI. Therefore, even without a covalent interaction, ENDOR spectroscopy could detect the coupling from a H-bonded moiety provided that sufficient dipolar coupling between the unpaired π-electron of the radical and the nitrogen nucleus are present.

Hydrogen-bonding interactions of this genre have been studied in other paramagnetic systems, both *in vivo* and *in vitro* and can provide information regarding the form of the hyperfine tensors expected. In powder samples, these interactions were characterized initially by O'Malley and Babcock[57] who used isotopic labeling and ENDOR spectroscopy to investigate H-bonds in p-benzoquinone anion radicals. The proton hyperfine coupling tensor for solvent protons H-bonded to the oxygen of the semiquinone radical in this system was shown to be axially symmetric. The ratio of -1:-1:2 for the principal values was determined and corroborated by earlier results from single crystal work.[58] *In vivo*, these interactions have been studied extensively in a variety of systems containing Fe-S centers. The hyperfine tensors of both the proton and nitrogen involved in the hydrogen bonding interaction have been determined from electron magnetic resonance experiments. Pulsed ^{1,2}H ENDOR and ^{2}H-^{2}H TRIPLE were

used by Doan *et al.*[59] to determine the intrinsic hyperfine coupling of three strong NH···S hydrogen bonds in the $[Fe_3S_4(cys)_3]^{2-}$ cluster in hydrogenase from *D. gigas*. Surprisingly, the hyperfine tensors for the protons hydrogen bonded to the cysteinyl sulfur contained a substantial isotropic interaction, although no covalent bond exists between the proton and sulfur atoms. Molecular orbital calculations have shown that the unpaired electron spin in these systems is highly centralized on the individual Fe atoms, as much as 80% of the total spin in the case of Fe^{2+}, and most likely contributes to the isotropic character of the proton coupling through a spin polarization or hyperconjugation mechanism.[60] Spin density is found on the peptide nitrogen nucleus as well and has been observed spectroscopically by Cammack *et al.*[61] from an Fe-S cluster of fumarate reductase from *Escherichia coli*. In these studies, the hyperfine and quadrupole parameters for a nitrogen atom assigned to an NH···S type hydrogen bond to the cluster were determined by using ESEEM spectroscopy and numerical simulations of the ESEEM data. Observation of the nitrogen coupling was again dependent on the presence of a large amount of unpaired spin density localized on the Fe of the cluster.

It is unlikely that these spectroscopic methods could be used to detect a H-bonded histidine in P_{700}^{+}. The spin density distribution on the 9-keto oxygen, although not determined definitively, has been estimated to be on the order of 0.4% in the chlorophyll *a* cation radical *in vitro*.[62] The majority of the unpaired spin in these systems is delocalized on the methine carbon atoms and the four nitrogen atoms.[63] However, if the peaks attributed to the nitrogen of the histidine observed in the ENDOR spectra of Figure 3-3 (top and middle) *do* represent the perpendicular components of a purely dipolar hyperfine tensor, then the corresponding parallel components would be expected in the 2

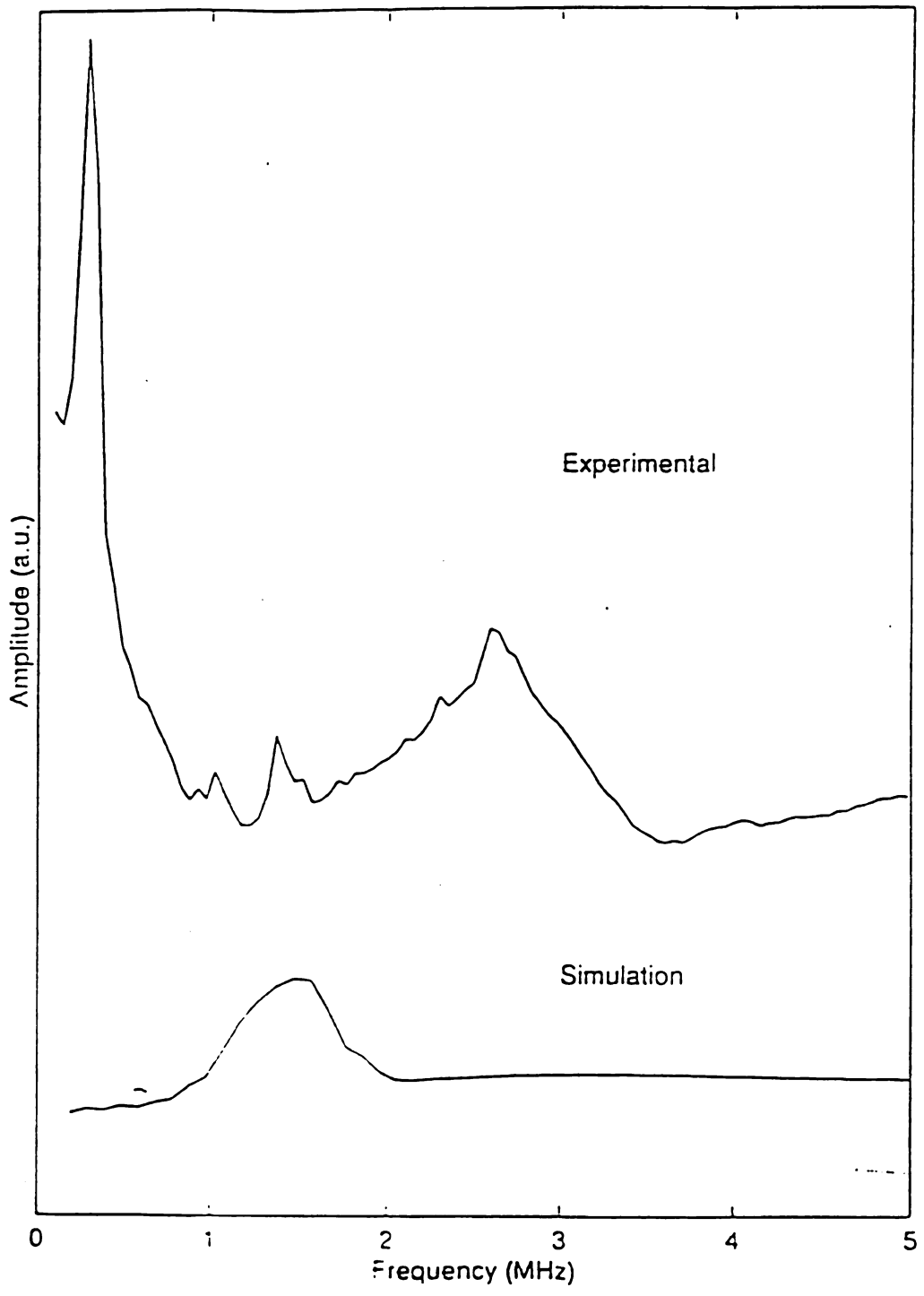

Figure 3-6: Fourier transformations of three-pulse experimental (top) and simulated (bottom) ESEEM spectra from P_{700}^{+} globally labeled with ^{15}N. Experimental conditions were identical to those of Figure 3-5. Simulation parameters: $A_{\perp}$ = -0.64 MHz, $A_{\parallel}$ = 1.28 MHz, all other parameters as in experiment.

MHz region of the spectra.. No discernible peaks can be seen in this frequency range in either of the spectra. The resolution of the parallel components of the hyperfine tensor can be difficult as the number of orientations with parallel symmetry contributing to the overall lineshape is small and the lack of these features is not indicative of a purely isotropic hyperfine interaction.

To estimate the dipolar contribution to the observed ^{15}N-histidine hyperfine coupling, numerical simulations of ESEEM data from ^{15}N enriched P_{700}^{+} were performed. Because the modulation depth observed in an ESEEM experiment relies on the quantum mechanical mixing of the nuclear states that occurs as a result of this contribution, it can be used to determine the dipolar character of a coupling. ^{15}N ESEEM simulations using a purely dipolar tensor, $A_{\perp}$ = -0.64 MHz, $A_{\parallel}$ = 1.28 MHz, predict that a broad feature, centered at the ^{15}N Larmor frequency, 1.4 MHz, would be observed under our experimental conditions (see Figure 3-6). These simulations indicate that the peaks observed in the ENDOR spectrum are primarily isotropic in character and are consistent with a nitrogen participating in a covalent bond with the Mg^{2+}.

The presence of an isotropic coupling to the nitrogen of the histidine ligand implies a non-zero spin density on the Mg^{2+} atom of P_{700}^{+}. Molecular orbital calculations on chlorophyll *a* monomers have shown that the availability of a low lying excited state with a decidedly different spin distribution that can influence the electronic structure of the radical and subsequently its magnetic resonance characteristics.[62] The spin density distribution of this excited state A_{2u} molecular orbital includes spin delocalized on the Mg^{2+} atom.[27] ENDOR experiments comparing the magnitude of proton hyperfine couplings in P_{700}^{+} to those of chlorophyll *a* model compounds led O'Malley and

Babcock[64] to suggest that the ground state orbital for P_{700}^{+} contains 75% ground state and 25% excited state character. These researchers suggested that interactions of P_{700}^{+} with its protein environment, either through axial ligation of the Mg^{2+} atom or by electrostatic interactions of the radical with nearby charged amino acid residues, could provide the perturbation necessary to mix the ground and excited state molecular orbitals. These data and the presence of a spectroscopically active histidine ligand to P_{700}^{+} exhibiting an isotropic hyperfine interaction are supportive of a model of P_{700}^{+} where the excited state orbital makes a significant contribution to the spin density distribution of the cation radical and may explain the differences in redox potentials and optical properties observed for the plant and bacterial primary donor species.

LIST OF REFERENCES

LIST OF REFERENCES

[1] Mitchell, P. (1961) *Nature 191*, 144.

[2] Chance, B. & Nishimura, M. (1960) *Proc. Natl. Acad. Sci. USA 46*, 19.

[3] Devault, D. & Chance, B. (1966) *Biophys. J. 6*, 825

[4] Marcus, R.A. (1956) *J. Chem. Phys. 24*, 966; Marcus, R.A. & Sutin, N. (1985) *Biochim. Biophys. Acta 811*, 265

[5] Levich, V.G. & Dogonadze, R.R., (1959) *Dokl. Adad. Nauk USSR 124*, 123

[6] Jornter, J. (1976) *J. Chem. Phys. 64*, 4860

[7] Moser, C.C., Keske, J.M., Warncke, K., Farid, R.S., Dutton, P.L. (1992) *Nature 355*, 796.

[8] Michel, H., Deisenhofer, J. & Epp, O. (1986) EMBO J. 5, 2445

[9] Deisenhofer, J., Epp, O., Miki, K., Huber, R. & Michel, H. (1985) *Nature 318*, 618-624.

[10] Allen, J.P., Feher, G., Yeates, T.O., Komiya, H. & Rees, D.C. (1987) *Proc. Natl. Acad. Sci. USA 84*, 5730-5734.

[11] Golbeck, J. (1992) *Annu. Rev. Plant Physiol. Plant Mol. Biol, 43*, 293-324.

[12] Michel, Beyerle, M.E. (1988) *Biochim. Biophys. Acta 932*, 52.

[13] Fromme, P., Witt, H.T., Schubert, W.-D., Klukas, O., Saenger, W. & Krauss, N. (1996) *Biochim. Biophys. Acta 1275*, 76-83;

[14] Gouterman, M. (1978) in *The Porphyrins*, Vol. 3, (Dolphin, D., ed.) Academic Press, New York, Chapter 1.

[15] Weiss, C., (1972) *J. Mol. Spectrosc. 44*, 37.

[16] Chang, C.K., Hanson, L.K., Richardson, P.F., Young, R., & Fajer, J. (1981) *Proc. Natl. Acad. Sci. USA 78*, 2652.

[17] Spangler, D., Maggiora, G.M., Shipman, L.L. & Christoffersen.R.E., (1977) *J.Am. Chem. Soc. 99*, 7470;

[18] Fajer, J. & Davis, M.S. (1979) in *The Porphyrins*, Vol. 4 (Dolphin, D., ed.) Academic Press, New York, Chapter 4

[19] Davis, M.S., Forman, A. & Fajer, J. (1979) *Proc. Natl. Acad. Sci. USA 76*, 4170.

[20] Fajer, J., Brune, D.C., Davis, M.S., Forman, A. & Saulding, L.D. (1975) *Proc. Natl. Acad. Sci. USA 72*, 4956.

[21] Fujita, I., Davis, M. S. & Fajer, J. (1978) *J. Am. Chem. Soc. 100*, 6280.

[22] Callahan, P.M. & Cotton, T.M. (1987) *J. Am. Chem. Soc. 109*, 7001.

[23] Hanson, L.K., Thompson, M.A. & Fajer, J. (1987) in *Progress in Photosynthesis Research*, Vol. 1, (Biggins, J., ed.) Martinus Nijhoff, Dordrecht, 311.

[24] Cotton, T.M. & Van Duyne, R. P. (1981) *J. Am. Chem. Soc. 103*, 6020.

[25]; Davis, M.S., Forman, A., Hanson, L.K., Thornber, J.P. & Fajer, J. (1979) *J. Phys. Chem. 83*, 3325.

[26] Edwards, W.D. & Zerner, M.C. (1986) *Can. J. Chem. 63*, 1763.

[27] Fajer, J., Davis, M.S., Brune, D.C., Spaulding, L.D., Borg, D.C. & Forman, A. (1977) *Brookhaven Symp. Biol. 28*, 74.

[28] Fajer, J., Fujita, M.S., Davis, M.S., forman, A., Hanson, L.K. & Smith , K.M. (1982) in *Electrochemical and Spectrochemical Studies of Biological Redox Components*, ACS Advances in Chemistry, No. 201 (Kadish, K.M., ed.) American Chemical Society, Washington D.C., 489.

[29] Horning, T.L., Fujita, E. & Fajer, J. (1986) *J. Am. Chem. Soc. 108*, 323.

[30] Zysmilich, M.G. & McDermott, A.E. (1994) *J. Am. Chem. Soc. 116*, 8362-8363.

[31] Schenck, C.C., Gaul, D., Steffen, M., Boxer, S.G., McDowell, L., Kirmaier, C. & Holten, D. (1990) in *Reaction Centers of Photosynthetic Bacteria: Feldafing II* (Michel-Beyerle, M.E., ed.) pp. 229-238, Springer Verlag, Berlin.

[32] Bylina, E.J. & Youvan, D.C. (1988) *Proc. Natl. Acad. Sci. USA 85*, 7226-7230.

[33] Goldsmith, J.O., King, B. & Boxer, S.G. (1996) *Biochemistry. 35*, 2421-2428.

[34] Cui, L., Bingham, S.E., Kuhn, M., Kass, H., Lubitz, W. & Webber, A.N. (1995). *Biochemistry 34*, 1549-1558.

[35] Robert, B. & Moenne-Loccoz, P. (1990) in *Current Research in Photosynthesis* (Baltscheffsky, M., ed.) Vol. I, pp 65-68, Kluwer, Dordrecht, The Netherlands.

[36] Plato, M., Mobius, K. & Lubitz, W. (1990) in *Chlorophylls* (Scheer, H., ed) pp 1015-1042, CRC Press, Boca Raton

[37] Commoner, B., Heise, J.J. & Townsend, J. (1956) *Proc. Natl. Acad. Sci. USA 42*, 710.

[38] Davis, I.H., Heathcote, P., MacLachlan, D.J. & Evans, M.C.W. (1993) *Biochim. Biophys. Acta 1143*, 183-189. Käβ, H., Bittersmann-Weidlich, E., Andreasson, L.-E., Bonigk, B. & Lubitz, W. (1995) *Chem. Phys, 194*, 419-432. Käβ, H. & Lubitz, W. (1996) *Chem. Phys. Lett, 251*, 193-203.

[39] Lendzian, F., Lubitz, W., Scheer, H., Hoff, A.J., Plato, M., Trankle, E. & Mobius, K. (1988) *Chem. Phys. Lett. 148*, 377-385.

Lendzian, F., Huber, M., Isaacson, R.A., Endeward, B., Plato, M., Bonigk, B., Mobius, K., Lubitz, W. & Feher, G. (1993) *Biochim. Biophys. Acta 1183*, 139-160.

[40] Tang, X.-S., Diner, B.A., Larsen, A.S., Gilchrist, M.L., Lorigan, G.A. & Britt,R.D. (1994) *Proc. Natl. Acad. Sci. USA 91*, 704-708.

[41] Rippke, R., DeRuelles, J., Waterbury, J.B., Herdman, M. & Starkier, R.Y. (1979) *J. Gen. Microbiol. 111*, 1-61.

[42] Tang, X.-S. & Diner, B.A. (1994b) *Biochemistry 33*, 4595-4603.

[43] Bender, C.J., Sahlin, M., Babcock, G.T., Barry, B.A., Chandrashekar, T.K., Salowe, S.P., Stubbe, J., Lindstrom, B., Petersson, L., Ehrenberg, A. & Sjoberg, B.-M. (1989) *J. Am. Chem. Soc. 111*, 8076-8083.

[44] Kevan, L. & Kispert, L.D. (1976) in *Electron Spin Double Resonance Spectroscopy*, pp 2-57, John Wiley and Sons, New York.

[45] Blinder, S.M. (1960), *J. Chem. Phys 33*, 748-752.

[46] McCracken, J., Shin, D.-H & Dye, J.L. (1992) *Appl. Magn. Reson 3*, 30.

[47] Lin, C.P., Bowman, M.K. & Norris, J.R. (1985) *J. Magn. Res. 65*, 369-374.

[48] Mehring, M. & Freysoldt, F. (1980) *J. Phys. E: Sci. Instrum.* 13, 894-895.

[49] Mims, W.B.(1984) *J. Magn. Reson. 59*, 291-306.

[50] Mims, W.B. (1972) *Phys. Rev. B 5*, 2409-2419.

[51] El-Kabbani, O., Chang, C.-H., Tiede, D., Norris, J. & Schiffer, M. (1991) *Biochemistry 30*, 5361-5369.

[52] DePillis, G.D., Decatur, S.M., Barrick, D. & Boxer, S.G. (1994) *J. Am. Chem. Soc. 116*, 6981-6982.

[53] Lin, S., Murchison, H.A., Nagarajan, V., Parson, W.W., Williams, J.C. & Allen, J.P. (1994) *Proc. Natl. Acad. Sci. USA 91*, 10265-10269.

[54] Backes, G., Mino, Y., Loehr, T.M., Meyer, T.E., Cusanovich, M.A., Sweeney, W.V., Adman, E.T. & Sanders-Loehr, J. (1991) *J. Am. Chem. Soc. 113*, 2055-2064.

[55] Allen, J.P., Artz, K., Lin, X., Williams, J.C., Ivancich, A., Albouy, D., Mattioli, T.A., Fetsch, A., Kuhn, M. & Lubitz, W. (1996) *Biochemistry, 35*, 6612-6619.

[56] Rautter, J., Lendzian, F., Lubitz, W., Wang, S. & Allen, J.P. (1994) *Biochemistry, 33*, 12077-12084.

[57] O'Malley, P.J. & Babcock, G.T. (1986) *J. Am. Chem. Soc, 108*, 3995-4001.

[58] Reddy, M.V.V.S., Lingam, K.V. & Gundu Rao, T.K. (1982) *J. Chem. Phy. 35*, 4398.

[59] Doan, P.E., Fan, C. & Hoffman, B.M. (1994) *J. Am. Chem. Soc. 116*, 1033-1041.

[60] Mouesca, J.-M., Noodleman, L., Case, D.A. & Lamotte, B. (1995) *Inorg. Chem, 34*, 4347-4359.

[61] Cammack, R., Chapman, A., McCracken, J., Cornelius, J.B., Peisach, J. & Weiner, J.H. (1988) *Biochim. Biophys. Acta 956*, 307-312.

[62] Petke, J.D., Maggiora, G.M., Shipman, L.L. & Christoffersen, R.E. (1980) *Photochemistry and Photobiolog, 31*, 243-257.

[63] Hanson, L.K. (1990) in *Chlorophylls* (Scheer, H., ed) pp 1015-1042, CRC Press, Boca Raton

[64] O'Malley, P. J. & Babcock, G.T. (1984) *Proc. Natl. Acad. Sci. US, 81*,1098-1101.

Chapter 4

Multifrequency ESEEM Studies of the Primary Electron Donor in PSI: The Electronic Structure of P_{700}^{+}

Background

Oxygenic photosynthesis in higher plants and cyanobacteria requires the interplay of two pigment-protein reaction centers, Photosystem I[1] and Photosystem II[2] (PSI and PSII). In each of these reaction centers, the primary charge separation event proceeds via the light-induced generation of a chlorophyll a cation radical species (P_{700} in PSI and P_{680} in PSII). This photochemically active chlorophyll is distinguished from the light harvesting and energy transfer chlorophylls by its spectral and redox properties. After initial charge separation, subsequent electron transfer events occur on a timescale fast enough to prevent recombination. This highly effective unidirectional electron transfer occurs with a quantum yield approaching unity. Because these events are controlled by the spatial and electronic arrangement of the cofactors involved, knowledge regarding the structure of these radicals is imperative to understand better the electron transfer process in photosynthetic systems.

Although significant progress has been made[3], the lack of a high resolution crystal structure in the higher plant and cyanobacterial systems has precluded determination of the nuclearity of the primary donor in PSI. The recent 4.5 Å crystal structure by Fromme *et al.*[3] indicates a dimeric structure for the primary donor and is supportive of earlier hypotheses that indicate that P_{700}, in its ground state, is a dimer of chlorophyll a.[4] Additional evidence for a dimeric structure comes from early magnetic resonance studies by Norris and coworkers[5] who found that the EPR spectrum of P_{700}^{+} is

narrower by a factor of $1/\sqrt{2}$ with respect to the monomeric chlorophyll species *in vitro*. Because the EPR spectra arising from chlorophyll aggregate species have been found to be $1/\sqrt{N}$ narrower than the corresponding monomeric species, the observed narrowing of the P_{700}^{+} EPR signal was taken to indicate that the primary donor *in vivo* is dimeric.[5] However, because the internal spin redistributions originating from protein interactions in chlorophyll species *in vivo* may alter substantially the linewidth by moving spin density away from the methyl groups onto carbons with no protons, these results are not conclusive.

Evidence from second moment analysis of these EPR signals, however, is supportive of a monomeric structure. Wasielewski and coworkers[6] have found that in cation radicals of P_{700}^{+} isotopically enriched with ^{2}H and ^{13}C, the second moment is similar to that of monomeric chlorophyll. Although this analysis correctly predicted the nuclearity of the primary donor in the bacterial systems, the data have questionable applicability in PSI since this technique is generally invalid for the non-Gaussian lineshapes observed for P_{700}^{+}, and, moreover, slight spin density distribution changes in the system can alter significantly the magnitude of the second moment.

Studies of the triplet state of P_{700}^{+} have determined that the zero field splitting parameter (D) is similar to those obtained for monomer chlorophyll a species *in vitro*.[7] These results do not definitively identify P_{700}^{+} as a monomer since a dimeric species with plane parallel macrocycle rings would yield D values similar in magnitude to that of the monomeric species.

The discrepancies in the magnetic and optical properties of P_{700}^{+} when compared to monomeric chlorophyll a *in vitro* may stem, ultimately, from interactions with the

protein present *in vivo*. These interactions have been implicated as the source of the experimentally observed red shifts of the long absorption band of neutral P_{700} relative to the monomeric chlorophyll a species.[8] These shifts had previously been attributed to a large exiton interaction between two closely spaced chlorophyll molecules.[9] It has subsequently been shown that interactions with charged amino acid groups can also effect these types of absorption changes in chlorophyll a and bacteriochlorophyll a model compounds.[10]

The electronic structure of the cation radical is elusive as well and, although both monomeric[11] and dimeric[5] unpaired spin density distributions have been suggested for P_{700}^{+}, neither has been proven conclusively and the ambiguity surrounding its electronic structure remains. Since the three dimensional structures of the bacterial reaction centers from *Rhodopseudomonas viridis*[12] and *Rhodobacter sphaeroides* [13] have been determined to high resolution by using X-ray crystallography, these systems have been used as a model for the oxygen evolving systems of higher plants and cyanobacteria. The bacterial reaction centers consist of a single photosystem with approximate C_2 symmetry. Electron transfer proceeds unilaterally down the L branch of the protein . The primary donor (P^{+}) has been shown to be a dimer of bacteriochlorophyll, however, the presence of quinones as terminal electron acceptors in the bacterial reaction centers makes this system more analogous to PSII than PSI, which uses iron-sulfur centers as terminal electron acceptors.

The presence of an easily trapped light-induced radical species makes each of these systems (eukaryotic and prokaryotic) especially amenable to the application of electron magnetic resonance techniques. Electron paramagnetic resonance (EPR) and ^{1}H Electron Nuclear Double Resonance (ENDOR) studies of single crystals of P^{+} from

bacterial reaction centers have shown that the unpaired electron is distributed asymmetrically over the two halves of the bacteriochlorophyll dimer, favoring the L branch by approximately a 2:1 ratio.[14] This asymmetry has been attributed to structural differences in the protein environments of the two bacteriochlorophylls, which manifest themselves as shifts the energy of the highest filled molecular π orbitals of the bacteriochlorophyll monomers. The asymmetry observed may contribute to the high efficiency of forward electron transfer by moving the hole away from the primary electron acceptor It has been hypothesized that this asymmetry also occurs in P_{700}^{-}.

Recent ^{1}H and ^{15}N ENDOR studies on frozen solutions of PSI have indicated either a very highly asymmetric, or completely monomeric, unpaired electron spin density distribution over the chlorophyll a dimer for P_{700}^{+}.[15] However, in systems with multiple anisotropic hyperfine couplings, unequivocal structural assignments from powder pattern ENDOR spectra are difficult to make, as often, only the turning points of the hyperfine coupling tensor are observed and correlation of these components to a specific ^{15}N nucleus is difficult without using specific isotope labeling. Also, the relative intensities of the ENDOR lines are not proportional to the number of coupled nuclei contributing.

In contrast, the modulation amplitudes in electron spin echo modulation (ESEEM) experiments are related directly to the relative populations of spin systems in the sample. Additionally, ESEEM can be used to probe directly small hyperfine couplings usually not resolved in conventional continuous wave EPR, and therefore provides information

regarding the electronic structure of these radical species. ESEEM is also ideal for detection of hyperfine couplings to nuclei like nitrogen with low gyromagnetic ratios.

In ESEEM, the amplitude of the spin echo induced by a series of microwave pulses is modulated by interactions with nearby magnetic nuclei. The frequency of these modulations can be related directly to the hyperfine and quadrupole (for nuclei with $I \geq 1$) interactions of the coupled nucleus. The magnitude of the hyperfine coupling is proportional to the fraction of unpaired electron spin residing on the coupled nucleus and thus yields useful information regarding the radical's electronic structure. Both one dimensional and two-dimensional ESEEM (Hyperfine Sublevel Correlation Spectroscopy, or HYSCORE) experiments have been used to measure the ^{14}N hyperfine and nuclear quadrupole (NQI) interactions in P_{700}^{+}.[15] However, spectral simulations of these ESEEM data have not been successful in determining these parameters conclusively. This precludes quantization of the number of ^{14}N nuclei giving rise to a particular hyperfine interaction. Here, we report results of multifrequency ESEEM experiments and corresponding spectral simulations of experimental ESEEM data of P_{700}^{+} containing either natural abundance ^{14}N or isotopically enriched with ^{15}N. The simulations indicate that the three-pulse ESEEM spectra arise from four nitrogens coupled to the unpaired electron, the hyperfine couplings of these nitrogens are indicative of a monomeric unpaired electron spin distribution.

Materials and Methods

Growth of Cells

Cells of *Synechocystis PCC* 6803 were grown under photoautotrophic conditions, with aeration, in BG-11. In order to label cells uniformly with ^{15}N, KNO_3 (18 mM) in the growth medium was replaced by 18 mM $K^{15}NO_3$ (purity >98 %,Cambridge Isotope Laboratories, Andover, MA). Amounts of ^{14}N arising from other nitrogen containing compounds in the medium accounted for less than 0.002 % of the total nitrogen. When cell growth had reached the late log phase (O.D. 600 >1.2), the cells were harvested by continuous-flow centrifugation at 4° C, washed twice and resuspended in BG-11. Glycerol was added to the cell suspension to 15 % (v/v), the suspensions were mixed thoroughly and stored at -70° C.

Preparation of Photosystem I Particles

Thylakoid membrane preparation and purification of the photosystems was performed essentially as described in Noren *et al.* [16] Frozen cells, equivalent to about 20 - 25 mg Chl, were thawed quickly and diluted with break buffer into a 250 mL centrifuge bottle. Cells were pelleted by centrifugation at 10,000 x g for 10 min, resuspended in a small volume of break buffer and transferred to the bead-beater chamber. Solubilization of thylakoid membranes and anion-exchange chromatography were carried out as

described[16] except that fractions from the Q-Sepharose Fast Flow column which were enriched in PSI (λ_{max} > 679 nm) were pooled and precipitated by the addition of an equal volume of 30 % (w/v) PEG- 8000 in 50 mM MES, pH 6.0. After mixing, the preparation was incubated overnight in the refrigerator and the resulting precipitate was recovered by centrifugation at 20,000 x g for 10 min. The pellet was redissolved in Mono-Q start buffer and the solution was chromatographed on the Mono-Q column. Fractions enriched in PSI were pooled and an equal volume of 30 % PEG-8000 was added followed by centrifugation at 40,000 x g for 30 min. The supernatant was removed completely and the pellet was resuspended in 50 mM HEPES pH 7.5, 15 mM NaCl,, 0.05 % dodecyl maltoside) to a final concentration of > 3 mg Chl/mL. The sample was then transferred to a 4 mm O.D.quartz EPR tube and stored in liquid nitrogen until further use. P_{700}^{+} was generated by illumination at 273 K for 30 seconds. The radical was trapped by freezing immediately to 77 K. The radical's presence, in both natural abundance ^{14}N and isotopically enriched ^{15}N samples, was confirmed by cw-EPR (see Figure 4-1).

Spectroscopy and Spectral Simulations

Continuous Wave EPR: The cw-EPR data were obtained (10 K) at X-band on a Bruker ER200D EPR spectrometer outfitted with a Bruker TE102 EPR cavity and an Oxford ESR-900 continuous flow cryostat. Microwave frequency was determined by using an EIP Microwave Model 25B frequency counter and the static magnetic field strength was measured with a Bruker ER035N NMR gaussmeter.

ENDOR spectroscopy and data analysis: The ENDOR data were obtained at X-band on a Bruker ESP300e spectrometer with a Bruker ESP360 DS ENDOR accessory and home-built demountable coils.[17] All ENDOR data were collected at a field position corresponding to the center of the EPR absorption line. Constant temperature in the cavity was maintained with an Oxford ESR900 continuous flow cryostat. Microwave frequency was determined by using an EIP Microwave Model 25B frequency counter and the static magnetic field strength was measured with a Bruker ER035M NMR gaussmeter

The peaks attributed to ^{15}N (I=1/2) electron nuclear hyperfine coupling are expected to be split symmetrically about the nuclear Larmor frequency for ^{15}N (ν_{15N} = 1.45 MHz at 3500 G). In solution ENDOR, the position of these peaks is indicative of the strength of the isotropic hyperfine coupling according to the relationship

$$\nu_{\pm} = \nu_N \pm A_{iso}/2$$

where $\nu_N \geq A_{iso}/2$. However, in frozen solution, the anisotropy of the hyperfine coupling gives rise to powder lineshapes described by to first order by

$$\nu_{\pm} = \nu_N \pm A/2$$

$$\text{where } A = A_{\|} \cos^2\theta + A_{\perp} \sin^2\theta$$

$A_{\|}$ and $A_{\perp}$ in the above expression are the principal values of the axially symmetric hyperfine tensor and θ describes the orientation of the principal axis system of the hyperfine tensor with respect to the laboratory magnetic field.

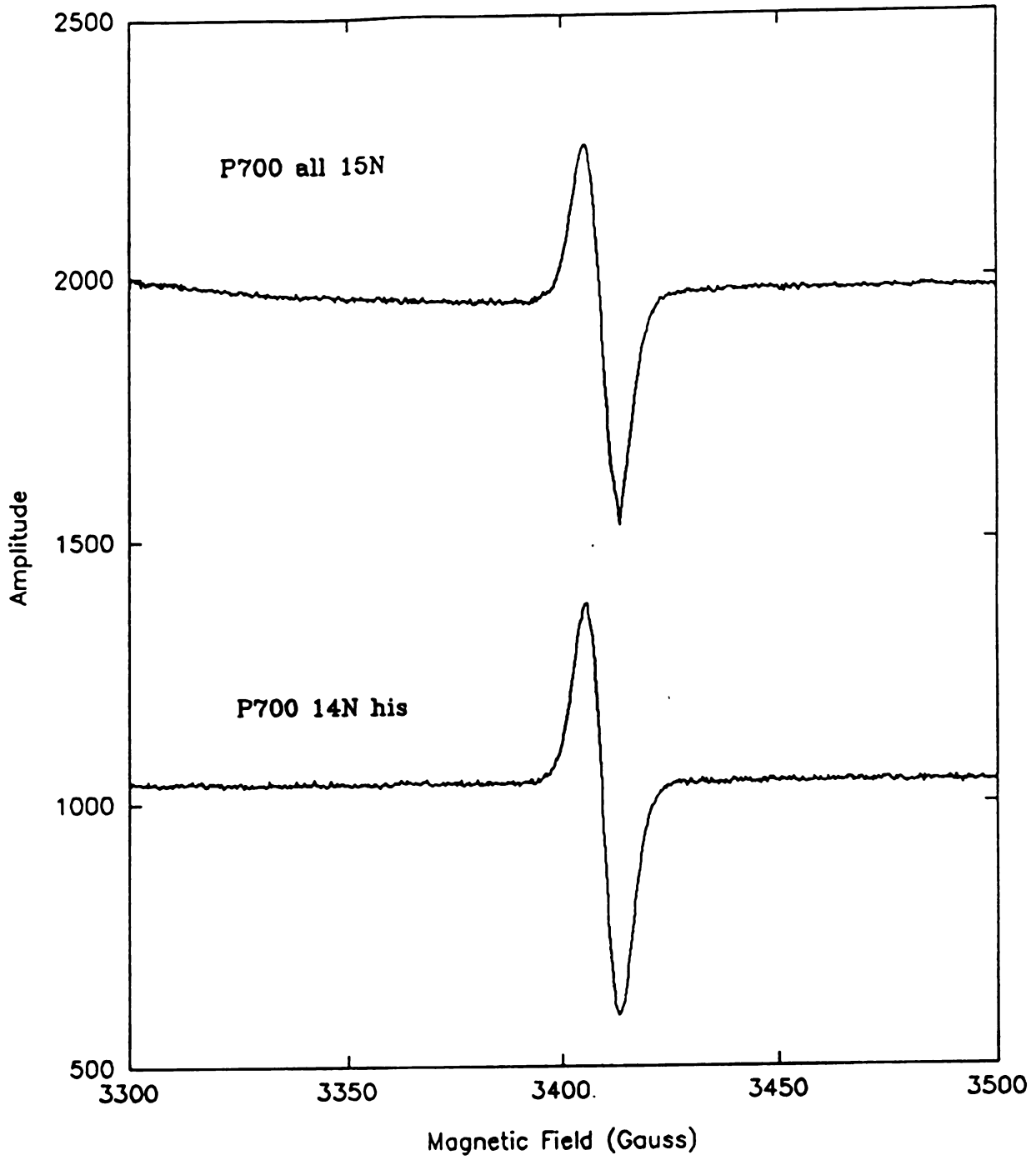

Figure 4-1: EPR spectra of P_{700}^{+} containing natural abundance ^{14}N (top) and isotopically enriched with ^{15}N. Spectrometer conditions: microwave power, 20 dB; center field, 3380 G; modulation amplitude, 20 Gpp; modulation frequency, 100 kHz; time constant, 200 ms; sweep time, 200 s; sample temperature, 8 K.

ESEEM data collection and analysis: ESEEM data were collected on a home built spectrometer[18] by using a reflection cavity where either folded stripline[19] or slotted-tube structures[20] served as the resonant element. A three pulse or stimulated echo (90°-τ-90°-T-90°) pulse sequence was used. Dead time reconstruction was performed prior to Fourier transformation as described.[21] Computer simulations of the ESEEM data were performed on a Sun Sparcstation 2 computer utilizing FORTRAN software based on the density matrix formalism of Mims.[22] The analysis software for the treatment of experimental and simulated ESEEM data was written with Matlab (Mathworks, Nantick, MA). The experimental dead time was included in the simulations. An isotropic g-tensor was assumed in all of the calculations. The success of the spectral simulations was based on the modulation depth and duration observed in the time domain traces as well as the lineshapes, peak positions and relative peak intensities in the frequency spectra.

Results

The continuous wave EPR spectra from P_{700}^{+} containing natural abundance ^{14}N (top) and isotopically enriched with ^{15}N (bottom) are shown in Figure 4-1. The spectra are indistinguishable from one another; both exhibit the characteristic lineshape of a chlorophyll π cation radical species. The spectra consist of a single peak centered at g=2.0025 with a linewidth of 7-7.5 G with no observable fine structure. ESEEM spectroscopy was used to resolve the small hyperfine couplings not observed in this inhomogeneously broadened line. The data were collected at magnetic field positions

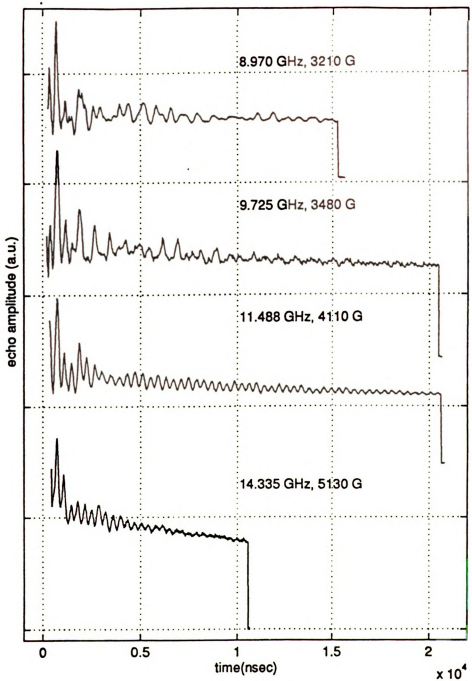

Figure 4-2: Multifrequency stimulated echo ESEEM time domain decay traces from P_{700}^{+} containing natural abundance ^{14}N. Spectrometer conditions: magnetic field strength, as noted; tau value, A) 250 ns, B) 162 ns, C) 300 ns, D) 400 ns; microwave pulse power, A) 45 dBm, B) 49 dBm, C) 55 dBm, D) 60 dBm; pulse repetition rate, A) 20 Hz, B) 60 Hz, C) 30 Hz, D) 60 Hz; pulse width (FWHM), 22 ns; sample temperature, 4.2 K.

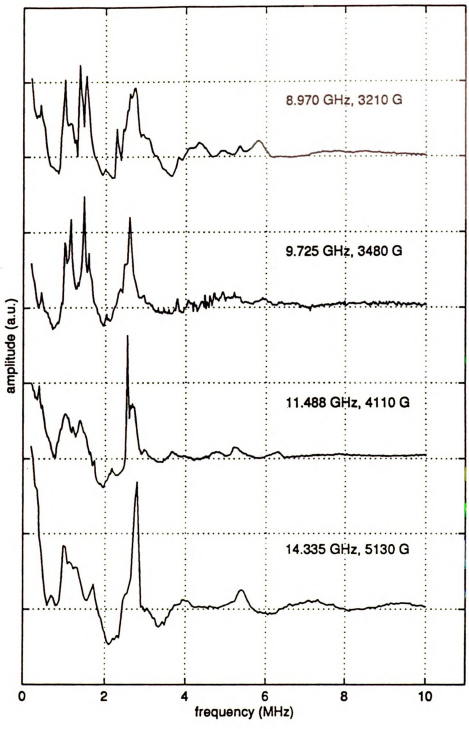

Figure 4-3: Cosine Fourier transformations of three-pulse ESEEM time domain traces at multiple microwave frequencies. Spectrometer conditions: as in Figure 4-2.

corresponding to the zero-field crossing on the EPR spectrum. Typical stimulated echo ESEEM patterns for P_{700}^{+} containing natural abundance ^{14}N and their corresponding Fourier transforms are shown in Figures 4-2 and 4-3, respectively.

The spectra in Figure 4-3 are dominated by the quadrupole coupling of the ^{14}N nucleus (I = 1). If the hyperfine interaction is approximately equal to twice the nuclear Zeeman frequency, then the energy level splittings in the spin manifold where these two cancel is determined primarily by the ^{14}N nuclear quadrupole interaction (see Chapter 2 for a detailed description of this interaction). To determine the field position at which this exact cancellation condition is met, it is essential that the experiment be performed at multiple microwave frequencies. The exact cancellation ESEEM pattern is characterized by modulations that are deep and long-lived, while the corresponding Fourier transformed spectrum exhibits three sharp, low frequency features (two of which add up to the third); these correspond to the zero field nuclear quadrupole transitions ($\nu_{\pm}$ and ν_0). If the exact cancellation condition is met, then the quadrupole parameters, the quadrupole coupling constant e^2qQ and the asymmetry parameter, η, which measure the magnitude and the symmetry of the electric field gradient tensor, may be calculated directly from the experimental ESEEM spectrum where

$$\nu_{\pm} = 3/4\ e^2qQ\ (1 \pm \eta/3)$$

$$\nu_0 = 1/2\ e^2qQ\ \eta.$$

The presence of a broad $\Delta M_I = 2$ or "double quantum" transition arising from the spin manifold where the nuclear Zeeman term is doubled by the hyperfine coupling, observed at approximately four times the nuclear Zeeman frequency is also indicative of this exact

cancellation condition, although the lineshape of this double quantum peak depends heavily on the amount of state mixing that is induced by the hyperfine coupling term of the Hamiltonian and also by the relative orientation of the NQI tensor with the PAS. The approximate peak position of the double quantum transition as well as the isotropic hyperfine coupling can be determined, in the exact cancellation limit, by using

$$\nu_{DQ} = 2\sqrt{\left(\nu_n \pm |A|/2\right)^2 + \xi^2} \quad \text{where} \quad \xi = \kappa\sqrt{3+\eta^2}$$

However, since both the isotropic and anisotropic part of the hyperfine coupling contribute to the A value in this expression, a large amount of dipolar coupling can make it difficult to determine A_{iso} directly from the position of the double quantum peak.

Figure 4-3B shows qualitatively that this exact cancellation condition is realized for at least two sets of nitrogen nuclei at a magnetic field strength of 3480 G. This spectrum contains five major low frequency components at 1.04, 1.15, 1.47, 1.60 and 2.60 MHz. From the positions of these peaks and by using the equations above, the nuclear quadrupole parameters can be determined for two sets of nitrogens; set A) e^2qQ = 2.70 MHz, η = 0.85 and set B) e^2qQ = 2.81 and η = 0.73.

Because the hyperfine contributions to the spectra in Figure 4-3 are obscured by the dominant quadrupole interaction, the reaction centers were isotopically enriched with ^{15}N (I = 1/2). The ^{15}N nucleus has no quadrupole moment and, therefore, the stimulated echo modulation pattern is determined primarily by the hyperfine interaction. The multifrequency stimulated echo ESEEM pattern and Fourier transforms of P_{700}^+ enriched with ^{15}N are shown in Figures 4-4 and 4-5, respectively. The modulations present in Figure 4-4 arise as a result of hyperfine coupling between the unpaired π electron and

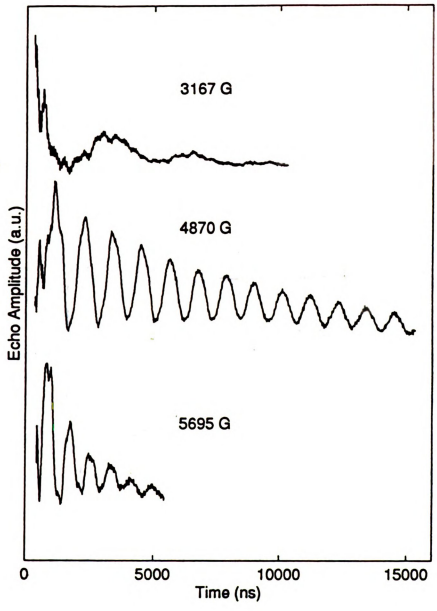

Figure 4-4: Multifrequency stimulated echo ESEEM time domain decay traces from P_{700}^{+} isotopically enriched with ^{15}N. Spectrometer conditions: magnetic field strength, as noted; tau value, A) 222 ns, B) 318 ns, C) 400 ns; microwave pulse power, A) 45 dBm, B) 45 dBm, C) 57 dBm; pulse repetition rate, A) 90 Hz, B) 30 Hz, C) 30 Hz; pulse width (FWHM), 22 ns; sample temperature, 4.2K.

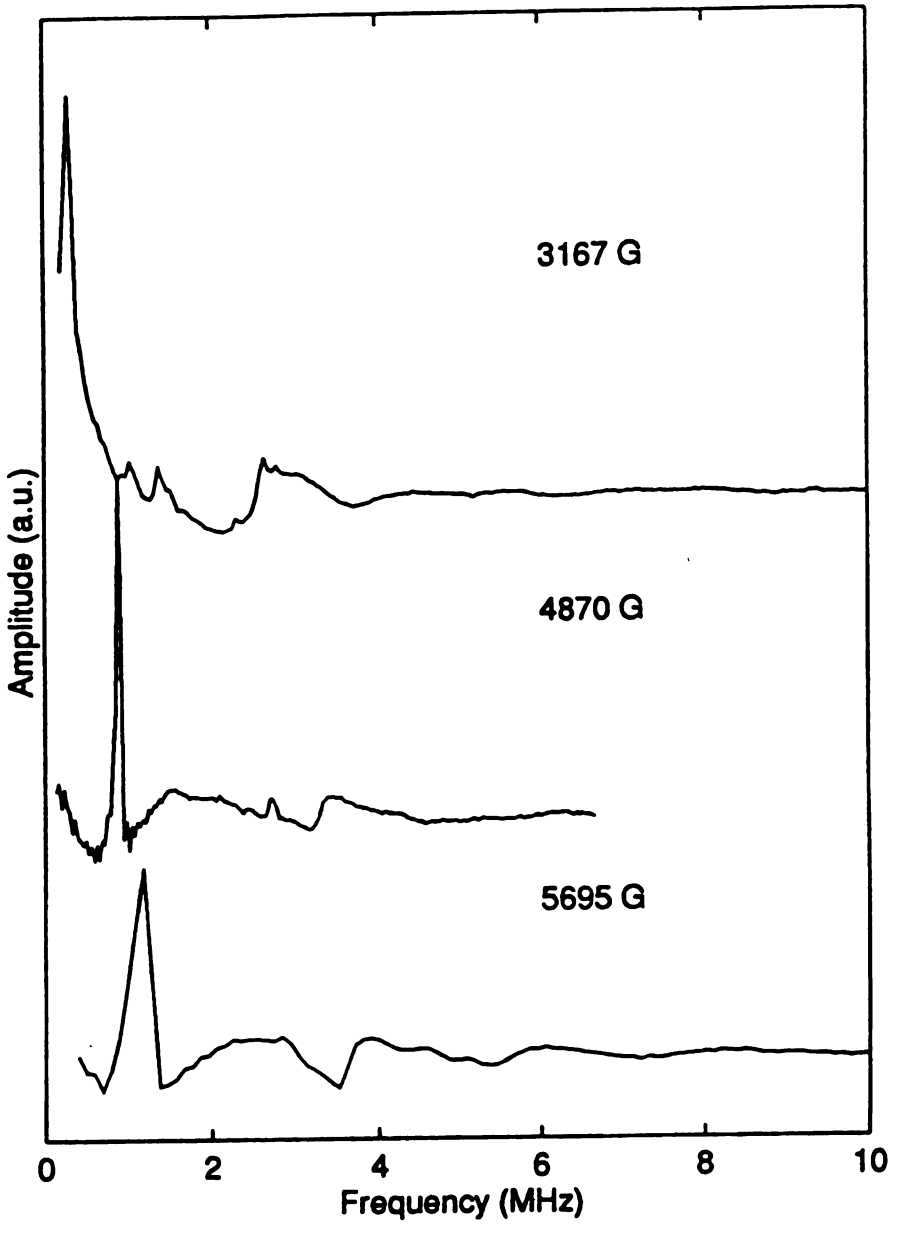

Figure 4-5: Cosine Fourier transformations of three pulse ESEEM time domain traces at multiple microwave frequencies. Spectrometer conditions: as in Figure 4-4.

nitrogen nuclei in the chlorophyll macrocycle. The increase in modulation depth evident at 4280 G (Figure 4-4, middle) is indicative of a situation where the hyperfine interaction is equal to twice the nuclear Zeeman frequency. At this "exact cancellation" like condition the modulation depth parameter, k (see Chapter 2) is maximized. The Fourier transform of this time domain decay trace (Figure 4-5, middle), unfortunately only exhibits two features: a large, sharp feature at 1 MHz and a broader feature near 4 MHz. The lack of spectral resolution in this, and all of the spectra from the ^{15}N enriched samples, precludes definitive determination of the hyperfine coupling constants and number of nuclei giving rise to the observed peaks.

Assignments may be achieved, however, by performing spectral simulations of the experimental data. The success of these simulations depends on the validity of both the magnitude of the nitrogen hyperfine and quadrupole coupling constants as well as the number of nuclei giving rise to a particular coupling. To make unambiguous assignments of nitrogen hyperfine coupling constants for P_{700}^{+}, the nitrogen hyperfine coupling tensors and nuclear quadrupole parameters determined must simulate successfully *all* of the ESEEM spectra in Figures 4-3 and 4-5.

Because the observed modulations may arise from as many as eight interacting nitrogen nuclei, with each nitrogen requiring eight independent simulation parameters, determination of the simulation parameters is severely underdetermined. To assist in the assignment of ESEEM features and provide constraints for the simulations, ENDOR experiments were performed on the ^{15}N enriched P_{700}^{+} sample, see Figure 4-6. Features in the low (1-5 MHz) frequency region of this spectrum are expected to arise from ^{15}N

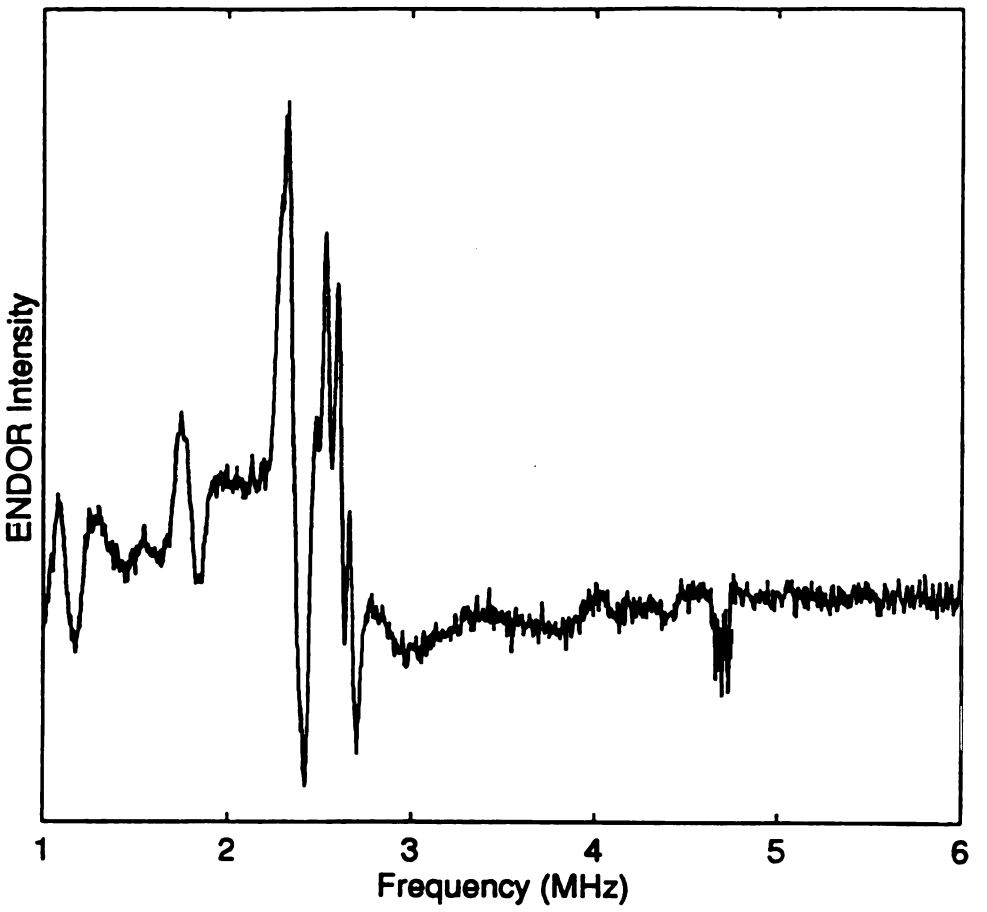

Figure 4-6: ENDOR spectrum collected at 6 K for P_{700}^{+} globally labeled with ^{15}N. Spectrometer conditions: microwave power, 1.99 mW; magnetic field strength, 3375 G; RF power, 200 W; RF frequency modulation: 100 kHz.

nuclei coupled to the π electron in P_{700}^-. Peaks at 1.12 and 1.78 MHz, which are split symmetrically about the nuclear Larmor frequency for ^{15}N (1.46 MHz at 3375 G), have been assigned to the magnetic coupling between P_{700}^- and an axial histidine ligand (see Chapter 3).

The features in the 2-3 MHz region are assigned to hyperfine interactions between P_{700}^+ and the pyrrole nitrogens in the chlorophyll macrocycle. This assignment is based on the fact that these peaks disappear when the sample is specifically labeled with ^{15}N histidine (see Figure 3-3, middle); in this sample, all other nitrogens, except those in histidine, are ^{14}N and, because of their large quadrupole moments, do not contribute to the ENDOR spectrum. The peaks in the 2-3 MHz region represent the perpendicular components of the hyperfine coupling in one spin manifold. The corresponding transitions from the other manifold, expected to be split symmetrically about ν_n for ^{15}N, occur at frequencies near zero and, therefore, are not resolved in this experiment. It is possible, however, to make some predictions on the strength of the hyperfine coupling based on the peak positions and lineshapes. For example, if the derivative shaped feature at 2.35 MHz, can be assigned to the perpendicular singularity of a nitrogen hyperfine tensor, then a corresponding $A_\perp$ value of 1.78 MHz is obtained. Because the number of orientations that contribute to the perpendicular singularity is larger than the number contributing to the parallel component, resolution of the corresponding $A_\parallel$ feature is often difficult with ENDOR.

The ESEEM data can be used, in this case, to provide some insight into the magnitude of the $A_\parallel$ coupling expected. At exact cancellation, the hyperfine coupling is

equal to twice the nuclear Larmor frequency. Figure 4-2 shows that this condition is realized at a magnetic field of 3480 G, where the nuclear Larmor frequency is 1.07 MHz. The hyperfine coupling corresponding to this is 2.14 MHz, which, when scaled to both the ^{15}N nucleus ($^{15}N/^{14}N$ = 1.403) and to the magnetic field strength at which the experiment was performed, yields an isotropic coupling of 2.90 MHz. Model chlorophyll and bacteriochlorophyll compounds have shown that the hyperfine tensor for the pyrrole nitrogens is of axial symmetry[23], therefore, by using the relations

$$A_{\parallel} = A_{iso} + 2f$$

$$A_{\perp} = A_{iso} - f$$

and

$$\nu_{observed} = \left| \nu_I \pm \frac{A}{2} \right|$$

where f is the dipolar contribution to the hyperfine coupling, and ν_I is the nuclear Larmor frequency, the peak positions of the $A_{\parallel}$ singularity can be determined. An isotropic hyperfine coupling of 2.90 MHz would therefore yield a peak in the 4 MHz region of the spectrum. There is a small absorptive feature in this region, which is assigned to the $A_{\parallel}$ turning point of one nitrogen hyperfine coupling.

The improved resolution of this ENDOR spectrum can be used to assist in constraining the parameters needed to perform the numerical simulations of the ESEEM data. Three additional $A_{\perp}$ features can be measured from the positions of the peaks in the ENDOR spectrum. These couplings, with magnitudes of 2.14, 2.30 and 2.42 MHz, scaled to the ^{14}N nucleus and included with the two sets of quadrupole parameters determined from Figure 4-3B provide a starting point for the simulations.

The lack of features in the double quantum region of the ESEEM spectrum also provides insight into the magnitude of the dipolar contribution to the total nitrogen hyperfine coupling. Increased state mixing induced by the presence of significant anisotropy in the hyperfine term of the spin Hamiltonian affects the transition probabilities in the spin manifold from which the double quantum feature originates. Because the energy levels are quantum mechanical mixtures of eigenstates, all transitions have a non-zero probability of occurring and because they all occur, for ^{14}N, near 4 MHz, can result in a loss of resolution in this region. This effect is exhibited in Figure 4-7. Each calculated ESEEM spectrum in this figure has the same isotropic hyperfine coupling; the dipolar contribution to the total hyperfine coupling in each case, however, is different. The effect on the features in the double quantum region as the anisotropy increases is pronounced as is the effect on the linewidth of the low frequency components. Because the double quantum peaks are missing from the ESEEM spectrum collected at 3480 G, a considerable amount of anisotropy must be present in the hyperfine coupling of at least one nitrogen.

Further insight into the form of the hyperfine and quadrupole tensor can be gained by examination of the ESEEM spectrum collected at 4110 G (see Figures 4-2C and 4-3C). The depth and duration of the modulations observed in the time domain trace are indicative of an exact cancellation condition for at least one nitrogen nucleus. The presence of only two sharp, intense low frequency peaks in the corresponding Fourier transform, however, does not confirm this hypothesis. The presence of two, rather than three, peaks can be explained by examining the asymmetry parameter, η. This parameter

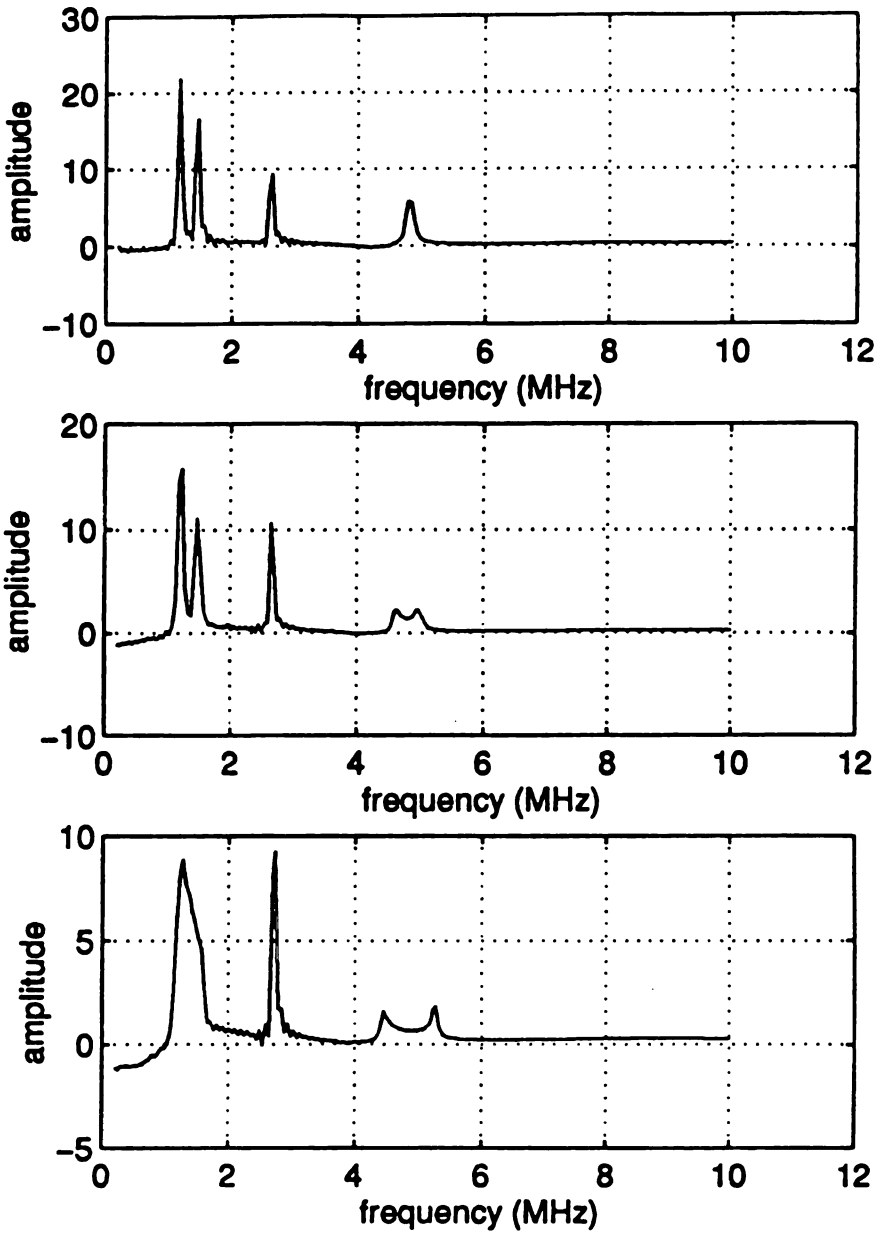

Figure 4-7: The effect of hyperfine anisotropy on the ESEEM spectrum. Simulation conditions for all spectra unless otherwise noted: $A_{\perp}$: 1.84 MHz (top), 1.64 MHz (middle), 1.44 MHz (bottom); $A_{\parallel}$: 2.17 MHz (top), 2.56 MHz (middle), 2.97 MHz (bottom); A_{iso}: 1.95 MHz; e^2qQ: 2.69 MHz; η: 0.87; magnetic field strength: 3480 G; tau value: 162 ns; Euler angles (α, β, γ): 0,0,0.

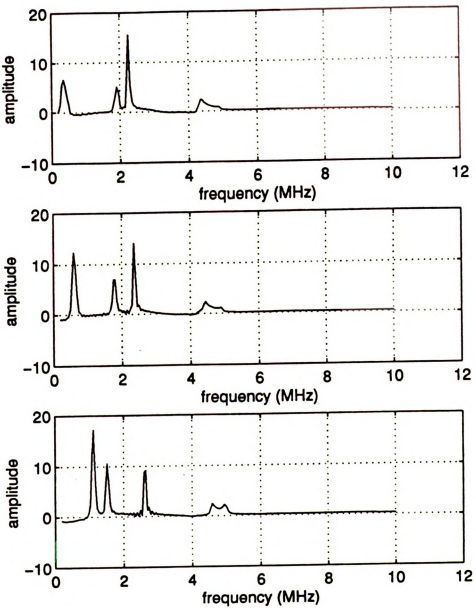

Figure 4-8: The effect of the asymmetry parameter on the ESEEM spectrum. Simulation conditions for all spectra unless otherwise noted: $A_{\perp}$: 1.64 MHz; $A_{\parallel}$: 2.56 MHz; A_{iso}: 1.95 MHz; e^2qQ: 2.69 MHz; η: 0.2 (top), 0.4 (middle), 0.8 (bottom); magnetic field strength: 3480 G; tau value: 162 ns; Euler angles (α, β, γ): 0,0,0.

describes the deviation from axial symmetry of the electric field gradient originating from the electrons in the p orbitals. An asymmetry parameter of 1 describes a system with rhombic symmetry, while a value of zero for η is indicative of axial symmetry. The magnitude of this parameter affects the position of the low frequency peaks in the ESEEM spectrum. These effects are shown in Figure 4-8. When η is small (Figure 4-8. top) the two lowest frequency peaks coalesce into a single feature. This is most likely the situation observed for the ESEEM spectrum collected at 4110 G and information regarding the magnitude of this asymmetry parameter can be utilized in the parameter set for at least one nitrogen.

Table 4-1: ^{14}N ESEEM simulation parameters.

	$A_\perp$ (MHz)	$A_\parallel$ (MHz)	A_{iso} (MHz)	e^2qQ (MHz)	η	α	β	γ
N_I	1.27	3.66	2.06	3.1	0.20	0	0	0
N_{II}	1.55	3.29	2.13	2.69	0.87	0	90	0
N_{III}	1.64	2.56	1.95	2.69	0.87	0	90	0
N_{IV}	1.73	3.10	2.19	2.81	0.70	0	0	0

The sharp features present in the spectrum collected at 4110 G were also found to be dependent upon the relative orientation of the hyperfine and quadrupole axis systems. By performing iterative simulations utilizing various angle combinations and subsequent qualitative analysis of the spectral features as a function of the Euler angles describing

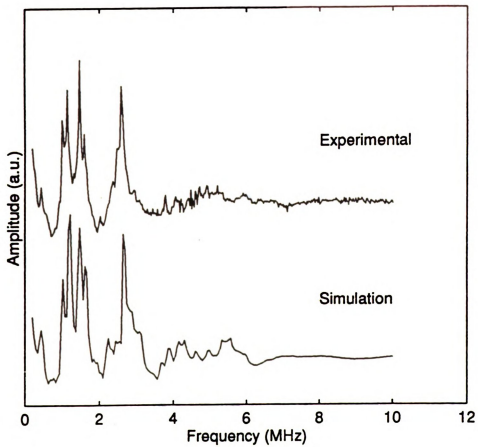

Figure 4-9: Experimental (top) stimulated echo ESEEM spectrum from P_{700}^{+} containing natural abundance ^{14}N and corresponding numerical simulation (bottom). Experimental conditions: as in Figure 4-3B. Simulation parameters: As in Table 4-1; additional parameters as in experimental.

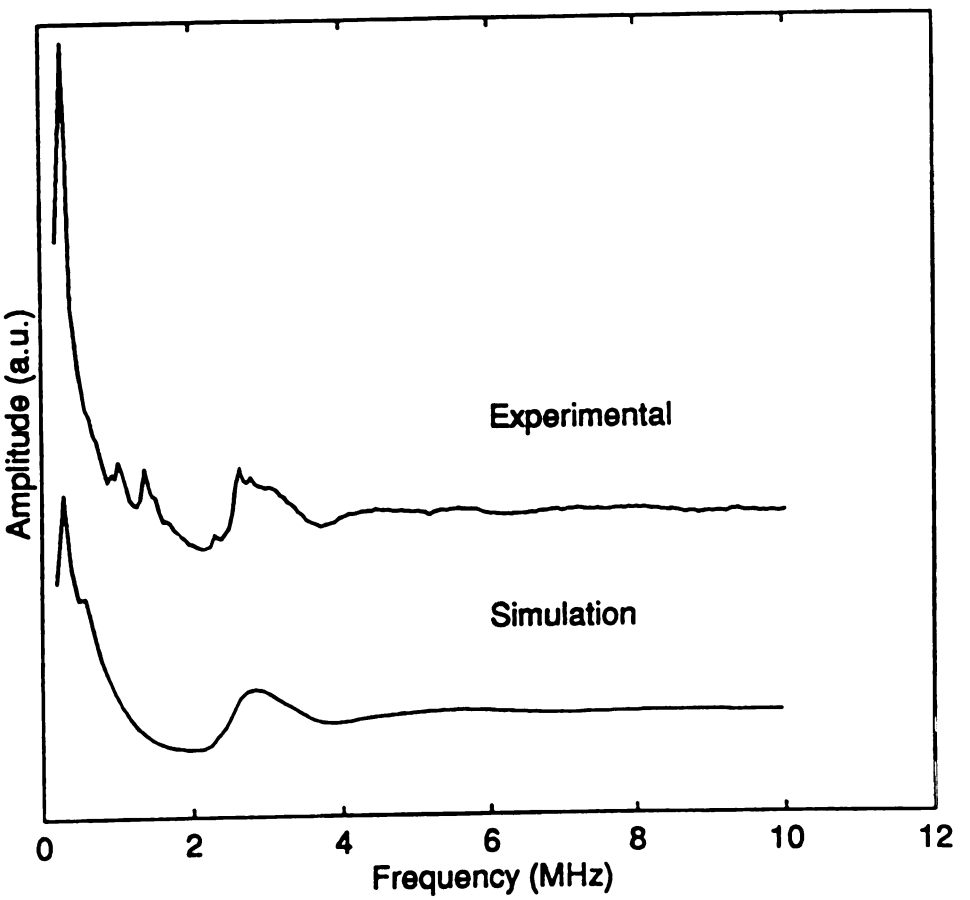

Figure 4-10: Experimental (top) stimulated echo ESEEM spectrum from P_{700}^{+} isotopically enriched with ^{15}N and corresponding numerical simulation (bottom). Experimental conditions: as in Figure 4-5B. Simulation parameters: As in Table 4-2; additional parameters as in experimental.

this orientation, it was found that this lineshape was present only when the two axes were collinear.

By utilizing these experimental constraints, successful numerical simulations of the ESEEM data for both nuclei at multiple microwave frequencies was possible. Figures 4-9 and 4-10 present the simulations and experimental data for P_{700}^- containing natural abundance ^{14}N (collected at 3480 G) and isotopically enriched with ^{15}N (collected at 3167 G). The parameter sets for these simulations are tabulated (see Tables 4-1 and 4-2). There is very good agreement between these simulations and the experimental spectra.

Table 4-2: ^{15}N ESEEM simulation parameters.

	$A_\perp$ (MHz)	$A_\parallel$ (MHz)	A_{iso} (MHz)	r (Å)
N_I	1.78	5.13	2.89	1.93
N_{II}	2.17	4.62	2.99	2.13
N_{III}	2.30	2.67	2.73	2.65
N_{IV}	2.43	4.35	3.07	2.32

The peaks in the experimental spectrum from ^{15}N enriched P_{700}^+ that are not reproduced in the simulation are the result of residual ^{14}N contamination. Mass spectrometry of the ^{15}N enriched P_{700}^+ sample confirms the presence of this ^{14}N (see Figure 4-11). Because the modulations originating from the ^{14}N quadrupolar interactions are so strong, even residual

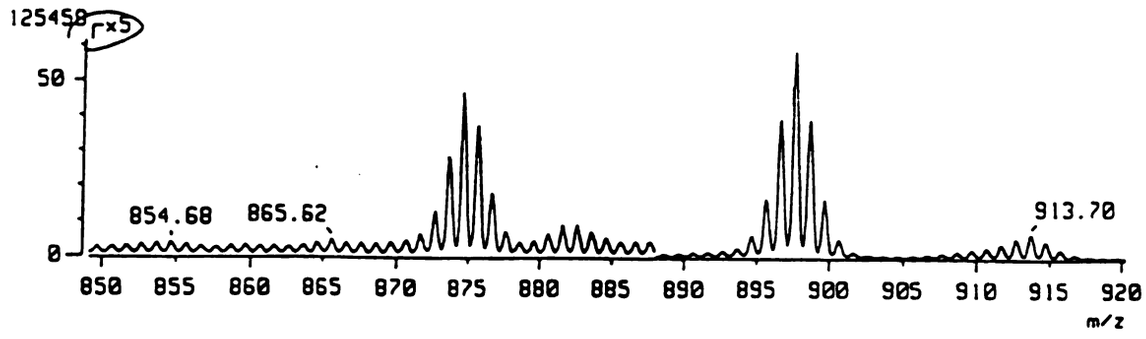

Figure 4-11: FAB-MS data on chlorophyll a extracted from PSI isotopically enriched with ^{15}N. Peaks at 896.65 and 873.68 indicate the presence of residual ^{14}N.

amounts of the nucleus can be observed in the ESEEM spectrum and, moreover, the positions of these features in the ^{15}N spectrum corresponds to the observed frequencies of the peaks in the ^{14}N spectrum (Figure 4-3B). In the absence of the mass spec data, these features, which appear in the same low frequency region of the spectrum as those arising from ^{15}N, may have been erroneously assigned to ^{15}N resonances.

Multifrequency simulations utilizing the parameter sets in Table 4-1 are shown in Figure 4-12. The agreement between these calculated spectra and the experimental data shown in Figure 4-3 is consistent at every field value. These multifrequency experiments and corresponding simulations are necessary for determination of the complete hyperfine and quadrupole parameter sets that contribute to the ESEEM modulation pattern.

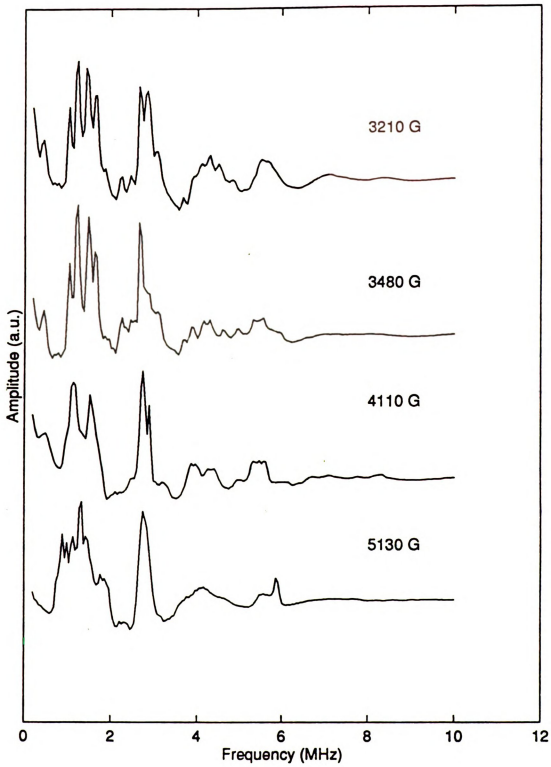

Figure 4-12: Numerical simulations of multifrequency ESEEM spectra from P_{700}^{+} containing natural abundance ^{14}N. Simulation parameters: as in Table 4-1; all other parameters as in experiment (see Figure 4-3A-D).

Discussion

The combination of isotopic substitution, ENDOR, multifrequency ESEEM and numerical simulations of ESEEM data utilized in this study presents a methodology that can be used to determine definitively the magnetic properties of radicals in protein systems. Although early ESEEM and ENDOR investigations of chlorophyll a model compounds and P_{700} containing natural abundance ^{14}N or isotopically enriched with ^{15}N were able to identify the limits for these properties[24], the combination of these spectroscopies with isotopic substitution was not enough to determine definitively the hyperfine and quadrupole tensors for all of the nitrogens contributing to the spectra observed and currently, the ambiguity surrounding the electronic structure of the primary donor remains.

The utility of ENDOR spectroscopy as a method to study hyperfine couplings with little or no anisotropy has been previously demonstrated (see Chapter 3). It's applicability to systems containing large isotropic proton couplings has been demonstrated extensively in the biophysics field.[25] However, in systems characterized by small hyperfine couplings with a large dipolar contribution and containing nuclei with low gyromagnetic ratios (e.g. ^{14}N or ^{15}N), useful spectral information is lost because the low frequency transitions occur near zero and are not resolved with most commercial spectrometers. Likewise, the turning points of the broad powder pattern lineshape that results from a large dipolar interaction can be difficult to resolve experimentally, as only the large perpendicular component is detected. Additionally, because of second order effects, the detection of couplings to quadrupolar nuclei is difficult and results in line

broadening that decreases resolution. Again, isotopic substitution with ^{15}N can be utilized to remove the quadrupolar contribution, however the low frequency resolution problem remains as the gyromagnetic ratio of ^{15}N differs only slightly from that of ^{14}N.

ESEEM spectroscopy circumvents these problems. The exact cancellation condition, usually realized for nitrogen nuclei near 3300 G, allows determination of the pure quadrupole resonances while the hyperfine interactions can be discerned by using isotopic substitutution with ^{15}N, which eliminates the quadrupole contribution. Furthermore, the physical requirement for bandwidth sufficient to excite all transitions simultaneously means that detection of small couplings to nuclei with low gyromagnetic ratios is possible. This technique is also ideal for measuring hyperfine couplings containing a large dipolar contribution, since the nuclear modulation effect depends on the quantum mechanical mixing of states that occurs as a result of the anisotropic interaction. Moreover, since all coupled nuclei contribute, in a multiplicative manner, to the modulation pattern observed in an ESEEM experiment, quantitation of the number of interacting species based on peak intensities is possible. The intensities of the peaks observed in ENDOR, because they are governed by competing relaxation times, yield no qualitative information about the number of species contributing.

Analysis of the peaks observed in the ESEEM spectrum, however, can be difficult as the number of combination peaks arising from multiple nuclei precludes the definitive assignment of these features. This is especially apparent in the primary donor systems of both plants and bacteria. In these systems, nitrogen couplings are expected from a minimum of 4 (monomer) and a maximum of 8 (dimer) pyrrole nitrogens. Additional couplings from axial nitrogenous ligands are possible as well, although couplings from

the axial histidine ligand to P_{700}^{+} have been shown not to contribute to the ESEEM modulation pattern (see Chapter 3). The presence of multiple interacting nuclei with similar magnetic properties results in the presence of multiple combination lines in the ESEEM spectrum. Moreover, these peaks appear in the 1-5 MHz region of the spectrum. Definitive assignment of peaks to specific nitrogen nuclei is therefore impossible without reliable spectral simulations.

Numerical simulations of experimental ESEEM data can be misleading as well since the number of independent parameters required for a system like P_{700}^{+}, which contains multiple quadrupolar nuclei, severely underdetermines the calculation. To constrain the calculation, information regarding the magnitude of these parameters can be obtained from study of model compounds, examination of the literature or from theoretical calculations modeling the species *in vivo* and *in vitro*. Constraints can also be provided by experimental results from other spectroscopic methods or by using isotopic substitution to eliminate specific contributions.

A combination of these methods has been used to constrain the parameter sets in this study. Perhaps one of the most useful of these constraints was the ability to obtain results from ESEEM experiments performed at multiple microwave frequencies. Since the peak position will change as a function of the Larmor frequency of the nucleus from which the resonance arises, which is dependent on the external magnetic field strength, this method can be used to make definitive assignments.

Multiple frequency ESEEM can also be used to find the exact cancellation condition for systems with quadrupolar nuclei. Because the Larmor frequency is a function of the applied magnetic field strength, an exact match between the hyperfine

coupling, which is constant for the system, can only be determined by changing the magnitude of the external magnetic field. In the case of P_{700}^{+}, the ability to perform multiple frequency experiments proved to be extremely advantageous since an additional set of quadrupole parameters was discovered at 11 GHz that was not observed at the lower microwave frequecies.

Analysis and Interpretation of Nuclear Quadrupole Interactions in P_{700}^{+}

Because the peaks observed in the exact cancellation ESEEM spectrum from P_{700}^{+} represent the zero field transitions of ^{14}N nuclei in the chlorophyll, the nuclear quadrupole coupling constant, e^2qQ and the asymmetry parameter, η, can be determined directly from the experimental spectrum. The quadrupole coupling constants and asymmetry parameters for the pyrrole nitrogens in P_{700}^{+} as determined from multifrequency ESEEM experiments are listed in Table 4-1. The magnitudes of the quadrupole coupling constants determined for P_{700}^{+} are consistent with those determined for chlorophyll and bacteriochlorophyll species studied *in vivo* and *in vitro* (see Table 4-3). The values determined for the asymmetry parameters for three of the pyrrole nitrogens are somewhat larger than those found for Chl a^{+}. Because this parameter can be dramatically affected by small fluctuations in the orbital occupancies, local electron density distribution differences due to interactions with the protein may significantly alter this parameter.[26] The asymmetry parameter for N_I (see Table 4-1) is consistent with the value obtained for Chl a^{+}, indicating that the environment of this nitrogen differs somewhat from the other three. This hypothesis, and possible explanations for this will be discussed later in this

Table 4-3: Quadrupole parameters for chlorophyll and bacteriochlorophyll species *in vivo* and *in vitro*.

Species	e^2qQ (MHz)	η
$P_{870}^{+\ 27}$	2.73	0.66
P_{960}^{+27}	2.90	0.70
P_{860}^{+24}	1.68	0.68
	2.72	0.66
Chl a^{+14}	2.68	0.60
	3.20	0.50
BChl a^{+28}	2.72	0.70
	2.80	0.79

chapter. For the most part, though, the values for η obtained are mostly consistent with those previously measured for P_{700}^{+} Because e^2qQ and η describe the interactions of the electric quadrupole moment of the nucleus with local electric field gradients, knowledge regarding the magnitudes of these parameters is desirable and can yield information regarding the local electric field gradients due to interactions with charged amino acid residues as well as the charge concentration present in a covalent bond.

The model of Townes and Dailey,[29] which assumes that the electric field gradient at the nucleus is due only to electrons in the valence 2p orbitals, is a convenient approach for the interpretation of these parameters. The axis system in this model assumes that the Z axis lies along the largest component of the electric field gradient tensor. In a pyrrole compound, the molecular symmetry ensures that one field-gradient axis lies along the NH bond, one is perpendicular to the molecular plane and the third, in the molecular plane, is perpendicular to the other two.[30] The principle axis is almost always perpendicular to the molecular plane since the p_π orbital contains the lone-pair of electrons. In contrast, the Z

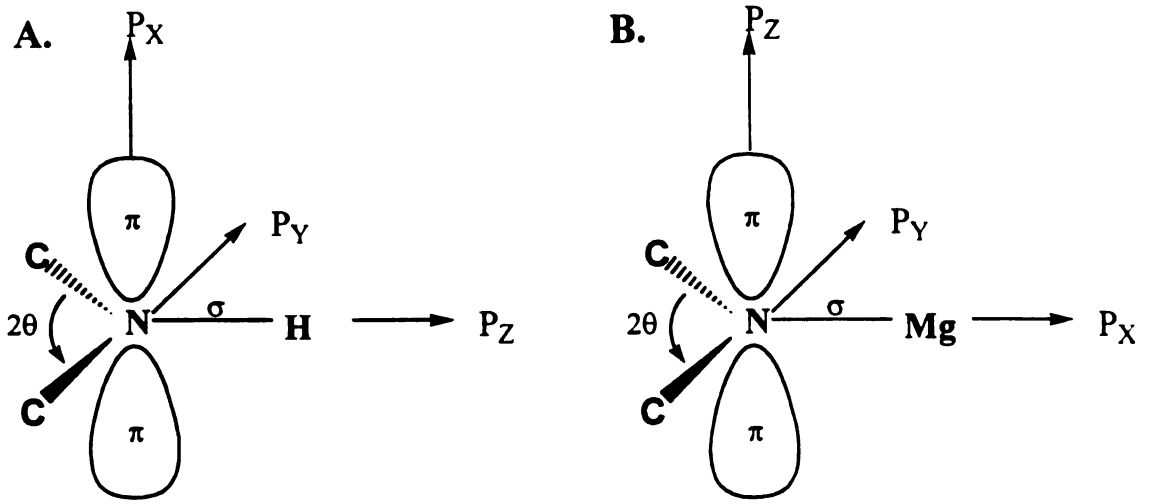

Figure 4-13: Quadrupole tensor axis systems for a) imino nitrogens in imidazole as compared to pyrrole (b) nitrogens.

axis for the imino nitrogen of imidazole has been found to lie in the plane and is only 4° off of the geometric z axis, defined as the bisector of the C-N-C angle (see Figure 4-13).[31]

Because the relative orientations of the nuclear quadrupole and hyperfine tensors can affect the lineshapes of the observed resonances, an Euler angle rotation relating the two coordinate systems was included in the simulations. The Z direction of the hyperfine tensor is usually taken as parallel to the p orbital containing the unpaired electron. For two of the pyrrole nitrogens in P_{700}^{+} the hyperfine and quadrupole axes were found to be collinear. The axes of the hyperfine and quadrupole tensors for the other two nitrogens were found to be related by an Euler angle rotation of $\beta=90°$ (see Euler angles, Table 4-1). This rotation is, most likely, the result of the asymmetrical distribution of the unpaired electron in the π molecular orbital and will be discussed in the following section.

Analysis and Interpretation of Hyperfine Interactions in P_{700}^{+}

A large body of work, both experimental and theoretical, has been dedicated to the determination of the magnitude of the hyperfine couplings for the pyrrole nitrogens in chlorophyll compounds both *in vivo* and *in vitro*.[32] Much of the early spectroscopic work was influenced by the single crystal magnetic resonance experiments performed on the bacterial reaction center. In this system, the primary electron donor consists of a dimer of bacteriochlorophyll a with the unpaired electron delocalized asymmetrically over the two halves of the dimer in a 2:1 ratio.[14] The electronic structure has been elucidated based on extensive ^{1}H ENDOR studies utilizing the available single crystals. The asymmetrical spin density distribution motif observed in these systems has been proposed for the primary donor in PSI.

A recent spectroscopic investigation of ^{15}N enriched P_{700}^{+} has estimated that the unpaired electron is 90% delocalized on a single chlorophyll a macrocycle; the other 10% of the spin is distributed over the other half of the geometric dimer.[15] This conclusion is based on the observation of small features in the ESEEM spectrum of ^{15}N labeled P_{700}^{+} that previously were not detected. These features correspond to a hyperfine coupling of 0.37 MHz and have been assigned to hyperfine couplings from the nitrogens on the *other* (10% spin) dimer half. Subsequent ENDOR and HYSCORE experiments indicated the presence of couplings of this magnitude. However, the presence of residual ^{14}N in these ^{15}N enriched samples, which has been shown to contribute to the ESEEM spectrum even at small concentrations, was not ruled out. The observed peaks, therefore, may result

from 14N contamination and not correspond to a hyperfine coupling to the 15N pyrrole nitrogens on the other half of the dimer.

Single crystal ESEEM studies by the same laboratory[15], which detected five sets of quadrupole couplings in P_{700}^{+} seem to corroborate these results, however, single crystal ESEEM studies are complicated by the presence of multiple combination peaks and unless couplings are confirmed by simulations and multiple microwave frequency experiments, do not provide definitive proof of these parameters.

The hyperfine and quadrupole coupling parameters listed in Tables 4-1 and 4-2, however, are the result of an exhaustive and comprehensive study incorporating samples containing either natural abundance ^{14}N or isotopically enriched with ^{15}N, followed by multifrequency ESEEM and ^{15}N ENDOR. The couplings extracted from these spectroscopic studies were confirmed by performing numerical simulations of the ESEEM data. Constraints for these calculations were provided by the multiple magnetic resonance experiments performed and, because simulations utilizing the *same* parameter set reproduced the experimental multifrequency ESEEM data for ***both*** isotopes, these data represent the first definitive assignments of hyperfine and quadrupole coupling constants to the pyrrole nitrogens in P_{700}^{+}.

The $A_{\perp}$ elements of the hyperfine tensors of P_{700}^{+} determined from ENDOR and the corresponding values concluded from simulations of the multifrequency three-pulse ESEEM spectra presented here are identical. The $A_{\parallel}$ components of these tensors were not resolved in the ENDOR and subsequently, the values utilized in the calculations were determined primarily through qualitative analysis of the numerical simulations. Limits

for these couplings, though, were provided through examination of the multifrequency stimulated echo ESEEM spectra. Isotropic hyperfine coupling constants, determined from exact cancellation stimulated echo ESEEM spectra, helped to place these limits. The use of axial tensors to model the hyperfine interaction of these nuclei is warranted since previous magnetic resonance studies of chlorophyll and bacteriochlorophyll model systems have yielded nitrogen hyperfine couplings of axial symmetry.[23] Furthermore, theoretical molecular orbital calculations with the RHF-INDO/SP (Restricted Hartree-Fock, Intermediate Neglect of Differential Overlap-Spin Polarization) method on chlorophyll a cation radicals yielded tensors varying only slightly from axial symmetry (see Table 4-4).[15] Corresponding calculations on the radical *in vivo* have not been presented in the literature. For comparison, the tensor components for P_{700}^{+} derived from experiment are included in this table.

These hyperfine couplings can be used to quantify the amount of spin density in the pp orbital of the individual nitrogen nuclei and therefore provide a probe into the electronic structure of the radical. A full characterization of this structure, however, should include spin density calculations for each nucleus in the species. Multiple ^{1}H ENDOR experiments[11] on frozen solutions of P_{700}^{+} have yielded coupling constants for various positions in the heterocycle. Based on the magnitude of these couplings and their corresponding spin densities, O'Malley and Babcock[11] proposed an electronic structure model for the radical whereby the unpaired electron is delocalized over a single macrocycle. The decreased proton hyperfine coupling constants and corresponding carbon spin densities observed for P_{700}^{+} *in vivo* relative to those of the chlorophyll a monomer model were attributed to differences in the composition of the ground state

Table 4-4: Experimental and theoretical hyperfine coupling tensor components for P_{700}^{+} and Chl a^{+}

	N_I	N_{II}	N_{III}	N_{IV}
RHF-INDO/SP* (Chl a^{+})				
A_{11}	1.90	1.11	0.96	0.88
A_{22}	1.97	1.28	1.06	0.98
A_{33}	4.83	3.01	2.31	2.31
A_{iso}	2.90	1.80	1.45	1.34
Experimental (P_{700}^{+})				
$A_{\perp}$	1.73	1.27	1.64	1.55
$A_{\|\|}$	3.10	3.66	2.56	3.29
A_{iso}	2.19	2.06	1.95	3.29

*converted from ^{15}N values.

orbital for the two systems. For P_{700}^{+}, a mixture of 25% of the first excited state and 75% of the ground state orbital was found to give good agreement between the *in vivo* and *in vitro* spin densities.

Analogous spin density calculations were performed for the nitrogen nuclei in P_{700}^{+}. Because the unpaired spin density on the nitrogens in these π-type radicals resides in the p orbital perpendicular to the plane of the three sp^2 hybrids, the spin density is determined by the magnitude of the dipolar part of the hyperfine coupling, f:[33]

$$A_{\perp} = A_{iso} - f$$
$$A_{\parallel} = A_{iso} + 2f$$

The amount of unpaired spin in this orbital can then be calculated by using a corrected form of the McConnell equation (see Chapter 2)

$$\rho_{\pi}^{N}(cor) = 1.042\, \rho_{\pi}^{N}(uncor)$$

where the correction factor accounts for the increased s character of the orbital containing the lone pair of electrons relative to the other sp^2 bonding orbitals.[33] The spin densities for the nitrogen nuclei in P_{700}^{+} as well as the dipolar part of the hyperfine coupling used in the calculation are shown in Table 4-5.

Table 4-5: Dipolar couplings and spin densities for pyrrole nitrogens in P_{700}^{+}

	N_I	N_{II}	N_{III}	N_{IV}
f (MHz)	0.79	0.58	0.31	0.46
spin density (corrected)	0.017	0.010	0.007	0.013

In the O'Malley and Babcock hybrid orbital model, the experimentally determined spin densities were compared to the spin densities calculated for the ground state molecular orbital for chlorophyll a^{+}.[34] These experimentally determined "reduction factors" were then compared to those of the theoretically derived hybrid orbital. The reduction factors for C1, C2a, C3, C4, C17, C18 and C_{α} derived experimentally were in excellent agreement with the theoretically predicted factors (see Table 4-6).

A similar approach was taken with the nitrogen spin densities determined from ESEEM and numerical simulations. As exhibited in Table 4-6, an excellent match between the experimental and theoretical reduction factors was obtained.

The presence of a hybrid orbital also explains the isotropic hyperfine coupling observed for the axial histidine ligand to P_{700}^{+} discussed in Chapter 3. Molecular orbital calculations predict that there is no localized unpaired spin density residing on the Mg^{2+} nucleus for an electron in the ground state a_{1u} molecular orbital (see Chapter 3).[34] The first excited state molecular orbital however, is expected to have considerable spin density at this site. Mixing 25% of this excited state orbital with the ground state orbital provides the spin density necessary to produce an observable hyperfine coupling to the nitrogen moiety of the axial ligand.

The presence of this axial histidine ligand in P_{700}^{+} also explains the admixing of the ground and excited state orbitals as it has been shown that the energy splitting between these orbitals can vary with axial ligation.[35] In the bacterial reaction centers, the presence of an axial histidine ligand, which has been confirmed by the high resolution crystal structure,[12,13] is not expected to catalyze this mixing since the energy separation between the ground and excited state orbitals in bacteriochlorin systems has been found to be larger than in chlorin systems (see Chapter 3).[34]

The relative magnitudes of the spin densities determined for the pyrrole nitrogens in P_{700}^{+} can be used to explain the quadrupole parameters, and, in particular, the relative orientations of the hyperfine and quadrupole axis systems. Numerical simulations of ESEEM data have shown that the quadrupole axes of two of the nitrogens (N_I and N_{IV}) are collinear with the axis system of the hyperfine tensor. The principle axes of these two

Table 4-6: Experimental and calculated reduction factors for P_{700}^{+}

Atom	Ground state, D_0*	(0.75) D_0 x (0.25) D_1	$RF_{(calc)}$	$RF_{(expt)}$
C1	0.023	0.019	1.2	1.1**
C2	0.014	0.0100	1.4	
C3	0.037	0.0285	1.3	1.1**
C4	0.020	0.0142	1.4	1.5**
C5	0.006	0.0075	0.8	1.5**
C6	0.078	0.0600	1.3	
C9	-0.001	-0.0008	1.2	
C11	0.072	0.0485	1.5	
C12	0.090	0.0655	1.4	
C13	0.115	0.0830	1.4	
C14	0.147	0.1082	1.4	
C15	0.167	0.1235	1.3	
C16	0.105	0.0760	1.4	
C17	0.099	0.0734	1.3	1.3**
C18	0.73	0.0505	1.4	1.3**
Cα	-0.025	0.0275	0.9	1.1**
Cβ	-0.041	0.0060	6.8	
Cγ	-0.009	0.0322	0.3	
Cδ	-0.004	0.0455	0.1	
C2a	0.002	0.0017	1.2	1.1**
C2b	0.002	0.0016	2.0	
O1	0.030	0.0235	1.3	
O6	-	-	-	
N1	-0.005	0.0205	0.2	0.3
N2	-0.013	0.0107	1.2	1.3
N3	-0.008	0.0062	1.3	1.1
N4	-0.001	0.0317	0.03	0.07

*data from reference 34

**data from reference 11

tensors lie parallel to the p_z orbital, normal to the molecular plane. In nuclei carrying a large amount of unpaired spin density (e.g. N_I and N_{IV}), the electric field gradient in the p orbital, which contributes to the π molecular orbital, would be expected to be larger than in the s orbital participating in the σ bond to Mg. The principle axis of the field gradient therefore is expected to be along p_z; this is the case for N_I and N_{IV}.

Because the principle axis of the field gradient is sensitive to small changes in the orbital occupancy,[26] particularly in pyrrole systems where the field gradients are similar in the p orbital and the orbital containing the lone pair, small changes in the unpaired spin density can effect changes in the direction of the principle axis. This is most likely the case for N_{II} and N_{III}, the two pyrrole nitrogens carrying smaller amounts of unpaired spin density. The orientation of the quadrupole axis system for these two nuclei was found to be 90° shifted from that of the hyperfine tensor. For these nuclei, the s orbital participating in the coordinate covalent bond with the Mg^{2+} atom now carries the largest electric field gradient therefore, the principle axis of the quadrupole tensor lies along this orbital, in the molecular plane and perpendicular to A_{zz}, the principle axis of the hyperfine tensor.

The asymmetry parameter is also very sensitive to electric field gradients and has been found to shift dramatically as the result of hydrogen bonding and other electrostatic interactions. Interactions with charged amino acids or even with the carbonyl or ester functionalities of the other half of the chlorophyll dimer near N_I and N_{IV} may be responsible for the smaller η values determined for these nuclei. The distance between

the two chlorin planes has been determined by X-ray crystallographic studies to be about 4.5 Å, close enough to affect the electric field gradient near the nitrogens.[3]

Conclusions

Taken together, these data represent the first definitive assignments of hyperfine and quadrupole coupling constants to the nitrogen nuclei in P_{700}^{+}. The magnitude of the hyperfine couplings and their corresponding spin densities are indicative of a monomeric chlorophyll a cation radical interacting with its protein environment through axial ligation or hydrogen bonding. These effects cause an admixing of the ground and first excited state molecular orbitals to create a hybrid orbital with an altered spin density distribution when compared to chlorophyll cation radical species *in vitro*. Additionally, the methodology utilized to determine these parameters, a combination of isotope enrichment, electron magnetic resonance spectroscopy and numerical simulations, provides a means by which complicated couplings in biological systems can be consistently and systematically evaluated.

LIST OF REFERENCES

LIST OF REFERENCES

[1] For reviews see: a) Golbeck, J. (1992) *Annu. Rev. Plant Physiol. Plant Mol. Biol. 43*, 293 b) Malkin, R. (1996) in *Advances in Photosynthesis* (Ort, D. & Yocum, C.F., eds.) Kluwer, Dordrecht, in press.

[2] For reviews see: Diner, B.A. & Babcock, G.T. (1996) in *Advances in Photosynthesis* (Ort, D. & Yocum, C.F., eds.) Kluwer, Dordrecht, in press. b) Britt, R.D. (1996) in *Advances in Photosynthesis* (Ort, D. & Yocum, C.F., eds.) Kluwer, Dordrecht, in press.

[3] Fromme, P., Witt, H.T., Schubert, W.-D., Klukas, O., Saenger, W. & Krauss, N. (1996) *Biochim. Biophys. Acta 1275*, 76-83; Krauss, N., Hinrichs, W., Witt, I., Fromme, P., Pritzkow, W., Dauter, Z., Betzel, C., Wilson, K.S., Witt, H.T. & Saenger, W. (1993) *Nature 361*, 326-330.

[4] Moenne-Loccoz, P., Robert, B., Ikegami, I. & Lutz, M. (1990) *Biochemistry 29*, 4740.
Ratajczak, R. Mitchell, R. & Haehnel, W. (1988) *Biochim. Biophys. Acta 933*, 306.
[5] Norris, J.R., Uphaus, R.A., Crespi, H.L. & Katz, J.J. (1971) *Proc. Natl. Acad. Sci. USA 68*, 625.

[6] Wasielewski, M.R., Norris, J.R., Crespi, H.L. & Harper, J. (1981) *J. Am. Chem.Soc. 103*, 7664.

[7] Rutherford, A.W.& Mullet, J.E. (1981) *Biochim. Biophys. Acta 635*, 225.

[8] Davis, R.C. & Pearlstein, R.M. (1983) *Nature (London) 280*,413.

[9] Katz, J.J., Shipman, L.L. & Norris, J.R. (1981) in *Chlorophyll Organization & Energy Transfer in Photosynthesis*, Ciba Foundation Symposium 61, (Wolstenholme, G. & Fitzsimmons, D.W., eds.) pp 1-40, Excerpta Medica, Amsterdam.

[10] Eccles, J. & Honig, B. (1983) *Proc. Natl. Acad. Sci. USA 80*, 4959.

[11] O'Malley, P. J. & Babcock, G.T. (1984) *Proc. Natl. Acad. Sci. US, 81*,1098-1101.

[12] Deisenhofer, J., Epp, O., Miki, K., Huber, R. & Michel, H. (1985) *Nature 318*, 618.

[13] Allen, J.P., Feher, G., Yeates, T.O., Komiya, H. & Rees, D. (1987) *Proc. Natl. Acad. Sci. USA 84*, 5730.

[14] a) Lendzian, F., Lubitz, W., Scheer, H., Hoff, A.J., Plato, M., Trankle, E. & Mobius, K. (1988) *Chem. Phys. Lett. 148*, 377. b) Lendzian, F., Huber, M., Isaacson, R.A., Endeward, B., Plato, M., Bonigk, B., Mobius, K., Lubitz, W. & Feher, G. (1995) *Biochim. Biophys. Acta 1183*, 139.

[15] A) Käβ, H., Bittersmann-Weidlich, E., Andreasson, L.-E., Bonigk, B. & Lubitz, W. (1995) *Chem. Phys, 194*, 419-432. B) Käβ, H. & Lubitz, W. (1996) *Chem. Phys. Lett. 251*, 193-203.

[16] Noren, G.H., Boerner, R.J. & Barry, B.A. (1991) *Biochemistry 30*, 3943.

[17] Bender, C.J., Sahlin, M., Babcock, G.T., Barry, B.A., Chandrashekar, T.K., Salowe, S.P., Stubbe, J., Lindstrom, B., Petersson, L., Ehrenberg, A. & Sjoberg, B.-M. (1989) *J. Am. Chem. Soc. 111*, 8076-8083.

[18] McCracken, J., Shin, D.-H & Dye, J.L. (1992) *Appl. Magn. Reson 3*, 30.

[19] Lin, C.P., Bowman, M.K. & Norris, J.R. (1985) *J. Magn. Res. 65*, 369-374.

[20] Mehring, M. & Freysoldt, F. (1980) *J. Phys. E: Sci. Instrum.* 13, 894-895.

[21] Mims, W.B.(1984) *J. Magn. Reson. 59*, 291-306.

[22] Mims, W.B. (1972) *Phys. Rev. B 5*, 2409-2419.

[23] Kass, H., Rautter, J., Bonigk, B., Hofer, P. & Lubitz, W. (1995) *J. Phys. Chem. 99*, 436.

[24] Bowman, M.K., Norris, J.R., Thurnauer, M.C., Warden, J., Dikanov, S.A.& Tsvetkov, Yu. D. (1978) *Chem. Phys. Lett. 55*, 570. Dikanov, S.A., Astaskhin, A.V., Tsvetkov, Yu.D. & Goldfeld, M.G. (1983) *Chem. Phys. Lett. 101*, 206. Astashkin, A.V., Dikanov, S.A. & Tsvetkov, Yu.D. (1988) *Chem. Phys. Lett. 152*, 258.

[25] Barry, B.A., El-Deeb, M.K., Sandusky, P.O. & Babcock, G.T. (1990) *J. Biol. Chem. 265*, 20139.

[26] Ashby, C.I.H., Cheng, C.P. & Brown, T.L. (1978) *J. Am. Chem. Soc. 100*, 6057.

[27] Davis, I.H., Heathcote, P., MacLachlan, D.J. & Evans, M.C.W. (1993) *Biochim. Biophys. Acta 1143*, 183-189.

[28] Hoff, A.J., DeGroot, A., Dikanov, S.A., Astashkin, A.V.& Tsvetkov, Yu.D. (1985) *Chem. Phys. Lett. 118*, 40.

[29] Townes, C.H. & Dailey, B.P. (1949) *J. Chem. Phys. 17*, 782.

[30] Luckens, E.A.C. (1969) in *Nuclear Quadrupole Coupling Constants*, Chap. 11, pp 217-233, Academic Press, New York.

[31] Blackman, G.L., Brown, R.D., Burden, F.R. & Elsum, I.R. (1976) *J. Mol. Spectrosc. 60*, 63.

[32] Davis, I.H., Heathcote, P., MacLachlan, D.J. & Evans, M.C.W. (1993) *Biochim. Biophys. Acta 1143*, 183-189. Käβ, H., Bittersmann-Weidlich, E., Andreasson, L.-E., Bonigk, B. & Lubitz, W. (1995) *Chem. Phys, 194*, 419-432. Käβ, H. & Lubitz, W. (1996) *Chem. Phys. Lett, 251*, 193-203.

[33] Gordy, W. (1980) *Theory and Applications of Electron Spin Resonance in Techniques of Chemistry*, Vol. XV (West, W., ed.) John Wiley & Sons, New York

[34] Petke, J.D., Maggiora, G.M., Shipman, L.L. & Christoffersen, R.E. (1980) *Photochemistry and Photobiolog, 31*, 243-257.

[35] Hanson, L.K. (1990) in *Chlorophylls* (Scheer, H., ed) pp 1015-1042, CRC Press, Boca Raton

Chapter 5

The Effect of Sr^{2+} Substitution on the Oxygen Evolving Complex of Photosystem II

Introduction

Water oxidation in Photosystem II (PSII) occurs at an oxygen evolving complex (OEC) that consists, in part, of a cluster of four Mn atoms.[1,2] In addition to Mn, two Ca^{2+} ions per reaction center are required to activate oxygen evolution;[3] their location in PSII is uncertain (see Chapter 1 for a complete description of PSII). Successive light-induced charge separations cause the OEC to advance through five oxidation states, S_0-S_4.[4] A characteristic multiline EPR signal that arises from an S= ½ ground state of an exchange coupled Mn tetramer is associated with the S_2 oxidation state of the OEC.[5,6] Substitution of Sr^{2+} for Ca^{2+} maintains catalytic activity and gives rise to a modified multiline EPR spectrum.[7,8] These modifications are manifested as changes in both the number and average hyperfine splittings of the peaks (see Figure 5-1) and have been attributed to chagnes in either the structure or ligand environment of the Mn complex.[9] Electron spin echo envelope modulation (ESEEM) studies have identified a nitrogen-based ligand[10] to the OEC, which is assigned to the amino acid histidine.[11] This chapter describes studies in which the Mn-N_{his} ligation is utilized as a probe into the structural changes that may occur as a result of the Sr^{2+}. Well-resolved two and three pulse ESEEM data on the multiline EPR signal show that the electronic and geometric structure of at least one Mn is unaffected by Sr^{2+} substitution.

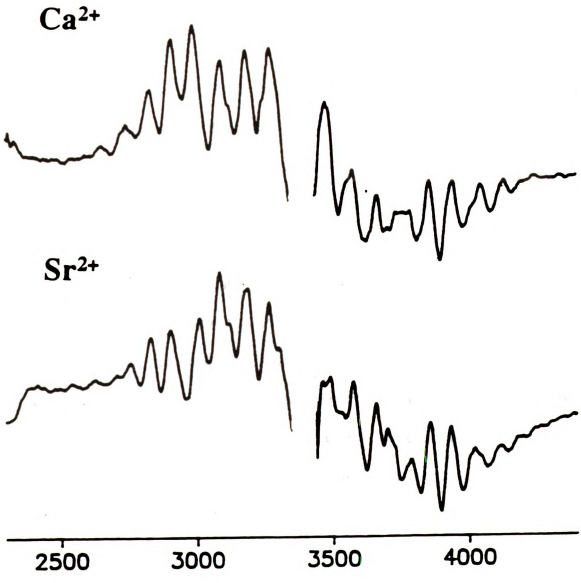

Figure 5-1: Light minus dark multiline EPR spectra from untreated (top) and Sr^{2+} substituted (bottom) RCCs. Spectrometer conditions: microwave power, 20 mW; modulation amplitude, 20 Gpp; modulation frequency, 100 kHz; sweep time, 100 s; time constant, 200 ms; sample temperature, 8 K.

Materials and Methods

The development in 1981 of a PSII enriched thylakoid membrane preparation, free from other electron transfer proteins, yet still functional in terms of oxygen evolution facilitated study of the PSII environment.[12] These particles, BBYs, allow direct spectroscopic studies of the OEC and serve as the starting point for the isolation of smaller membrane free complexes. This preparation relies on the fact that the thylakoid membranes, with their inherent negative charges, can be "stacked" by using divalent cations, such as Mg^{2+}. This increased lateral concentration can then be pelleted out by using selective solubilization techniques. This treatment removes approximately 95% of the PSI as well. Only the light harvesting complex proteins and the PSII/OEC remain after completion of this process. Moreover, the decreased number of chlorophyll molecules per PSII, 400 Chl/PSII in prior preparations to 250 Chl/PSII in BBYs, facilitates direct spectroscopic examination of the PSII electron transfer cofactors and, in particular, the Mn ensemble. The decreased chlorophyll concentration relative to PSII also results in increased O_2 evolution activity by allowing saturating light to reach the reaction centers.

Even with the increased concentration of active PSII centers and concomitant increase in O_2 activity, spectroscopic investigations of the EPR signal from the S_2 state of the OEC have been inhibited by the small number of spin present in the sample. Even with saturating light sources and a minimal number of inactive centers, extensive signal averaging was still necessary to obtain a resolved cwEPR spectrum. The subsequent development of a preparation lacking the light harvesting complex by Ghanotakis and

coworkers[13] produced a reaction center core preparation (RCC) that contained only the central PSII components. These preparations, again characterized by increased oxygen evolution activity, eliminated the necessity for extensive signal averaging and, moreover, allowed the application of advanced spectroscopic techniques that require larger sample concentrations.

Sample preparation: PSII membrane samples from market spinach, isolated by using the method of Berthold *et al.*[12] were diluted to a chlorophyll concentration of 1.0 mg/ml by using an appropriate volume of SMN buffer (0.4 M sucrose, 50 mM MES, 15 mM NaCl, pH 6.0) containing 0.8% of the detergent octyl-β-D-thioglucopyranoside (OTG). This non-ionic detergent was included with the high salt concentration to solubilize the PSII membranes and facilitate the removal of the light harvesting complex proteins as well as the 17 and 23 kDa polypeptides.[14] Following incubation, the solution was centrifuged to remove the remnants of these polypeptides. The supernatant, containing the reaction center cores, was incubated in SMN in a 1:0.8 ratio. $MgCl_2$ was added to a final concentration of 10 mM. Following centrifugation, the pellet, consisting of the light harvesting complex and solubilized membranes, was discarded and the reserved supernatant was incubated on ice with an equal volume of 30% w/v of polyethylene glycol (PEG). The PEG precipitation step acts to aggregate the water molecules by causing "clumping" of the PSII constituents, and represents a modification to the original published procedure. The PSII cores are easily pelleted out with centrifugation, resuspended in SMN and reserved for later use.

Substitution of Sr^{2+} for Ca^{2+} in these RCC samples is accomplished by using Ca^{2+} free buffers to wash the isolated reaction centers after incubation in a high (1 M NaCl) salt buffer. Substitution of Sr^{2+} is easily accomplished by resuspending the final pellet in a Sr^{2+} (10 mM) buffer. Samples were loaded into 4 mm O.D. quartz EPR tubes and frozen to 77 K until EPR experiments could be performed.

EPR Spectroscopy: Dark EPR spectra of the Sr^{2+} and Ca^{2+} samples at 8 K were recorded with a either a Bruker ER200D or ESP300e spectrometer fitted with an Oxford Instruments ESR-900 cryostat. Microwave frequency was determined by using an EIP Microwave Model 25B frequency counter and the static magnetic field strength was measured with a Bruker ER035M NMR gaussmeter. A rectangular TE102 cavity was used.

Dark adapted samples (5 minutes) were illuminated at 200 K in a liquid nitrogen/ethanol bath. Illumination time was 2 minutes. Following illumination, the samples were frozen in the dark and the light spectra were recorded at 8 K. The spectra from both the dark and the illuminated Ca^{2+} sample correspond to an addition of 30 accumulations. The spectra from the Sr^{2+} sample correspond to an addition of 60 accumulations. Signal averaging was accomplished (on the ER200D spectrometer) with an IBM clone fitted with a data analysis program written in house. The spectra presented represent a light minus dark difference. Subtraction was carried out with an IBM clone by using software written in house. The experimental conditions accompany each figure.

ESEEM Spectroscopy: ESEEM data were collected on a home built spectrometer[15] by using a reflection cavity where a folded stripline[16] served as the resonant element. Either

a two-pulse (90°-τ-180°) or a three pulse or stimulated echo (90°-τ-90°-T-90°) pulse sequence was used. Dead time reconstruction was performed prior to Fourier transformation as described.[17] Computer simulations of the ESEEM data were performed on a Sun Sparcstation 2 computer utilizing FORTRAN software based on the density matrix formalism of Mims.[18] The analysis software for the treatment of experimental and simulated ESEEM data was written with Matlab (Mathworks, Nantick, MA). The experimental dead time was included in the simulations. An isotropic g-tensor was assumed in all of the calculations.

Results

Difference ESEEM spectra obtained by Fourier transformation of two-pulse time domain data from untreated and Sr^{2+} substituted RCCs are shown in Figures 5-2 and 5-3, respectively. These data were collected at field values corresponding to g = 1.8 and g = 1.9 for the two sample to avoid interference from the intense tyrosine radical signal at g = 2.0. The two pulse ESEEM spectra are identical for the two samples; a feature near 4 MHz is present in both spectra. An additional feature arising from weakly coupled matrix protons is also present in both spectra. The broad, featureless peak at 4 MHz is similar in frequency and appearance to the peak assigned, based on specific isotopic substitution and subsequent ESEEM studies, to the nitrogen moiety of histidine.[11] Resolution of low frequency component in a two pulse ESEEM experiment can be poor due to the short phase memory time T_m. To resolve these components, stimulated echo

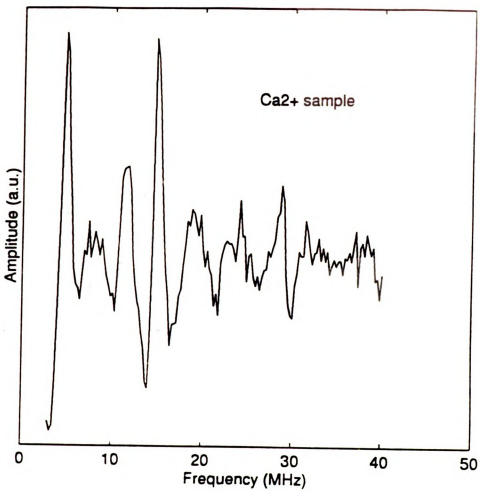

Figure 5-2: Fourier transformation of light minus dark two-pulse ESEEM data from untreated RCCs. Spectrometer conditions: magnetic field strength, 3440 G; microwave pulse power, 44 dBm; microwave pulse width, 22 ns; pulse repetition rate, 90 Hz; tau value, 200 ns; sample temperature, 4.2 K.

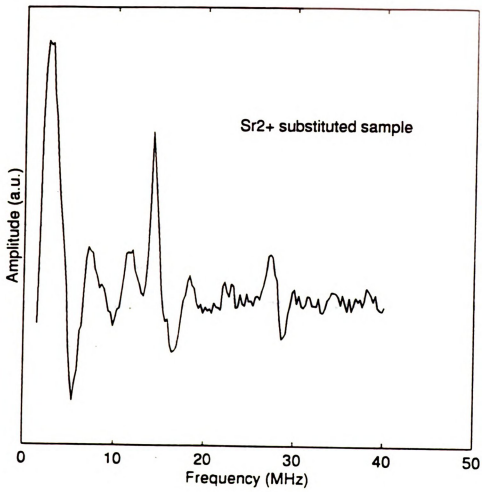

Figure 5-3: Fourier transformation of light minus dark two-pulse ESEEM data from Sr^{2+} substituted RCCs. Spectrometer conditions: magnetic field strength, 33250 G; all other conditions as in Figure 5-2.

experiments were performed. Since the decay of the modulations in these experiments is governed by the spin-lattice relaxation time, T_1,[19] improved resolution of the low frequency modulations is expected.

Stimulated echo difference ESEEM spectra from the untreated and Sr^{2+} substituted RCC samples are presented in Figures 5-4 and 5-5, respectively. These spectra were collected at field values identical to those in Figures 5-2 and 5-3. Unfortunately, no additional frequency components were resolved in these experiments. The spectra are similar; each exhibiting a single resonance in the 4 MHz region. Because the two spectra were collected at slightly different magnetic field values, these peaks are not observed at identical frequencies. However, by taking the difference in fields into account, these peaks represent identical couplings.

The magnetic field position at which the data are collected can have a profound effect on the appearance of the ESEEM spectrum. This is especially apparent in the case of the PSII samples where the overlap of multiple radical signals can make data analysis complicated and, although difference spectroscopy is employed to eliminate many of these contributions, care must be taken to avoid erroneous assignments.[20] The photoexcitation utilized to effect Mn oxidation to the S_2 state can produce radical species on the acceptor side of PSII that can not be completely eliminated by difference spectroscopy.

ESEEM spectra obtained by Fourier transformation[17] of three-pulse time domain data from untreated RCCs collected at 1.8 K are shown in Figure 5-6. All spectra were collected at g = 1.95 to avoid interference from the intense tyrosine radical signal at g =

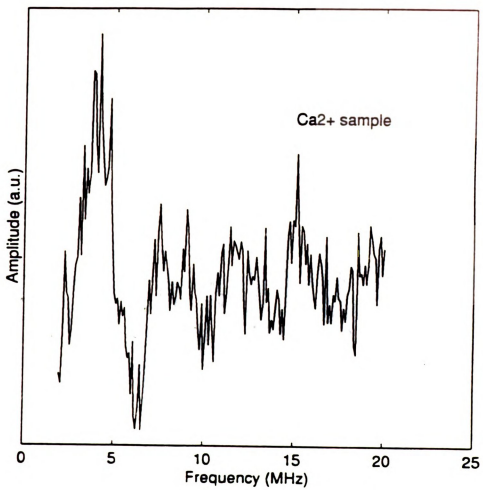

Figure 5-4: Fourier transformation of light minus dark three-pulse ESEEM data from untreated RCCs. Spectrometer conditions as in Figure 5-2.

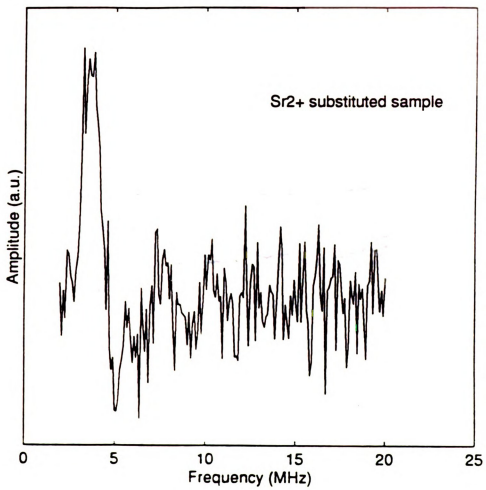

Figure 5-5: Fourier transformation of light minus dark three-pulse ESEEM data from Sr^{2+} substituted RCCs. Spectrometer conditions as in Figure 5-3.

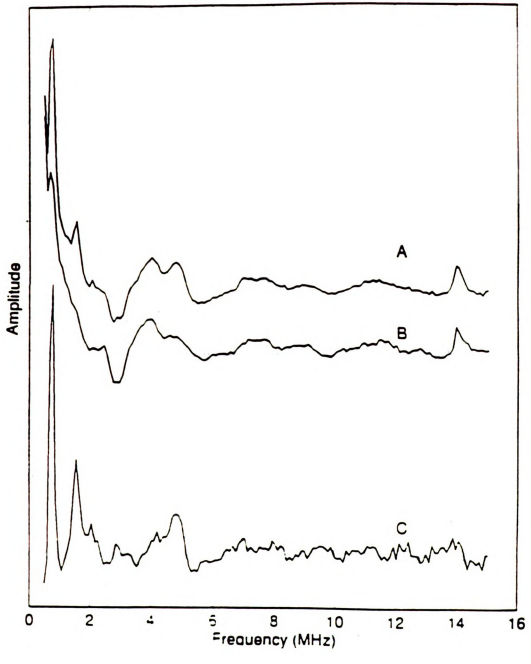

Figure 5-6: Three-pulse ESEEM spectra from untreated RCCs after illumination (top), prior to illumination (middle) and the light minus dark difference spectrum (bottom) collected at g=1.95. Spectrometer conditions: microwave frequency, 8.955 GHz; magnetic field strength, 3290 G; microwave pulse power, 20 W; tau value, 213 ns; pulse repetition rate, 90 Hz; sample temperature, 1.8 K.

2.0. The ESEEM spectrum from untreated RCCs in S_1 (Fig. 5-6. middle) shows peaks at 2.41, 3.85 and 14.10 MHz that arise from paramagnets present in this state. When advanced to S_2 by continuous illumination at 195 K for 10 minutes. the ESEEM spectrum (Fig. 5-6, top) shows peaks at 0.78, 1.55, 2.41. 3.85. 4.84 and 14.10 MHz. Following subtraction of the S_1 time domain data from that of S_2. and subsequent Fourier transformation of the difference (Fig. 5-6, bottom), peaks at 0.78. 1.55. 4.25 (shoulder) and 4.84 MHz are clearly evident. Because these spectra differ from those obtained at higher field values, the couplings observed must arise from a contaminating paramagnetic species that is not removed by using difference spectroscopy. The most likely candidate for this spurious radical is the quinone anion radical that acts as an electron acceptor in PSII.[21] Magnetic interactions between this quinone species and a non-heme iron produce an EPR signal centered at g = 1.9 and overlaps considerably at this g value with the multiline signal.[22] The peaks observed in the difference ESEEM spectrum most likely arise from a histidine residue interacting with this quinone-iron species.

The difference spectra in Figure 5-6 is indicative of ^{14}N-magnetic couplings close to the condition of exact cancellation.[23] In this condition, the positions of the two narrow, lower frequency peaks are dominated by ^{14}N nuclear quadrupole interactions. The frequency and lineshape of the 4.8 MHz feature is most sensitive to the superhyperfine coupling tensor and its orientation relative to the nuclear quadrupole tensor. Numerical simulations[18] of this ^{14}N-ESEEM spectrum yields an isotropic hyperfine coupling constant of 2.2 MHz, an effective dipole-dipole distance of 2.8 Å, an ^{14}N nuclear quadrupole coupling constant, e^2qQ, of 1.6 MHz and an asymmetry parameter, η, of 0.9.

An isotropic hyperfine coupling constant of 2.2 MHz is consistent with values obtained in a detailed ^{14}N ESEEM study of di-μ-oxo bridged Mn(III)Mn(IV) bipyridyl dimer compounds,[24] where scalar couplings of 2.8 MHz for the directly coordinated bipyridyl nitrogens were found. Therefore, the features of the ESEEM spectrum of Figure 5-6 are assigned to a histidyl nitrogen terminally coordinated to the non-heme iron and not to the histidine residue ligated to the Mn complex.

Discussion

EPR spectral shifts in a multinuclear metal cluster without corresponding changes in the ESEEM spectrum have precedence. For example, when the Rieske iron-sulfur center[25] of cytochrome b_6f is treated with 2,5-dibromo-3-methyl-5-isopropyl-benzoquinone, shifts in the g value occur without affecting the Fe-N interaction observed by ESEEM. Similarly, studies of copper (II) compounds ligated to substituted imidizoles show that changes in coordination geometry lead to changes in the Cu(II) hyperfine coupling without corresponding changes in ^{14}N-ESEEM.[26]

The ESEEM results presented here show that the bond length and bond covalency of the Mn-N_{his} bond, as well as the unpaired spin density on the Mn, do not change appreciably upon Sr^{2+} substitution.[9,27] The modifications in the EPR spectrum suggest, however, that structural or electronic changes do occur. Manganese hyperfine couplings in a cluster are a function of the spin projections of the individual ions onto the system spin as well as the hyperfine coupling values for the individual metals.[5] The spin

projections are related directly to the ground spin state of the cluster, whereas the hyperfine coupling constants of the individual metal ions are sensitive to changes in ligand environment. To affect the hyperfine coupling observed in the multiline EPR spectrum, one, or both, of these parameters must change. Because the S= ½ ground spin state of the Mn complex in S_2 is believed to be well separated from the first excited state,[28] it is unlikely that the Sr^{2+} induced modifications in the EPR spectrum arise from changes in the ground spin state.[29] However, changes in the ligand environment can cause the Mn hyperfine coupling to vary from 65 to 84 gauss.[30] The substitution of Sr^{2+} for Ca^{2+} may affect the hyperfine coupling of one, two or three of the Mn in the OEC without perturbing the Mn-N_{his} ligation observed with ESEEM.

Recent extended X-ray absorption fine structure (EXAFS) studies of PSII show that the Mn-Mn, Mn-O and Mn-terminal ligand distances are the same or only slightly different upon Sr^{2+} substitution.[31] The EXAFS data also suggest a close proximity of Ca^{2+} (Sr^{2+}) to the Mn cluster and a model based on the EXAFS data shows the Ca^{2+} bridged to one Mn by a carboxylate ligand.[31] The slightly larger ionic radius of Sr^{2+} over Ca^{2+} (1.13 Å versus 0.99 Å) appears to cause a modification of the structure of the Ca^{2+} binding site, which is transmitted to the Mn complex. Taken together, the ESEEM, EPR and EXAFS results indicate that a shift in hyperfine coupling that arises from terminal ligand effects remote from the Mn-N_{his} detected by ESEEM, rather than rearrangement of ground spin states, is the source of the EPR spectral modifications observed upon Sr^{2+} substitution.

LIST OF REFERENCES

LIST OF REFERENCES

[1] For reviews see: Diner, B.A. & Babcock, G.T. (1996) in *Advances in Photosynthesis* (Ort, D. & Yocum, C.F., eds.) Kluwer, Dordrecht, in press. b) Britt, R.D. (1996) in *Advances in Photosynthesis* (Ort, D. & Yocum, C.F., eds.) Kluwer, Dordrecht, in press. C) Debus, R.J. (1992) Biochim. Biophys. Acta 1102, 269.

[2] Yocum, C.F., Yerkes, C.T., Blankenship, R.E., Sharp, R.R. & Babcock, G.T. (1981) Proc. Natl. Acad. Sci. USA 78,7507.

[3] Yocum, C.F. (1991) Biochim. Biophys. Acta 1059,1.

[4] Kok, B., Forbush, B. & McGloin, M.P. (1970) Photochem. Photobiol. 11, 457.

[5] A) Dismukes, G.C. & Siderer, Y. (1981) Proc. Natl. Acad. Sci. USA 78, 274. B) Hansson, O. & Andreasson, L.-E. (1982) Biochim. Biophys. Acta 679,261.

[6] A) Britt, R.D., Lorigan, G.A., Sauer, K., Klein, M.P. & Zimmerman, J.-L. (1992) Biochim. Biophys. Acta 1140,95. B) Koulougliotis, D., Hirsh, D. & Brudvig, G.W. (1992) J. Am. Chem. Soc. 114, 8322.

[7] Boussac, A. & Rutherford, A.W. (1988) Biochemistry 27, 3476.

[8] Ghanotakis, D.F., Babcock, G.T. & Yocum, C.F. (1984) FEBS Lett. 167, 127.

[9] Sauer, K., Yachandra, V.K., Britt, R.D. & Klein, M.P. (1992) in Manganese Redox Enzymes, pp. 141-175, VCH Publishers, New York.

[10] DeRose, V.J., Yachandra, V.K., McDermott, A.E., Britt, R.D., Sauer, K. & Klein, M.P. (1991) Biochemistry 30, 1335.

[11] Tang, X.-S., Diner, B.A., Larsen, B.S., Gilchrist, M.L., Lorigan, G.A. & Britt, R.D. (1994) Proc. Natl. Acad. Sci. USA 91, 704.

[12] Berthold, D., Babcock, G.T. & Yocum, C.F. (1981) FEBS Lett. 34, 231.

[13] Ghanotakis, D.F., Babcock, G.T. & Yocum, C.F. (1984) FEBS Lett. 143, 175.

[14] OTG ref.

[15] McCracken, J., Shin, D.-H. & Dye, J.L. (1992) Appl. Magn. Reson. 3, 30.

[16] Lin, C.P., Bowman, M. K. & Norris, J.R. (1985) J. Magn. Reson. 65, 369.

[17] Mims, W.B. (1984) J. Magn. Reson. 59, 291.

[18] Mims, W.B. (1972) Phys. Rev. B 5, 2409.

[19] Schweiger, A. (1991) Angew. Chem. Int. Ed. Engl. 30, 265.

[20] Miller, A.-F. & Brudvig, G.W. (1991) Biochim. Biophys. Acta 1056, 1.

[21] Nugent, J.H.A., Diner, B.A. & Evans, M.C.W (1981) FEBS Lett. 124, 241.

[22] Rutherford, A.W. & Zimmerman, J.-L. (1984) Biochim. Biophys. Acta 767, 168.

[23] A) Flanagan, H.L. & Singel, D.J. (1987) J. Chem. Phys. 87, 5606. B) Mims, W.B. & Peisach, J. (1978) J. Chem. Phys. 69, 4921.

[24] A) Britt, R.D. (1988) Ph.D. Thesis, Department of Physics, University of California-Berkeley, Lawrence-Berkeley Laboratory, Laboratory Report LBL-25042. B) Britt, R.D. & Klein, M.P. (1992) in Pulsed Magnetic Resonance: NMR, ESR and Optics, pp. 390-410, Clarendon Press, Oxford.

[25] A) Britt, R.D., Sauer, K., Klein, M.P., Knaff, D.B., Kriauciunas, A., Yu, C.-A., Yu, L. & Malkin, R. (1991) Biochemistry 30, 1892. B) Malkin, R. (1982) Biochemistry 21, 2945.

[26] Jiang, F., Karlin, K.D. & Peisach, J. (1993) Inorg. Chem. 32, 2576.

[27] Tsao, J., Sivaraja, M.& Dismukes, G.C. (1991) Biochemistry 30, 4734.

[28] Hansson, O., Aasa, R. & Vanngard, T. (1987) Biophys. J. 51, 825.

[29] A) Chan, M.K.& Armstrong, W.H. (1992) J. Am. Chem. Soc. 113, 5055. B) Kirk, M.L., Chan, M.K., Armstrong, W.H. & Solomon, E.I. (1992) J. Am. Chem. Soc. 114, 10432. C) Pal, S., Chan, M.K. & Armstrong, W.H. (1992) J. Am. Chem. Soc. 114, 6398.

[30] A) Diril, H., Chang, H.-R., Niges, M.J., Zhang, X., Potenza, J.A., Schugar, H.J., Isied, S.S. & Hendrickson, D.N. (1989) J. Am. Chem. Soc. 111, 5102. B) Bonvoison, J., Blondin, G., Girere, J.-J. & Zimmerman, J.-L. (1992) Biophys. J. 61, 1076.

[31] Yachandra, V.K., DeRose, V.J., Latimer, M.J., Mukerji, I., Sauer, K. & Klein, M.P. 91993) Science 260, 675.